**POLITECNICO DI MILANO**

School of Industrial and Information Engineering
Master of Science in Engineering Physics

POLITECNICO
MILANO 1863

# Nanoscale spin-waves based platforms for magnon computing

**Supervisor:**
Dr. Daniela PETTI

**Candidate:**
Giuseppe SCARAMUZZI
**ID Number:**
882952

**Academic Year 2017-2018**

*Alla mia famiglia.*

# Abstract

In recent years, one of the major technological challenges consists in finding alternative routes to the well-established computational paradigm based on silicon and electrons transport. Indeed, the corresponding CMOS (Complementary Metal-Oxide-Semiconductor) technology is close to its fundamental limits, inherently related to the scaling of the devices in modern architectures, and to power dissipation issues and leakage currents. A big deal of interest inspires the scientific community in uncovering beyond-CMOS technologies able to overcome the current constraints. Among the emerging proposals, spin waves, namely the collective excitations of spin systems, offer several advantages, such as the absence of parasitic ohmic losses, frequencies up to the THz regime, and the possibility of designing analog-based platforms. Broadly speaking, the idea of optically-inspired devices, wherein the information is processed via the controlled interference of wavefronts, promises significant improvements for data encoding and their manipulation in several digital tasks. Although different fields of physics are already pursuing this scope, nowadays photonics represents the state-of-the-art. However, the main criticality related to the use of light resides in the centimetre-long wavelength of the electromagnetic radiation in the GHz and THz range, which forbids the miniaturization of photonic components. On the contrary, within the same frequencies, the sub-micrometre spin waves wavelength effectively paves the way towards analog computing.

To this purpose, in the first part of the present work, resulting from an international collaboration among United States (CUNY-Advanced Science Research Center), Italy (Politecnico di Milano and Dipartimento di Fisica e Geologia dell'Università di Perugia), and Switzerland (Paul Sherrer Institut), an optically-inspired platform has been realized, where magnetic domain walls are exploited as spin waves emitters (magnonic nanoantennas). The versatility of thermally assisted magnetic - Scanning Probe Lithography (tam-SPL), employed for magnetic patterning of arbitrarily shaped spin configurations, together with the distinctive magnetic properties of Synthetic Antiferromagnets (SAF), for the first time allowed the excitation and control

of spin waves with nanometre wavelengths and *ad hoc* engineered wavefronts. Especially, the combined action of tam-SPL and the non-reciprocal nature of propagating modes in SAF, has made possible both to achieve robust interference patterns and to generate linear, radial, convex and concave wavefronts. The latter experimental evidence is an indicative example of how the hosts of spin waves can influence their behaviour. In this regard, the second part of the thesis, which has arisen as a collaboration between Chile and Italy, has concerned the designing of an unconventional one-dimensional magnonic crystal, wherein a periodic spatial variation of the Dzyaloshinsky-Moriya interaction (DMI) defines the magnetic landscape. Though the aforementioned antisymmetric coupling is widely studied in literature, magnonic devices which take advantage of the DMI have not been realized yet. In virtue of the restrictive geometrical constraints, each fabrication stage has been singularly addressed and optimized, leading to magnonic crystals with a DMI modulation characterized by a period of 200 nm. The subsequent Brillouin Light Scattering (BLS) measurements have proved the theoretical predictions. A peculiar trend of the magnonic band structure has been ascertained, with a 1 GHz gap opening up between the lowest-lying frequency bands, and a localized mode related to a flat-band condition has been observed.

# Sommario

Una delle principali sfide tecnologiche dell'era moderna consiste nel trovare alternative valide al paradigma computazionale vigente incentrato sul silicio e sul trasporto di elettroni. La relativa tecnologia CMOS (Complementary Metal-Oxide-Semiconductor) è infatti sempre più prossima al raggiungimento dei sui limiti fondamentali, intrinsecamente legati alla miniaturizzazione dei componenti nelle attuali architetture elettroniche, e a problemi di dissipazione di potenza e di correnti di perdita. Un grande interesse alimenta perciò la comunità scientifica nel ricercare soluzioni post-CMOS in grado di superarne i vincoli attuali. Tra le proposte emergenti, l'uso di onde di spin, ossia eccitazioni collettive di sistemi che presentano un ordinamento magnetico, come vettori di informazione offre significativi vantaggi, quali l'assenza di dissipazione di energia per effetto Joule, la fattibilità di lavorare a frequenze fino ai THz, e, soprattutto, la possibilità di progettare piattaforme basate su computazione analogica. L'idea di dispositivi integrati inspirati all'ottica classica, dove l'informazione viene processata mediante l'interferenza controllata di fronti d'onda, promette infatti grandi miglioramenti nella codifica e nell'elaborazione di dati in molte applicazioni digitali. Sebbene diversi campi della fisica siano già indirizzati verso il suddetto obiettivo, la fotonica ad oggi rappresenta lo stato dell'arte da un punto di vista applicativo. Tuttavia, la principale difficoltà relativa all'impiego concreto della luce risiede nella lunghezza d'onda della radiazione elettromagnetica nei GHz e THz (dell'ordine del centimetro), che impedisce la miniaturizzazione dei componenti necessari per manipolare l'informazione. Di contro, nello stesso range di frequenze, la lunghezza d'onda (sub-micrometrica) delle onde di spin apre effettivamente la strada verso concreti sviluppi nel settore del calcolo analogico.

A tale proposito, nella prima parte di questo lavoro di tesi, frutto di una collaborazione internazionale tra Stati Uniti (CUNY- Advanced Science Research Center), Italia (Politecnico di Milano e Dipartimento di Fisica e Geologia dell'Università di Perugia), e Svizzera (Paul Sherrer Institut), è stata realizzata sperimentalmente una piattaforma che implementa approcci simili all'ottica, e che sfrutta pareti di dominio magnetiche come emettitori

di onde di spin (nanoantenne magnoniche). La versatilità della tecnica thermally assisted magnetic - Scanning Probe Lithography (tam-SPL), impiegata per il patterning magnetico di configurazioni di spin arbitrarie, unitamente alle caratteristiche magnetiche distintive di eterostrutture basate su Antiferromagneti Sintetici (SAF), ha permesso per la prima volta di eccitare onde di spin con lunghezze d'onda nanometriche, e di ingegnerizzarne *ad hoc* i fronti d'onda. In particolare, la flessibilità e la stabilità del sistema investigato, hanno consentito di ottenere figure di interferenza robuste, e di generare fronti d'onda lineari, radiali, convessi e concavi, sfruttando la combinazione della tecnica tam-SPL e la natura non-reciproca dei modi viaggianti nei SAF. Quest'ultima evidenza rappresenta un esempio significativo di come la scelta del supporto determini sostanzialmente il comportamento delle onde di spin che vi si propagano internamente. A questo riguardo, la seconda parte del presente lavoro, anch'essa risultato di una collaborazione tra Cile e Italia, concerne la progettazione di un cristallo magnonico monodimensionale basato su un concetto innovativo, ovvero contraddistinto da una modulazione spaziale periodica dell'interazione Dzyaloshinsky-Moriya (DMI). Sebbene il suddetto accoppiamento antisimmetrico sia largamente studiato in letteratura, dispositivi magnonici che sfruttano DMI non sono ancora mai stati realizzati. In virtù degli stringenti requisiti geometrici, ogni fase della fabbricazione è stata singolarmente pianificata, ed il processo ottimizzato ha condotto a cristalli dove la DMI viene modulata con un periodo di 200 nm. Le successive misure di Brillouin Light Scattering (BLS) hanno confermato le previsioni teoriche, cioè un andamento peculiare della struttura a bande del sistema, che presenta una gap di circa 1 GHz tra le due bande a frequenze minori, e un modo localizzato che non disperde (condizione di banda piatta).

# Contents

# List of Figures

# List of Tables

# Chapter 1

# Introduction

## 1.1 Magnonics: state-of-the-art

Nowadays, the incessant growth in the volume of information to handle requires to find new paradigms for fast and efficient computing and transfer of data. Promising candidates to flank and overstep the existing technology are spin waves, which open up very intriguing perspectives for high-speed and low-power information processing.

The notion of spin waves as collective excitations in magnetically ordered substances was first introduced by Bloch nearly one century ago [1]. From a classical *naïf* point of view, a spin wave depicts an ordered precession of microscopic magnetic dipoles inside a magnetic medium, whose energy quanta are called *magnons*. Magnonics is the related scientific field of magnetics, oriented towards both fundamental studies and practical applications of these quasi-particles. Nevertheless, in a similar fashion as electronics gathers a wide variety of effects that are not limited by the quantum nature of electrons, magnonics embraces a broad collection of phenomena connected with spin waves in general. Especially, it mainly deals with the control and manipulation of spin waves, with the ultimate scope of using them as information carriers at the nanoscale [2]. To this aim, the peculiar traits of spin waves substantially differentiate magnons from other quasi-particles, as photons and phonons. For instance, exchange-dominated spin waves can achieve sub-

nanometre wavelengths $\lambda$. Indeed, spin waves spectra comprises two main regimes according to the leading contributor to the magnons energy, namely the quantum exchange coupling on nanoscopic length scales, and the classical dipolar interactions for higher $\lambda$. Moreover, the spin waves dispersion relation $\omega(k)$ is anisotropic even for isotropic media, and usually contains a gap $\omega(k = 0) \neq 0$ that depends on both the applied field and the geometry of the ferromagnetic sample.

In contrast with conventional electronics, which relies on the transport of electron currents, magnon currents are spin fluxes, which propagate without charge transfer. Therefore, by avoiding the associated ohmic losses, the use of spin waves can dramatically reduce the power consumption for data handling. Besides, spin waves promise other gains [3], such as: the availability of magnetically ordered conductors and insulators as spin waves hosts; the wide range of frequencies encompassed in spin waves spectra, which may boost the clock frequencies of future calculators; the possibility of exploiting spin waves even at room temperature; the existence of strong spin waves non-linear effects, allowing for the realization of magnon-magnon interaction-based functionalities; the capability of encoding information in both the amplitude and the *phase* of travelling spin waves. Noteworthy, besides digital processing, the latter paves the route also towards analog-based architectures. In this regard, albeit the idea of using waves for signal conditioning has already been conceived and tested in photonics over the past years, spin waves offer relevant benefits.

The first advantage of spin waves compared to light resides in their available wavelengths $\lambda$. As a matter of fact, for all practical situations (i.e. in the GHz to THz frequency regime), $\lambda$ is several orders of magnitude smaller than that of electromagnetic radiation (it can be as short as 10 nm), thus opening encouraging miniaturization prospects for magnonic devices at these frequencies. Furthermore, in the GHz–THz range, spin waves propagation distances span several times their wavelength, letting them be concretely feasible means to carry information. In addition, compared to light, the corresponding spin waves 'refraction index' is easier to manipulate [4], making magnons more favourable than photons for technological applications. For in-

stance, spin waves characteristics can be engineered by properly modulating macroscopic parameters, such as the exchange constant and the saturation magnetization. Broadly speaking, the spin waves dispersion relation inside a ferromagnet noticeably changes already by simply modifying the magnetization direction. This enormous flexibility, together with the continuous improvement of nanofabrication lithographic techniques, let novel artificial magnetic media develop, whose properties can be tailored by designing *ad hoc* the spectra of the supported spin waves excitations.

In order to represent an actual alternative among beyond-silicon-based technologies, magnonics needs to fulfil some fundamental prerequisites. Especially, for realizing efficient magnonic devices, the capability of controlling the propagation of spin waves down to the nanoscale, the ability of exciting such perturbations at specific frequencies and with nanometre wavelengths, and the deterministic manipulation of their properties (phase, interference etc.), are all necessary conditions. For this reason, new fabrication methods and novel device concepts should be implemented to overstep conventional approaches, which rely on 'shaping' materials for using the related shape anisotropy to control spin waves. One example, of particular interest for the present work is represented by the so-called magnonic crystals, which are periodically structured systems playing the same role as photonic crystals for light. Such metamaterials open a plethora of possibilities for spin-wave-based devices, including both passive and active elements. A non-exhaustive list comprehends filters, spin waves conduits, sensors [5], delay lines and phase shifter for microwave generation [6], and component of logic gates [7].

To date, both one-dimensional and two-dimensional magnonic crystals have been deeply investigated. As for the former, they usually are constituted by arrays of alternate stripes of ferromagnetic/nonmagnetic materials or by arranging side-by-side different ferromagnetic slabs [3]. On the other hand, two-dimensional magnonic crystals are split into three major groups [8], namely interacting arrays of ferromagnetic discs, anti-dot lattices, and bi-component heterostructures. Nevertheless, it is worth to note that the fabrication of this type of devices provides challenges due to the interplay between their magnetic properties, their shape, and local and non-local in-

teractions. In addition, using conventional approaches to magnonic crystals fabrication requires to physically carve the magnetic active layer, resulting in a possible deterioration of its magnetic properties and in an increase of the spin waves damping and scattering.

Instead of suitably tailoring the geometry of the samples, other ways can be thought to control spin waves inside specific hosts. Indeed, a novel device concept, which has been theoretically proposed in [9], aims to manipulate the spin waves behaviour by means of Dzyaloshinsky-Moriya-like interactions (DMI) at the interfaces between a ferromagnet and a heavy metal. In this regard, chiral spin textures of a ferromagnetic layer in contact to a heavy metal, as Skyrmions, have been examined intensively because of their potential for future nanomagnetic devices, and DMI is an essential ingredient for the formation of such spin configurations. Besides, several studies have established that magnons are non-reciprocal in this kind of systems [10, 11], and a rich variety of physical phenomena is largely anticipated from the combination of magnonics and interfacial DMI. Yet, a concrete implementation of an artificial metamaterial exploiting a periodic modulation of DMI lacks in literature, and it is exactly one of the goals of the present research.

Though the designing of spin waves properties via magnonic crystals is a well consolidated experimental evidence, the practical nanoscale control of spin waves propagation possibly remains an issue, and several attempts were carried out in the past in developing appropriate conduits. Customarily, lithographed ferromagnetic waveguides in the form of stripes are used to transmit spin waves in proof-of-principle prototypes, where the travelled distances are mainly limited by the material-specific Gilbert damping parameter $\alpha$. The latter is significantly lowered for a particular type of modes, namely the one related to Magnetostatic Surface Spin Waves (MSSW). In fact, MSSW are the most suitable for experimental implementations either due to the low value of $\alpha$, and their high group velocities [12]. However, within these schemes, a large external magnetic field is always necessary to promote MSSW, which move perpendicularly to the in-plane magnetization direction. Indeed, in a ferromagnetic stripe, the shape anisotropy tends to orient the magnetization parallel to its principal axis, and external fields are

required to rotate it along the short direction of the waveguide, i.e. perpendicularly to the MSSW wavevectors. Moreover, the employed global magnetic field does not permit the channeling of MSSW along curved paths, since it cannot locally cant the magnetization to make it perpendicular to the waveguide everywhere. Therefore, other methods than the lithographic patterning of the samples have to be addressed to the purpose.

Recently, steering of spin waves has been proved in arrays of nanomagnets [12] and inside domain walls (DWs) of thin ferromagnets [13]. Especially, a magnetic domain wall is an interface separating regions with different magnetization direction (magnetic domains), wherein the latter is naturally oriented perpendicular to the wall, and no fields are demanded to let MSSW propagate confined to it. In this kind of experiments, thermally assisted magnetic - Scanning Probe Lithography, have successfully been used for arbitrarily (and reversibly) tailoring the spin configuration of ferromagnetic media. As a matter of fact, in [14] for the first time spin waves propagation inside DWs was directly observed, and a prototypic spin wave circuit to superimpose two distinct signals was demonstrated. Nevertheless, in such an approach, the allowed wavelengths range in the micrometre length scale, thus partially inhibiting the benefit of magnonic devices, which promise miniaturization of the building blocks down to the nm. To overcome this limitation, other strategies have been developed using stripes of Co atop of YIG [15], which yet suffer from the deficit of CMOS compatibility due to the substrate (Gadolinium Gallium Garnet) exploited for the growth of YIG. Only lately, an encouraging proposal have arisen by considering a peculiar magnetic heterostructure, namely a Synthetic Antiferromagnet (SAF) [16].

Yet, the effective generation of short-wavelength spin waves, and the manipulation of the corresponding wavefronts remain a significant challenge. Indeed, the widely-adopted mechanism for spin waves excitation consists in the use of lithographed antennas, which give rise to a Oersted field that couples to the magnetization nearby, thus triggering the emission of spin waves. However, the lowest achievable $\lambda$ is intimately related with the width of the antennas [17], which in turn is limited by impedance mismatching. Besides, this scheme lacks of the versatility required by reprogrammable devices, since

once the antennas are physically patterned, their shape, and thus the spin waves wavefront, cannot be further modified. As a matter of fact, the other fundamental goal of the present research thesis is to show an alternative feasible method to face the problem, which, at the same time, has allowed for the generation of spin waves with nanometre wavelengths and reconfigurable engineered waveforms.

## 1.2 Thesis outline

The current work has been carried out under the supervision of Dr. Daniela Petti, within the NanoBiotechnology and Spintronics (NaBiS) group, coordinated by Prof. Riccardo Bertacco. Though the research activity has been primarily conducted at PoliFAB, the micro and nano technology centre of Politecnico di Milano, I also partook in the measures, within the SWING project, performed at the Swiss Light Source (SLS) synchrotron facility, hosted at the Paul Scherrer Institut (PSI) in Villigen, Switzerland.

Two are the major topics covered in the present thesis. In the first part, it has been investigated the possibility of launching and controlling spin waves by exciting patterned spin textures in peculiar magnetic systems, namely Synthetic Antiferromagnets (SAFs). Combining the unique features of SAFs together with the inherent flexibility offered by thermally assisted magnetic - Scanning Probe Lithography (tam-SPL), a nanoscale optically-inspired spin-wave-based platform has been developed for the first time.

The second part of the work results from a collaboration with a theorists group, and it has aimed to realize an unconventional magnonic crystal whose magnetic landscape is affected by a periodic Dzyaloshinsky-Moriya interaction (DMI). Due to restrictive geometrical constraints, a precise optimization of each nanofabrication stage has been required, which ultimately led to a good agreement between envisioned predictions and experimental outcomes.

The subsequent sections are organised as follows:

- **Chapter 2** provides the fundamental background necessary to understand the physics underlying the discussed phenomena.

- **Chapter 3** reviews the working principles of the experimental techniques employed in this work to fabricate and characterize the devices and the heterostructures of interest.
- **Chapter 4** reports on the samples preparation, their successive magnetic patterning, and the final experimental investigation of exploiting arbitrarily shaped spin textures as emitters for spin waves with nanometre wavelengths and customized wavefronts.
- **Chapter 5** is devoted to frame the main fabrication steps which brought to the ended one-dimensional magnonic crystals, and to highlight a comparison with the theoretical expectations.
- **Chapter 6** summarizes the results achieved insofar and outlines the future perspectives.

# Chapter 2

# Theoretical framework

## Overview

Aim of the present chapter is to briefly review the theoretical background necessary to figure out the work that has been done. Especially, within the micromagnetics framework, the expression for the total energy of a magnetic body is built piece by piece and the physical meaning of each term is explained. Then, Brown equations are reported and the relevant aspects of static equilibria are discussed. Subsequently, both interfacial effects and higher order energy terms are shortly investigated; indeed, all of these contributions have been exploited and tailored in the current research thesis (see Chapter 4 and Chapter 5). Finally, the last part of the chapter deals with the collective excitations of the electrons spin inside solids and their quantized version, namely spin waves and magnons respectively. In particular, an elementary derivation of the magnon dispersion relation for an isotropic one-dimensional ferromagnet is given (through the *spin exchange operator method*) and the distinctive features of the existing modes within a thin ferromagnetic film are examined.

## 2.1 Micromagnetism

Broadly speaking, the magnetic properties of all materials are assessed according to the atoms or ions they contain, which can either possess permanent magnetic moments or not. Within the first group, it is possible to further distinguish materials manifesting a long-range order among the magnetic moments (below a critical temperature) and those that do not, namely *paramagnets*. Lastly, different magnetic orders can be found.

*Ferromagnets* (FMs) are media in which the elementary permanent moments, due to a phase transition, partially align below a specific temperature, known as Curie Temperature $T_C$. Their most peculiar feature is the existence of a macroscopic non-zero magnetization $\mathbf{M}$, defined as the average dipole moment per unit volume, in the absence of an external magnetic field. Indeed, while in paramagnetic materials $\mathbf{M}$ is proportional to the applied field $\mathbf{H}$ through the so-called magnetic susceptibility $\chi$, for ferromagnets $\mathbf{M}$ is not even a one-valued function of $\mathbf{H}$; its response to an imposed magnetic field, epitomized by a hysteresis loop, depends on the 'history' of the sample and it is highly irreversible and non-linear.

The broad family of magnetic substances does not consist only of FMs. As a matter of fact it may happen that the coupling between adjacent moments is such that they tend to line up along opposite directions. In these circumstances, the long-range order can be viewed in terms of two opposite ferromagnetic sublattices; if the overall net magnetization is zero the material is called *antiferromagnet* (AF), otherwise it is recognized as *ferrimagnet*. A common thread joining these compounds to the previous one is the 'randomizing' role of thermal fluctuations, and the temperature above which the magnetic arrangement is now completely lost is called Néel temperature $T_N$.

Ferromagnets, antiferromagnets and ferrimagnets are just non-exhaustive examples of the richness encompassed by magnetic phenomena, which goes far beyond the aforementioned scheme. In real-cases study, the complexity of determining the properties of magnetic substances is strictly linked to the capability of foreseeing their behaviour when subjected to an external field, i.e. $\mathbf{M}(\mathbf{H})$. Due to the subtle interplay between the several competing con-

tributions involved, this task is extremely hard to face. Goal of the next few paragraphs is to explain the underlying physics governing the configuration of a magnetic material under equilibrium conditions. Especially, the case of a sub-micrometer ferromagnet is considered. The main mechanisms leading the expression for the total energy of such a system are exchange interaction, dipolar energy, Zeeman coupling to an external field and magnetic anisotropies; interfacial and higher order energy effects are later examined.

In what follows the theoretical framework of *micromagnetism* is employed. Within this approach, which is a thermodynamic one, the most energetically favourable state results from the minimization of a free energy functional including all the terms listed before. The basic idea is to divide the investigated body into tiny volume elements $\Delta V$, where the magnetization $\mathbf{M}$ can be assumed uniform and such that $\mid \mathbf{M} \mid \equiv M_S$, being $M_S$ its value attained at saturation (*macrospin model*). On one hand, these volume partitions must be small enough compared to the length over which the direction of $\mathbf{M}$ changes, on the other hand, they need to be sufficiently big so that statistics can be applied. Moreover, the *continuum approximation* is adopted, thus neglecting the granular structure of matter and supposing $\mathbf{M}(\mathbf{r})$ as a 'smooth' function.

### 2.1.1 Exchange interaction

Exchange interaction lies at the very root of the phenomenon of long-range magnetic order; it has no classical analogue, and is caused by electronic wave functions overlap in quantum mechanics. Indeed, it reflects the electrostatic Coulomb repulsion of nearby charges together with the Pauli exclusion principle [18], which forbids them to access the same quantum state.

To get some insight, consider a simple model involving just two electrons, $a$ and $b$, whose coordinates are labelled with $\mathbf{r}_1$ and $\mathbf{r}_2$ respectively. Since they are indistinguishable, the wave function for the joint state must obey exchange symmetry, as the same electron density is given upon exchanging the two. Therefore, the only states allowed are symmetrized or antisymmetrized product states, which properly behave under the action of the exchange operator $\hat{P}$. Besides, due to the electrons fermionic nature, the overall solution

$\Psi$, comprehending both the spatial and spin parts, needs to be antisymmetric on the whole. Hence, the symmetric spatial state couples with the antisymmetric spin singlet state $\chi_S$ ($|\uparrow\downarrow\rangle$), whereas the antisymmetric spatial state with the symmetric spin triplet state $\chi_T$ ($|\uparrow\uparrow\rangle$). The options for $\Psi$ are then:

$$\Psi_S = \underbrace{\frac{1}{\sqrt{2}}[\psi_a(\mathbf{r}_1)\psi_b(\mathbf{r}_2) + \psi_a(\mathbf{r}_2)\psi_b(\mathbf{r}_1)]}_{\text{Symmetric Spatial Combination}} \chi_S$$

$$\Psi_T = \underbrace{\frac{1}{\sqrt{2}}[\psi_a(\mathbf{r}_1)\psi_b(\mathbf{r}_2) - \psi_a(\mathbf{r}_2)\psi_b(\mathbf{r}_1)]}_{\text{Antisymmetric Spatial Combination}} \chi_T$$

The energies associated to these wave functions can be simply evaluated as:

$$E_S = \int \Psi_S^* H \Psi_S d\mathbf{r}_1 d\mathbf{r}_2$$

$$E_T = \int \Psi_T^* H \Psi_T d\mathbf{r}_1 d\mathbf{r}_2$$

with the extra assumption that also the spin parts $\chi_S$ and $\chi_T$ are normalized. The energy difference is thus:

$$\Delta E \equiv E_S - E_T = 2 \int \psi_a^*(\mathbf{r}_1)\psi_b^*(\mathbf{r}_2) H \psi_a(\mathbf{r}_2)\psi_b(\mathbf{r}_1) d\mathbf{r}_1 d\mathbf{r}_2 \tag{2.1}$$

Defining the *exchange integral* $J$ as $J \doteq \frac{\Delta E}{2}$, the effective hamiltonian ruling the system can be written in a spin-dependent fashion [19], given by

$$H_{eff} = -2J(\mathbf{S}_a \cdot \mathbf{S}_b) \tag{2.2}$$

being $\mathbf{S}_a$, $\mathbf{S}_b$ the spin angular moments of the electrons $a$ and $b$. The sign of $J$ determines which state, either the triplet or the singlet, is favoured; if $J > 0$, from eqn (2.1) $E_S > E_T$, and so $\chi_T$ is favoured (the spins align parallel to each other), otherwise $\chi_S$ is preferred and $\mathbf{S}_a$, $\mathbf{S}_b$ point in opposite directions.

Even though generalizing the above argument to a many-body system is far from trivial, intuitively it is possible to infer that interactions such as that in eqn (2.2) also apply between all neighbouring atoms inside a crystal. This reasoning motivates the so-called *Heisenberg Hamiltonian*, expressed as:

$$H = -2 \sum_{i>j} J_{ij} (\mathbf{S}_i \cdot \mathbf{S}_j) \tag{2.3}$$

where the summation runs over each pair of spins only once, and $J_{ij}$ is the exchange integral characterizing the $(i,j)$-*th* couple. Since $J$ strongly depends on the overlap of the electronic wave functions (see eqn (2.1)), in practical calculations the summation is carried over only nearest or next-nearest crystal sites, neglecting longer-range interactions. Considering the spin operators as classical vectors, starting from eqn (2.3) and after some rearrangements, the exchange energy can be modelled by

$$E_H = A \int_V [(\nabla m_x)^2 + (\nabla m_y)^2 + (\nabla mz)^2] d\tau \tag{2.4}$$

where the integration is over the whole ferromagnet and $m_i$ are the cartesian components of the unit vector $\mathbf{m} = \mathbf{M}/M_S$. The parameter $A$ [J/m], appearing in eqn (2.4) and termed *exchange stiffness*, is defined through

$$A \doteq 2JS^2 \frac{z}{a}$$

being $z$ an integer depending on the crystalline structure of the material, $a$ its lattice constant and $J$ the exchange integral between first neighbouring sites. As stated in the eqn (2.4), the larger is $A$, the heavier is the weight of the exchange interaction within the total energy, the 'firmer' is the magnetization configuration. Moreover, being material specific and accounting for the effective number of nearest neighbour pairings, exchange stiffness $A$ is an useful and concise term for cross substance comparison. Typical values for ferromagnetic elements are in the range of tens of pJ/m.

### 2.1.2 Dipolar energy and Zeeman interaction

The dipolar energy, or *magnetostatic self-energy*, concerns the interplay of the magnetic body with the field it creates by itself, also known as the *demagnetizing field* $\mathbf{H}_d$. It fundamentally consists in the mechanical work required to arrange the magnetic moments inside the material, bringing them from the infinity to their actual positions, so as to build up the final macroscopic configuration. The arising effects, resulting from interactions similar to the dipole-dipole ones, are rather weak compared to the exchange forces, but they extend over longer distances. Nevertheless, they are of capital importance in determining both the domain structure and the magnetization process.

For a continuous medium, in the absence of any currents or displacement currents, it is possible to write:

$$\nabla \times \mathbf{H} = 0 \tag{2.5}$$

In fact, the above restriction of zero currents does not lead to a particular case; namely, it is always fair to split magnetic fields into two categories: the ones externally applied ($\mathbf{H}_a$), and the one originating 'ab initio' from the microscopic internal lattice ($\mathbf{H}_d$). As long as these contributions are superimposed, there is no loss of generality with the notation of (2.5), which exclusively refers to $\mathbf{H}_d$.

General solutions of the previous equation can be formed by introducing a scalar magnetostatic potential $U$. The customary convention is to define it through a minus sign:

$$\mathbf{H} \equiv -\nabla U \tag{2.6}$$

Combining eqns (2.5) and (2.6), and making use of the constitutive relation $\mathbf{B} = \mu_0(\mathbf{H} + \gamma_B \mathbf{M})$, being $\mu_0$ the vacuum magnetic permeability constant, $\gamma_B$ the Brown factor (equal either to 1 or to $4\pi$ in SI and cgs units respectively) and $\mathbf{H} = \mathbf{H}_a + \mathbf{H}_d \equiv \mathbf{H}_d$ in our assumption, one at the end obtains the Poisson-like equation

$$\nabla^2 U = \gamma_B \nabla \cdot \mathbf{M} \tag{2.7}$$

which should be valid inside the ferromagnet only. The magnetization $\mathbf{M}$

vanishes identically outside of it, so that $\mathbf{B} \equiv \mu_0 \mathbf{H}_d$ and $\nabla^2 U = 0$ elsewhere. Taking advantage of the interfacial continuity requirements for the fields, directly arising from the Maxwell's equations, these boundary conditions for $U$ follow:

$$U_{in} = U_{out}\,, \qquad \frac{\partial U_{in}}{\partial \mathbf{n}} - \frac{\partial U_{out}}{\partial \mathbf{n}} = \gamma_B(\mathbf{M}\cdot\mathbf{n}) \tag{2.8}$$

where $\mathbf{n}$ is a unit vector normal to the surface of the magnetic body, taken to be positive in the outward direction. Looking at eqns (2.7) and (2.8), a significant electrostatic analogy can be pulled out. Indeed, by comparing eqn (2.7) with the Gauss theorem written in terms of the electric potential $V$, i.e. $\nabla^2 V = -\frac{\rho}{\epsilon_0}$, the same formal role is played both by the charge density $\rho$ and $\nabla\cdot\mathbf{M}$. Pushing further this equivalence, the scalar product $\mathbf{M}\cdot\mathbf{n}$ in eqn (2.8) offers a mathematically convenient way of representing surface 'magnetic charges', since the analogous density of the polarization charge $\sigma_P$ equals to $\sigma_P = \mathbf{P}\cdot\mathbf{n}$. Therefore, the volume magnetization inhomogeneity, as well as its discontinuity at the body enclosing surfaces, can be regarded as sources for internal demagnetizing fields and external stray fields.

Once $U$ is get for the whole space, $\mathbf{H} \equiv \mathbf{H}_d$ is straightforwardly calculated from (2.6). The corresponding energy is then evaluated as:

$$E_M = -\frac{\mu_0}{2}\int_V \mathbf{H}_d\cdot\mathbf{M}d\tau \tag{2.9}$$

Eqn (2.9) reads as the sum of the interactions of each dipole with the demagnetizing field generated by all the others, with the prefactor 1/2 to avoid counting twice the interaction among each pair of magnetic moments.

When an external magnetic field $\mathbf{H}_a$ is imposed, it tends to cant the total magnetization towards its direction, and thus an additional energy contribution appears, similar to the previous one, called *Zeeman coupling*:

$$E_Z = -\mu_0\int_V \mathbf{H}_a\cdot\mathbf{M}d\tau \tag{2.10}$$

### 2.1.3 Magnetic anisotropy terms

The Heisenberg hamiltonian discussed in Paragraph 2.1.1 is totally *isotropic*, meaning that its energy levels do not depend on the particular direction along which the crystal is magnetized, all being equivalent. However, in order to account for the remanent magnetization, i.e. magnetization at zero external field, other energy terms should be included [20]. Indeed, termed $\alpha$ the angle between $\mathbf{M}$ and $\mathbf{H}_a$, not all its values are actually equally probable. Especially, one of the leading root of preferential orientations for $\mathbf{M}$ resides in the so-called *magnetocrystalline anisotropy*, caused by the blended action of both the crystal field and the spin-orbit coupling. Consequently, there exist specific directions in space in which it is easier to magnetize a given crystal, accordingly called *easy axes*, and others, named *hard axes*, which are less energetically favourable. The energy penalty to be paid in the latter circumstance can be expressed as a direction-dependent energy density function $e_{\mathrm{AN}}$, which is customarily quite small. In fact, while this contribution basically rules the *direction* along which $\mathbf{M}$ lies, the *magnitude* of the magnetization is determined almost only by the exchange.

Modelling the above anisotropy is always accomplished by means of parametric approximations, aiming to phenomenologically depict the proper magnetic landscape throughout the medium. In this regard, within each volume elements $\Delta V$ forming the body (see Section 2.1) a common choice consists in writing an expression for $e_{\mathrm{AN}}(\mathbf{M})$ as a series of trigonometric functions:

$$e_{AN} = k_0 + k_1 \sin^2\theta + k_2 \sin^4\theta + .. \tag{2.11}$$

In the eqn (2.11), $\theta$ is the polar angle between $\mathbf{M}$ and an anisotropy axis, say $z$, about which a rotational symmetry is supposed, and the coefficients $k_0$, $k_1$, etc. are material specific and depend on temperature. Retaining just the first two terms, the sign of $k_1$ determines the resulting configuration: if it is positive, the convenient angle is $\theta = \frac{\pi}{2}$, and thus $\mathbf{M}$ lays in the $(x, y)$ plane, otherwise the magnetization follows the $z-$axis, being the minima $0, \pi$.

This formalism is for instance particularly appropriate for a hexagonal crystal where, replacing $z$ with the $c$-axis, the uniaxial anisotropy approximation of eqn (2.11) holds. Anyway, regardless of the actual symmetry, if $\mathbf{M}$ varies in space an integration on the whole macroscopic magnetic volume must be performed, thus becoming the energy:

$$E_{AN} = \int_V e_{AN} d\tau \tag{2.12}$$

Besides the aforementioned contribution, another intrinsic term spontaneously arises from the system geometry. Indeed, when the specimen is a uniformly magnetized ellipsoid, the demagnetizing field $\mathbf{H}_d$ can be expressed trough a second order tensor $\overline{\mathbf{N}}$, whose trace is unitary and elements depend on the sample shape:

$$\mathbf{H}_d = -\overline{\mathbf{N}} \cdot \mathbf{M}$$

Once $\overline{\mathbf{N}}$ is put in a diagonal form, the magnetostatic self-energy of the body, stated by the eqn (2.9), can be rewritten as:

$$E_M^{'} = \frac{\mu_0}{2} \int_V (N_x M_x^2 + N_y M_y^2 + N_z M_z^2) d\tau \tag{2.13}$$

In this equality $N_x$, $N_y$ and $N_z$ are universally known as *demagnetizing factors* and their magnitudes abide by the ratios of the ellipsoid principal axes: two ellipsoids with the same contours, but occupying different volumes, have the same $\overline{\mathbf{N}}$. As a result, $E_M^{'}$ is thus conditioned by the aspect of the ferromagnet, which consequently impacts also in the orientation of $\mathbf{M}$, giving rise to a supplemental *shape anisotropy*. It is worth to notice that eqn (2.13) can be exploited for instance for thin films, which can be thought as 'extreme' oblate spheroids, just the way a prolate one (which is a kind of rugby ball) could stand for a cylinder.

### 2.1.4 Magnetic domains and domain walls

Exchange interaction, dipolar energy and magnetic anisotropy make up the major pieces of the puzzle portraying the idealized behaviour of a single-domain magnetic body. However, as conveyed in the related eqns (2.4), (2.9), (2.10) and (2.12), to describe real scenarios, an integration over the *macroscopic* volume of the magnet is always required. Indeed, bulk ferromagnets break in magnetic *domains*, which are portions of space uniformly magnetized along different directions. Theories, such as micromagnetism, calculate the magnetization attained inside each of these regions, and then properly sum up all the contributions to foresee magnetic equilibrium states.

Nowadays, the existence of magnetic domains is a well-established fact, being their boundaries, *domain walls* (DWs), observed by several experimental methods (see for instance MFM and STXM techniques, explained in Paragraphs 3.2.2 and 3.2.3). Nonetheless, despite they were first introduced in 1906 by Weiss [21], their origin has been strongly debated for long time. To this purpose, it is worth noting that neither the exchange coupling nor anisotropy effects can singularly account for subdividing a piece of magnetic material into such domains. Their formation is indeed a consequence of the minimization of the magnetostatic self-energy.

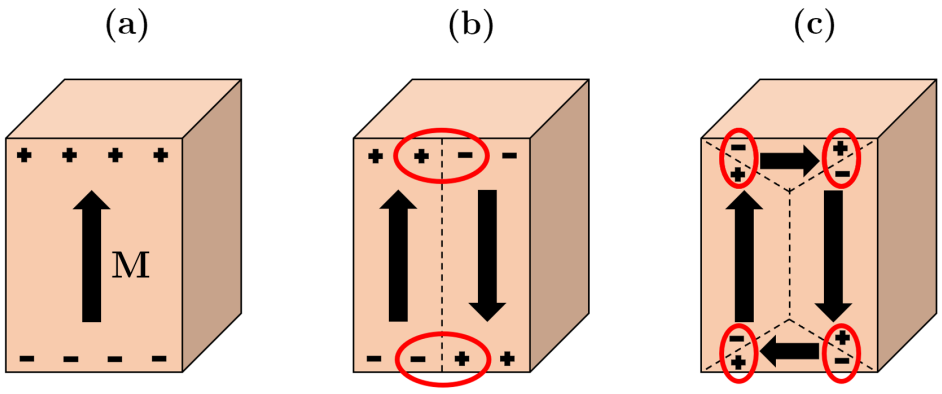


**Figure 2.1:** Magnetic domains formation. From **(a)** to **(c)** the magnetic charges, sources for the demagnetizing field $\mathbf{H}_d$, progressively decrease, thus minimizing the corresponding dipolar energy too.

Indeed, by arranging its internal 'magnetic' volume in a proper partition, the ferromagnetic crystal is able to reduce the sources of the demagnetizing field $\mathbf{H}_d$, discussed in Paragraph 2.1.2, therefore lowering the corresponding weight of eqn (2.9). In this regard, the optimal solution would consist in a magnetization flux closure state (see Figure 2.1), where $\mathbf{M}$, by following the shape of the body, always lies parallel to its surfaces, thus nullifying both the volume ($\nabla \cdot \mathbf{M} \approx 0$) and the surface ($\mathbf{M} \cdot \mathbf{n} \equiv 0$) magnetic charges (*charge avoidance principle*). However, each configuration in which $\mathbf{M}$ spatially varies, bumps into the other energy contributions. In fact, on the one hand the exchange tries to align *all* the spins parallel to each other, on the other hand the anisotropy favours only *few* preferential directions in space. Hence, the formation of multiple differently oriented domains, albeit mainly promoted by the dipolar energy, ultimately arises as a consequence of the interplay among all these terms together. Especially, it results as a balance between the energy cost due to the presence of $\mathbf{H}_d$ and the one demanded for the domain wall formation.

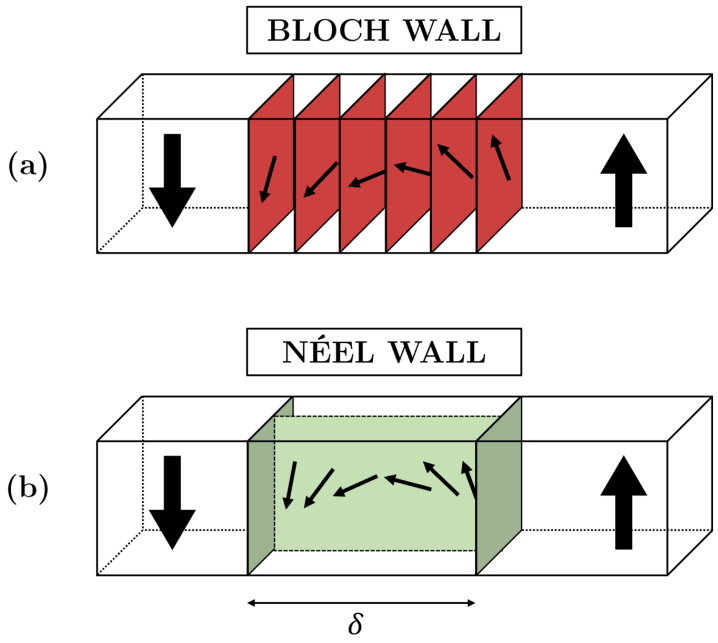


**Figure 2.2:** Schematic of a Bloch domain wall **(a)** and a Néel domain wall **(b)**.

DWs are the border interfaces in the middle of two adjacent domains, where the magnetization flips under the opposing influences of exchange and anisotropy (see Fig. 2.2). Indeed, the former promotes the parallel alignment of the spins and limits the shortest rotation distance for **M**. The anisotropy, on the other hand, sets the energetically favourable direction for the spin orientation, determining an upper limit for the rotation distances. The effective width $\delta$ of a DW is therefore established by the compromise between these two terms. Moreover, depending on the characteristic spin arrangement across the wall, two main types of DWs can be distinguished: *Bloch* and *Neél* walls. Within a Bloch DW, usually found in thick ferromagnetic films and bulk samples, the plane where **M** rotates is parallel to the wall, so that its divergence vanishes identically inside ($\nabla \cdot \mathbf{M} \equiv 0$), and only surface magnetic charges possibly develop. On the contrary, a Neél DW perpendicularly evolves respect to the domains boundaries, thus ideally avoiding surface charges, though volume ones appear instead ($\nabla \cdot \mathbf{M} \neq 0$). Because of the stray field created by the last, normally Neél DWs are higher in energy than Bloch DWs, and tend to be favoured in thin films only (thinner than $\delta$), where a dipolar energy cost should be paid in rotating the spins out-of-plane.

### 2.1.5 Brown equations

The issue of determining equilibrium magnetic states is mathematically complex to face, since the general arguments of the previous paragraph can be used as guide-lines only. An attempt to simplify the task to manageable proportions was firstly tried through the so-called *domain theory*. Within this approach, the total energy $E_{tot}$ of certain domain configurations is estimated, and then the one related to the lowest $E_{tot}$ is identified. However, this method suffers from the serious drawback connected to the risk of ignoring some configurations [20].

Instead, by reading the actual initial problem in terms of a variational minimization procedure, its rigorous solution for a ferromagnetic body of arbitrary shape has been first accomplished in 1940 by Brown [22]. Indeed, collecting the results achieved in Paragraphs 2.1.1, 2.1.2 and 2.1.3 in a sin-

gle equation, the following formulation for the total free energy functional $E_{tot}(\mathbf{m})$ holds, uniquely associated to a spatial distribution $\mathbf{m}(\mathbf{r}) \equiv \mathbf{M}(\mathbf{r})/M_S$ (neglecting temperature):

$$\begin{aligned} E_{tot}(\mathbf{m}) = \int_V \Big\{ & A[(\nabla m_x)^2 + (\nabla m_y)^2 + (\nabla mz)^2] + \\ & - \frac{\mu_0}{2} M_S(\mathbf{m} \cdot \mathbf{H}_d) - \mu_0 M_S(\mathbf{m} \cdot \mathbf{H}_a) + e_{AN} \Big\} d\tau \end{aligned} \tag{2.14}$$

Known the expression for $\mathbf{m}(\mathbf{r})$, $E_{tot}$ accordingly derives, yet the duty here is to find $\overline{\mathbf{m}}(\mathbf{r})$ so that this energy is a minimum. Albeit the detailed analysis of the whole computation is beyond the scope of the present work, Brown minimized eqn (2.14) by considering small variations of the magnetization vector $\mathbf{m}$, bound to the constraint $|\,\mathbf{m}(\mathbf{r})\,| = 1$, and by evaluating the corresponding modifications in each term of eqn (2.14). The arising stable magnetic texture at the end produce local energy minima of the magnetic configurational space such that

$$\begin{cases} \overline{\mathbf{m}} \times \mathbf{H}_{eff} = 0 \\ \dfrac{\partial \overline{\mathbf{m}}}{\partial \mathbf{n}} = 0 \end{cases} \tag{2.15}$$

being $\mathbf{n}$ a unit vector normal to the surface of the magnetic body, and $\mathbf{H}_{eff}$ an effective magnetic field of the form:

$$H_{eff} = \frac{A}{\mu_0 M_S} \nabla^2 \overline{\mathbf{m}} + \mathbf{H}_d + \mathbf{H}_a - \underbrace{\frac{1}{\mu_0 M_S} \frac{\partial e_{AN}}{\partial \overline{\mathbf{m}}}}_{\text{Anisotropy Field}} \tag{2.16}$$

Eqns (2.15) and (2.16) are named *Brown equations* and state that equilibrium magnetic configurations are found by making $\mathbf{m}(\mathbf{r})$ lie parallel everywhere to the field $\mathbf{H}_{eff}(\mathbf{r})$, which comprehends all the material-specific parameters seen so far. Depending explicitly on the searched unknown $\overline{\mathbf{m}}(\mathbf{r})$, the Brown equations are not linear and must be recursively solved until an approximated solution is attained.

Apart from the equilibrium solution, these equations represent the basis for the subsequent calculation of the dynamic behaviour of the magnetization. Indeed, as in classical magnetism, an elementary magnetic moment $\boldsymbol{\mu}$ in a

external magnetic field is subjected to a torque $\boldsymbol{\tau}$ which aligns it parallel to $\mathbf{B}$. Since $\boldsymbol{\mu}$ is primarily associated with the intrinsic angular momentum $\mathbf{S}$, and because $\boldsymbol{\tau}$ is equal to rate of change of angular momentum, it is fair to write the following equation, called *Landau–Lifshitz equation* [23]:

$$\frac{d\boldsymbol{\mu}}{dt} = \gamma\boldsymbol{\mu} \times \mathbf{B} \quad \Longrightarrow \quad \frac{d\mathbf{m}}{dt} = -\gamma_0 \mathbf{m} \times \mathbf{H}_{eff} \tag{2.17}$$

having exploited $\mathbf{B} = \mu_0 \mathbf{H}_{eff}$ and defined $\gamma_0 \doteq -\gamma\mu_0$ as an effective gyromagnetic ratio. To some extent, the first equation in (2.15) can be thought as a particular case of eqn (2.17), giving the magnetic landscape when there is no variation in time. It is worth to notice that eqn (2.17) would depict an undamped precession of $\mathbf{m}(\mathbf{r})$ around $\mathbf{H}_{eff}(\mathbf{r})$, which potentially lasts for ever. To account for the finite time spent by $\mathbf{m}$, or equivalently $\mathbf{M}$, to reach stationary conditions in everyday situations, a dissipative mechanism must be phenomenologically added. To include it, one can modify eqn (2.17) into

$$\frac{d\mathbf{M}}{dt} = -\gamma_0 \mathbf{M} \times \left( \mathbf{H}_{eff} - \eta \frac{d\mathbf{M}}{dt} \right) \tag{2.18}$$

where $\eta$ is a fitting damping parameter, which is inversely proportional to the transient after which $\mathbf{M}$ locally lines up to $\mathbf{H}_{eff}$. Eqn (2.18) is termed *Gilbert equation* [24], or LLG equation.

## 2.2 Interfacial effects

Considering the same substance, its magnetic properties for bulk samples may appreciably differ compared to the ones measured in nanoscale magnets. Actually, scaling down the features of a specimen, a threshold, the so-called *exchange length* $l_{ex}$ (typical values in 2–5 nm range), marks the entrance into the 'small' regime. It is given by the formula

$$l_{ex} \doteq \sqrt{\frac{A}{\mu_0 M_S^2}}$$

being $A$ the exchange stiffness of the substance and $M_S$ its saturation magnetization, and it provides the shortest scale on which $\mathbf{M}$ can be twisted in order to minimize the dipolar interaction. Moreover, it coincides with the lower bound for the domain wall (DW) width $\delta$ of Paragraph 2.1.4, and it also defines the size $\Delta V$ of the mesh to adopt within the micromagnetic framework (see Section 2.1). From the comparison with $l_{ex}$, magnetic systems can be classified as *thin films*, *nanowires* and *nanoparticles*, which present one, two or three 'small' dimensions, respectively.

Thin films are the most versatile magnetic nanostructures, and the underlying physics governing their intrinsic characteristics is quite different from the one ruling the macroscopic case. Especially, in thin-film heterostructures, as those addressed in Chapters 4 and 5, several effects arise from the reduced symmetry at the interfaces (here an outer spin has half the pairings with respect to its counterpart deeply inside the volume), and according to the chemistry of the materials pulled together (which possibly give rise to even distinct environments for the surface spins). A strong dependence on the films thickness $t$ is a common thread shared by all these new arising phenomena, whose magnitude diminishes as $t$ increases. Indeed, such interactions usually follow an empirical decreasing power-law in $t$ (see next paragraph), though they are not only the consequence of the last interfacial atomic layers. In this regard, they can be promoted by epitaxial stress, modified electronic structures, surface or growth-induced texturization, variations in the exchange local landscape, etc. Nevertheless, irrespective of their origins, from a phenomenological point of view any additional surface energy term can be ultimately read as a sort of anisotropy, entailing a tendency for the surface spins to lie either parallel or perpendicularly to the surface itself.

### 2.2.1 Exchange bias

The essential building block allowing the magnetic pattering of the devices discussed in Chapter (4) is a bilayer, composed of a ferromagnetic and an antiferromagnetic film in contact with each other. In this heterostructure, the coupling between the two layers leads to the stabilization of a unidirectional

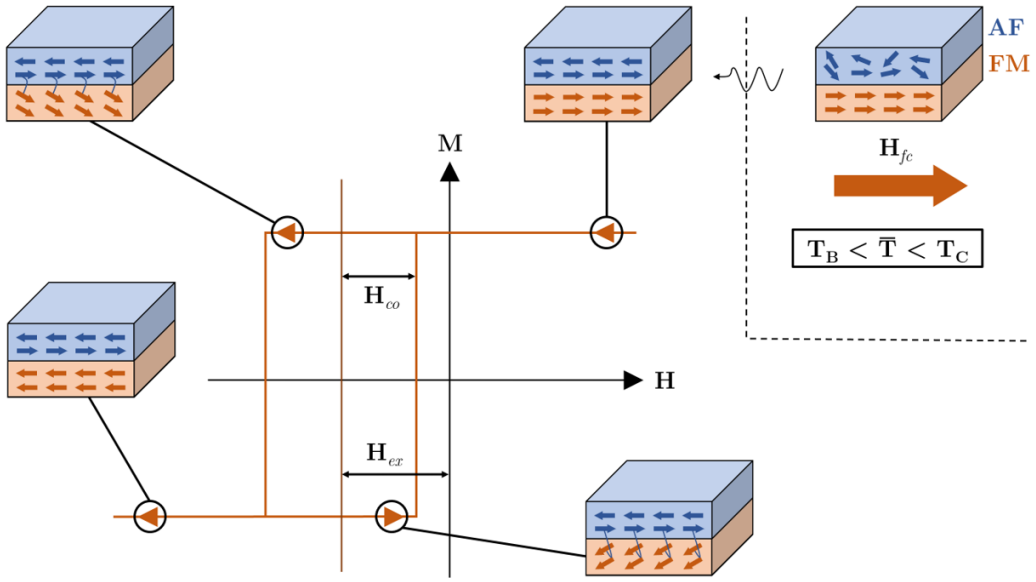


**Figure 2.3:** Establishing the exchange bias by the field cooling procedure, and its effect on the hysteresis loop of a ferromagnetic layer. The dashed panel, on the upper-right side of the image, summarizes the necessary conditions for setting the exchange bias. If $T_B < \overline{T} < T_C$, the external field $\mathbf{H}_{fc}$ is able to cant the spins inside the ferromagnetic layer towards its direction, for the subsequent reorganization of the antiferromagnet. By cooling the system at room temperature while keeping the field on, the exchange bias eventually determines the spin texture pointed by the zig-zag arrow. The sketched hysteresis loop shows the behaviour of the bilayer by sweeping a magnetic field $\mathbf{H}$ parallel to $\mathbf{H}_{fc}$. Note that the spin configurations are not necessarily accurate portraits of the actual rotation of the FM or AF spins.

anisotropy, discovered in 1956 by Meiklejohn and Beam [25]. The effect they first experimentally observed, later named *exchange bias*, was a shifted and stretched hysteresis loop for the investigated systems (Co particles embedded in their native antiferromagnetic oxide). Despite more than 60 years have passed from its first appearance, the exact microscopic origin of this surface phenomenon is still unclear and a lot of theories have been proposed until now [26]. Nonetheless, it has been exploited in a variety of different structures which find practical applications in several magnetic storage devices [27].

Exchange bias is an interfacial exchange interaction which consists in the pinning of the magnetization of a ferromagnet (FM) through an antiferromagnet (AF). The results of such a behaviour are sketched in Fig. 2.3 and phenomenologically consist in displacing the hysteresis loop of the FM, by

an amount equal to $\mathbf{H}_{ex}$, and in altering its coercive field $\mathbf{H}_{co}$. The direction of the bias and its strength (the latter only for polycrystalline films) can be arbitrarily set by cooling the bilayer in a suitable external field (*field cooling*), from a specific temperature $\overline{T}$. The last must fulfil two constraints at the same time: on the one hand it has to be lower than the Curie temperature $T_C$ characterizing the FM, on the other hand it needs to exceed $T_B$, known as the *blocking temperature* of the AF, and thus $T_B < \overline{T} < T_C$. Though $T_B$ is unambiguously defined as the temperature at which $\mathbf{H}_{ex}$ vanishes, its attained value is not unique instead, being affected by the thickness $t_{AF}$ of the AF. Indeed, while in a bulk AF it basically corresponds to the Néel temperature $T_N$ (the one at which the antiferromagnetic order is lost), scaling the AF film thickness it becomes smaller and smaller, approximately following a power-law in $t_{AF}$ [28].

Consider the dashed panel in Fig. 2.3. As $T = \overline{T}$, the magnetic order inside the AF is lost (since $\overline{T} > T_B$), consequently unlocking the interfacial spins of the FM. On the contrary, due to the extra aforementioned requirement $\overline{T} < T_C$, the FM spin configuration retains its original arrangement, whose overall direction in space can be now tailored by applying an appropriate field $\mathbf{H}_{fc}$. Then, if the temperature of the system is gradually reduced while keeping constant $\mathbf{H}_{fc}$, due to the exchange interaction, the spins of the FM at the interface act as a template for restoring the magnetic order in the AF, which is completely re-constituted at room temperature ($< T_B$). At this stage, the removal of $\mathbf{H}_{fc}$ does not influence anymore the interfacial magnetic landscape established so far, made field-insensitive, from now on, thanks to the low susceptibility $\chi_{AF}$ of the recovered AF (being the last hardly directable by a magnetic field). As a result, by setting a *unidirectional* anisotropy along the direction of $\mathbf{H}_{fc}$, the exchange bias acts like a fictitious offset field $\mathbf{H}_{ex}$, as proved by the shifted hysteresis loop in Fig. 2.3. Accordingly, a unique direction for the magnetization is allowed at remanence.

Since the exchange bias strength is roughly found to inversely decrease with the FM thickness $t_{FM}$ [27], for an idealized single-domain ferromagnetic layer it can be modelled through:

$$e_{ex} \propto -\frac{\sigma_{ex}}{t_{FM}} \cos\phi \doteq -K_{ex} \cos\phi \tag{2.19}$$

with $\phi$ the angle between $\mathbf{M}$ and the direction of $\mathbf{H}_{fc}$, and $\sigma_{ex}$ the interfacial exchange energy per unit surface ($\sigma_{ex} \doteq \mid \mathbf{H}_{ex} \mid t_{FM} M_S$, whose typical values amount to few mJ/m$^2$) defining the effective anisotropy constant $K_{ex}$. Its contribution to the total energy of eqn (2.14) is thus simply given by integrating this term over the volume of the FM. However, it is important to highlight that (2.19) is just an attempt to qualitatively capture the true behaviour of the above phenomenon, whose real trend can follow more complex dependence on $t_{FM}$ [29, 30]. For instance, if $t_{FM}$ becomes of the order of few nm at most, the $1/t_{FM}$ relationship breaks down, likely because the FM film ceases to be continuous; in this regard, an important role is played by the adopted growth method, from which the FM microstructure derives (see Paragraph 3.1.1).

Albeit less explicitly, $\mathbf{H}_{ex}$ is also conditioned by the AF thickness $t_{AF}$ and its surface orientation [31]. Especially, the exchange bias is actually turned on by overcoming a lower threshold for $t_{AF}$, resulting from the competition between $\sigma_{ex}$ and the anisotropy governing the AF alone [32] (expressed by a proper term $K_{AF}$ [J/m$^3$]). Indeed, it turns out that, when $K_{AF} t_{AF} > \sigma_{ex}$, the AF 'rigidity' makes its spins to be unperturbed by the reorientation of the FM ones with the external magnetic field, giving rise to unidirectional anisotropy and exchange bias. Conversely, for $K_{AF} t_{AF} < \sigma_{ex}$, by sweeping $\mathbf{H}$ the spins of the AF tend to be canted as those of the FM (exchange spring), thus inhibiting the characteristic hysteresis loop shift. In fact, while $\mathbf{H}_{ex}$ saturates to a material-specific value for large $t_{AF}$ (and finally diminishes), a reduction of the last causes an abrupt decrease in $\mathbf{H}_{ex}$, until it eventually vanishes. In these circumstances the loop is only enlarged due to the enhanced coercivity of the system (FM+AF) as a whole.

## 2.3 Higher order energy terms

As it has been shown, the exchange bias can be thought as a first order correction to eqn (2.14), ruling the total energy for the case of particular magnetic heterostructures. Indeed, depending on the investigated system, other contributions can be considered 'ad hoc' to account for the observed experimental phenomena. This is exactly the case for the next paragraphs, in which two higher order energy terms are analysed, namely the interlayer exchange coupling (also known as *bilinear coupling*) and the Dzyaloshinsky-Moriya interaction. Throughout this thesis work, the former has made possible the development of the synthetic antiferromagnetic structures discussed in Chapter 4, and the latter has been exploited in defining the periodicity of the magnonic crystals of Chapter 5.

### 2.3.1 Interlayer exchange coupling

Interlayer exchange coupling is a phenomenon taking place in a trilayer composed by two ferromagnetic films, separated by a non-magnetic spacer, which gives rise to a parallel or antiparallel coupling of their magnetizations. It was first demonstrated in 1986 by experimental evidences in Fe/Cr structures and in manganites based multilayers [33, 34]. Following these preliminary results, a variety of systems, characterized by many different material combinations and structural properties, have been investigated. The interest in such heterostructures has been further enhanced by the discovery of an *oscillating behaviour* in the interlayer coupling with respect to the spacer thickness [35]. Various approaches have been developed so far in order to explain the observed phenomena, including the Ruderman-Kittel-Kasuya-Yosida (RKKY) model [36], the free-electron model [37], the Anderson (or s-d *mixing*) model [38] and so on. The mechanism explained in what follows is widely accepted, and it is based upon quantum interferences in the spacer layer due to spin-dependent confinement [39].

In trilayers with magnetic $3d$ elements, provided there are no significant anisotropy contributions, three kinds of alignment have been identified for the magnetizations within the two ferromagnetic films ($a$ and $b$): parallel

(P), antiparallel (AP) and 90°-type. Considering the simplest case of a paramagnetic/diamagnetic spacer, the following phenomenological expression for the interlayer coupling areal energy density $\overline{E}$ holds:

$$\frac{\overline{E}}{A} = -J_1 \frac{\mathbf{M}_a \cdot \mathbf{M}_b}{|\,\mathbf{M}_a\,| \cdot |\,\mathbf{M}_b\,|} - J_2 \left( \frac{\mathbf{M}_a \cdot \mathbf{M}_b}{|\,\mathbf{M}_a\,| \cdot |\,\mathbf{M}_b\,|} \right)^2 \equiv -J_1 \cos(\Delta\varphi) - J_2 \cos^2(\Delta\varphi)$$

with $\Delta\varphi$ the angle between $\mathbf{M}_a$ and $\mathbf{M}_b$. The constants $J_1$ and $J_2$ determine the type and the strength of the coupling: if $|\,J_1\,| \gg |\,J_2\,|$, from the minima of $\overline{E}$, the coupling is P (AP) for positive (negative) $J_1$, respectively; otherwise, when $J_2$ dominates (supposing $J_2 < 0$), the minimum is achieved for $\Delta\varphi = 90°$. Neglecting the $J_2$ term (called 'biquadratic'), since $E_P \doteq \overline{E}(0)/A = -J_1/A$ and $E_{AP} \doteq \overline{E}(\pi)/A = J_1/A$, the parameter $J_1$ can be written as:

$$J_1 = \frac{1}{2A}(E_{AP} - E_P) \tag{2.20}$$

and its typical values are on the order of few mJ/m$^2$ at most. To get aware of the magnitude of such a coupling, it is useful to compare this number with the one arising in a bulk ferromagnet due to the exchange on neighbouring atomic planes ($J_{IP}$). Assuming a reasonable exchange stiffness $A \approx 10$ pJ/m (see Paragraph 2.1.1) and an interplanar spacing $d \approx 1$ Å, at the end $J_{IP}$ results $J_{IP} \approx A/d = 100$ mJ/m$^2$. Here is why the present phenomenon can be customarily treated as an higher order energy correction, being its extent a percent of the direct exchange strength.

From eqn (2.20), evaluating the interlayer coupling is reduced to compute the energy difference between the AP and P configuration. This calculation can be significantly simplified through the *force theorem* [40], which affirms that the energy difference in eqn (2.20) can be esteemed by neglecting the mutual interactions among the spacer electrons, as to consider them as free particles, and by taking the difference in the sum of their single-particle-like energies in the two corresponding macroscopic states. Thus, firstly one develops approximations for the effective potentials in both cases, and then computes the sum of the single particle energies for every arrangement of $\mathbf{M}_a$ and $\mathbf{M}_b$. Assume that the ferromagnetic layers are semi-infinite and

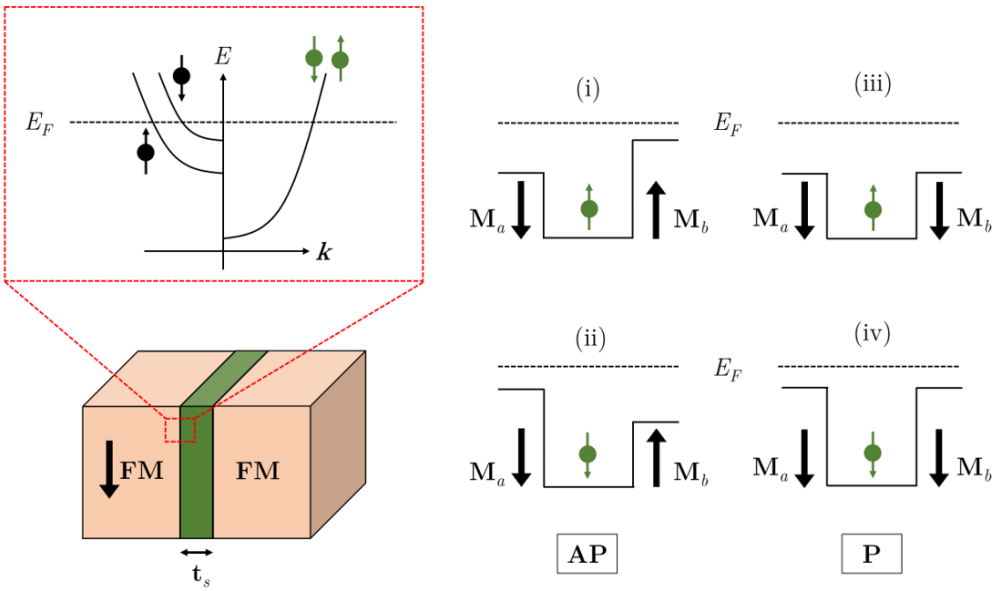


**Figure 2.4:** One-dimensional spin-dependent quantum wells experienced by either a spin-up (i)-(iii) or a spin-down (ii)-(iv) electron. The magnetization of the FM '$a$' points downwards while $\mathbf{M}_b$ points either up or down. The height of the edges of the potential barriers depends on both the spin character of the electron and the nearby magnetization direction. The red dashed panel shows a 'nearly-matched' exchange-split interface among the pinned FM on the left and the central spacer material. Both the exchange-split bands of the FM lie near in energy with respect to the spin-independent energy band of the spacer (a simplified free electron model is assumed).

the spacer thickness $t_S$ large enough to construct the effective potentials piecewise. Furthermore, supposing perfectly flat interfaces characterized by 'nearly-matched' exchange-split free electron band structure (see Fig. 2.4), and collinear magnetizations (meaning the majority and minority carriers do not interact with each other), the problem is reduced to computing the single particle energies for the four quantum wells depicted in Fig. 2.4.

Inside the middle layer, conduction electrons basically experience the same potential as in the bulk material; deviations from it are confined to the interfaces. Here, an electron moving from the spacer to the FM, and described through a plane wave $\psi$ labelled with the wavevector $\boldsymbol{k}$, can be partially reflected. Because of the spin-polarization of the ferromagnet, the potential deviation is spin-dependent, and so do the reflection coefficients $R_i^s$.

Especially, they depend on the specific spin character of the carrier (either majority '$s = \uparrow$' or minority '$s = \downarrow$'), which needs to be evaluated, for each interface, referring to the magnetization in the adjacent FM (see Fig. 2.4). Within a simplified one-dimensional quantum well model, which nevertheless contains the essential physics involved in the phenomenon, the $R_i^s$ coefficients can be written as $R_{a,b}^s = r_{a,b}^s \exp(i\phi_{a,b})$, where $a$, $b$ stand for the two ferromagnetic layers, and $s$ for the electron spin type. Hence, by substituting $\boldsymbol{k}$ with its 1D version $k_\perp$, and considering that after a round trip the electron is eventually reflected by both interfaces, the phase of the wave function $\psi$ changes according to:

$$\Delta\phi = 2k_\perp t_S + \phi_a + \phi_b$$

The waves interference, due to multiple reflections on the barriers, induces a modification of the density of states $\rho$ in the spacer layer for the electronic state ($k_\perp$) under consideration. Indeed, the amplitude of $\psi$ is finally given by summing up all the possible round trips (*phase accumulation model*):

$$\sum_{n=1}^{\infty} \left[ r_a^s r_b^s e^{i\Delta\phi} \right]^n = \frac{r_a^s r_b^s e^{i\Delta\phi}}{1 - r_a^s r_b^s e^{i\Delta\phi}} \tag{2.21}$$

and a constructive interference for $\psi$ thus occurs whenever the denominator of (2.21) is minimized, i.e. for

$$\Delta\phi = 2k_\perp t_S + \phi_a + \phi_b = 2n\pi \tag{2.22}$$

with $n$ an integer number. Constructive interference inside the spacer gives rise to *resonances*, frequently referred to as *Quantum Well States* (QWSs), characterized by an *increase* of the density of states $\rho$. Conversely, for destructive interferences $\Delta\phi = (2n+1)\pi$, one has a *reduction* of $\rho$. For energies less than the potential barrier height, $r_a^{\uparrow,\downarrow} = r_b^{\uparrow,\downarrow} = 1$, and from (2.21), one gets perfect bound states with a well defined energy; otherwise, due to the spreading of the waves amplitude into the surrounding FMs, the QWSs become 'broader' resonances. Moreover, since $\Delta\phi$ depends on the spacer thickness $t_S$, as it varies, the resonances shift in energy: if there is such a state at the Fermi energy $E_F$ for a thickness $\overline{t_S}$, then another one passes through

$E_F$ for $t_S = \overline{t_S} + 2n\pi/2k_F$, being $k_F$ the Fermi wave vector of the spacer layer. This periodic crossing (period $\Delta = 2\pi/2k_f$) of the Fermi level by QWSs as a function of $t_S$, is the exact origin of the oscillations in the interlayer exchange coupling parameter $J_1$. In fact, the QWSs affect the density of states $\rho$ of the heterostructure, which in turn influences the overall energy by altering the single particle energy levels distribution. Therefore, by properly treating the effective change in the density of states $\Delta\rho$ due to electron confinement, the energy of each configuration in Fig. 2.4 can be derived. The parameter $J_1$ is then simply given by the energy difference between the configurations (i)+(ii) and (iii)+(iv). In the limit of large $t_S$ and small reflection coefficients, such that $R_a^{\uparrow} = R_b^{\uparrow} \doteq R^{\uparrow}$ and $R_a^{\downarrow} = R_b^{\downarrow} \doteq R^{\downarrow}$, with $R^{\uparrow} \neq R^{\downarrow}$, $J_1$ can be expressed as [40]:

$$J_1 \propto Re\left[\left(R^{\uparrow} - R^{\downarrow}\right)^2 e^{i2k_f t_S}\right] \tag{2.23}$$

Relation (2.23) catches the very heart of the interlayer exchange coupling, by actually showing an oscillating behaviour of $J_1$ (spatial period equals to $\Delta = 2\pi/2k_f$) which ultimately arises due to the sharp cut-off in momentum space of the spacer Fermi surface.

The extension to more realistic three-dimensional multilayers is straightforward under the hypothesis of *coherent interfaces* [39, 41], which preserve the in-plane translational invariance throughout the space. Hence, the in-plane component $\mathbf{k}_{\|}$ of the electronic wave vector is conserved upon reflection, and a suitably one-dimensional-like quantum well picture can be recast.

### 2.3.2 Dzyaloshinsky-Moriya interaction

In Paragraph 2.1.1, an implicit assumption lead to the eqn (2.4). Especially, the exchange integrals $J_x$, $J_y$, $J_z$ were supposed to be all identical. Either the cases in which only two of the $J_i$ are the same, and the one where $J_x \neq J_y \neq J_z$ (named Heisenberg 'XXZ' and 'XYZ' models respectively), are analytically solvable too. However, besides these *anisotropy* exchange interactions and those described in Paragraph 2.1.3, other types of anisotropies may also be present in real systems. Certain crystals, such as $\alpha$-$Fe_2O_3$ or $MnCo_3$, exhibit

a weak spontaneous magnetization, though neutron diffraction measurements have confirmed their spin arrangements to be mainly antiferromagnetic [42]. Such phenomena cannot be explained either in terms of an imbalance between the sublattices magnetizations inside the AFs, or by means of antiferromagnetic domains with magnetized domain walls (DWs), as first speculated [43]. The problem, whether this *weak ferromagnetism* could be an intrinsic property of specific materials, was faced by Dzyaloshinskii in 1957 [44]. Based on a symmetry reasoning, he proposed an argument where the spin-spin coupling, responsible for the observed behaviour in $\alpha$-$Fe_2O_3$, was suggested to be antisymmetrical in nature, and expressible through:

$$H_{DM} = \mathbf{D} \cdot (\mathbf{S}_1 \times \mathbf{S}_2) \tag{2.24}$$

with $\mathbf{D}$ a vector (possibly null; see hereafter) either parallel or perpendicular to the line joining the two spins. Later, Moriya [45] provided the underlying microscopic mechanism for (2.24) by extending Anderson's superexchange theory [46] to include *spin-orbit interaction*. The above term was thus dubbed Dzyaloshinsky-Moriya interaction (DMI).

In addition to explaining the weak ferromagnetism of some antiferromagnetic compounds, hamiltonians of the type (2.24) rule a wide variety of physical systems, and are currently the subject of intense research due to their capability to induce the formation of chiral-spin textures [47, 48].

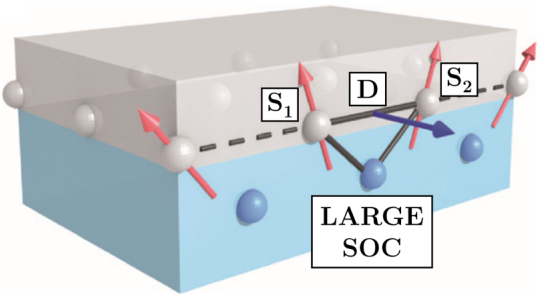


**Figure 2.5:** Schematic of the interfacial DMI based on the three-site Fert-Levy model between a ferromagnet (grey) and a strong spin-orbit coupling (SOC) heavy metal (blue). The interaction tilts the spins in the ferromagnetic film with respect to the parallel order. The image is adapted from [47].

Besides a strong spin-orbit coupling, the essential ingredient at the root of DMI is the lack of inversion symmetry. Especially, the vector $\mathbf{D}$ appearing in eqn (2.24) vanishes every time the crystal field has a centre of inversion located at the midpoint of the line connecting the spins $\mathbf{S}_1$ and $\mathbf{S}_2$ [44]. Since most *bulk* substances are inversion symmetric, the arising effects due to DMIs are thus typically irrelevant. Conversely, in ultrathin ferromagnetic films in contact with nonmagnetic heavy metal (HM), noticeable interfacial DMIs are allowed from the broken inversion symmetry at the interfaces. Here, the coupling originates from a three-site indirect exchange mechanism [49], involving two spins at the outer surface of the FM and a neighbouring HM atom having a large spin-orbit coupling (see Fig. 2.5). In such heterostructures, which are exactly those discussed in Chapter 5, the vector $\mathbf{D}$ results to be perpendicular to the plane identified by the triangle whose vertexes coincide with $\mathbf{S}_1$, $\mathbf{S}_2$ and the HM atom; a quantitative evaluation for the direction of $\mathbf{D}$ in this kind of systems can be performed as in [50].

A key insight of the behaviour governing the microscopic spins arrangement in the presence of DMIs can be straight derived from the expression of $H_{DM}$. Indeed the energy corresponding to eqn (2.24) is minimized (i.e. it is negative) when the two spins $\mathbf{S}_1$ and $\mathbf{S}_2$ are forced to be at 'right' angles in a plane perpendicular to $\mathbf{D}$, and hence the coupling described in eq (2.24) very often acts to rotate them. In fact, albeit the exact derivation of (2.24) falls well outside the purpose of the present work, it is quite easy to show the related *spin canting* effect. In this regard, consider a linear ferromagnetic chain of $N$ sites where a Dzyaloshinsky-Moriya-like term is added to the exchange coupling described by eqn (2.4). The overall hamiltonian thus results as:

$$H = -2J_1 \sum_i \mathbf{S}_i \cdot \mathbf{S}_{i+1} + J_2 \sum_i (\mathbf{S}_i \times \mathbf{S}_{i+1}) \cdot \hat{\mathbf{z}} \tag{2.25}$$

where the interactions are assumed to be effective only among nearest neighbours, $\mathbf{D}$ points along the $z$-axis ($\mathbf{D} = J_2\hat{\mathbf{z}}$) and $J_1 > 0$ is the usual exchange integral introduced in Paragraph 2.1.1. Let the spins $\mathbf{S}_i = (S_i^x, S_i^y)$ be classical vectors in the plane $(x, y)$, with $S_i^x = \cos(\alpha_i)$ and $S_i^y = \sin(\alpha_i)$. Whereas the first term in (2.25) favours parallel neighbouring pairs, the second is min-

imized when the spins are perpendicular to each other. Eqn (2.25) can be rewritten as:

$$H = -\sum_{i=1} \left[ 2J_1 \cos(\alpha_i - \alpha_{i+1}) + J_2 \sin(\alpha_i - \alpha_{i+1}) \right] \tag{2.26}$$

Defining $\phi \doteq \tan^{-1}\left(\frac{J_2}{2J_1}\right)$, $\phi \in [0, \pi/2]$, the hamiltonian (2.26) lastly becomes:

$$H = -\frac{2J_1}{\cos\phi} \sum_i \cos(\alpha_i - \alpha_{i+1} + \phi) \tag{2.27}$$

and since $\frac{2J_1}{\cos\phi} \geq 0$ for $\phi \in [0, \pi/2]$, the ground state of the one-dimensional chain is given by the restriction:

$$\alpha_i - \alpha_{i+1} = \phi \tag{2.28}$$

with $\alpha_i$ determined by imposing suitable boundary conditions. Therefore, the classical FM ground state acquires now a canted ('frustrated') spin structure ($\alpha_i - \alpha_{i+1} \neq 0$), irrespective of the value of $J_2$.

## 2.4 Elementary excitations of coupled spin systems

As already pointed out in Paragraph 2.1.1, it is a great leap to postulate a Heisenberg-like hamiltonian for realistic ferromagnets. Nonetheless, its 'good sense' makes eqn (2.3) to be a model rich in physical insight. In this regard, consider an homogeneous body ruled only by a term like (2.3). In the ground state of such a system all the spins line up towards a given direction. Due to the exchange interaction, if one of them bends away from the alignment axis, the perturbation is carried over the entire texture. This is just one pictorial example of what a *spin wave* is, whose idea was initially conceived by Bloch [1] as the lowest-lying energy state of unbounded ferromagnetic media. Actually, spin waves are propagating disturbances in the ordering of magnetic materials; their quantized version, namely *magnons*, are quasi-particles which

behave like bosons (see below), have a discrete energy spectrum and a well defined momentum. By acting the same way as phonons do in solids, they play in magnets the role of collective excitations.

Albeit plenty of theories were developed to describe spin wave quanta [51, 52], their very essential features can be caught starting from an elementary reasoning involving a one-dimensional chain of $N$ coupled spins ($S = 1/2$). In this case, the *Pauli spin exchange operator* $P_{i,j}$, which basically interchanges the spin of the $i$-th site with the one on the $j$-th site, can be used to express the Heseinberg hamiltonian (2.3) as follows [53]:

$$H = -2\sum_{i>j} J_{ij}(\mathbf{S}_i \cdot \mathbf{S}_j) \quad \Longrightarrow \quad H = -\frac{J}{2}\sum_n (2P_{n,n+1} - 1) \tag{2.29}$$

In eqn (2.29) it is assumed that only nearest neighbour interactions are important, and the exchange integral $J_{ij} \doteq J > 0$ is unique for all of them. The ground state $|G\rangle$ is thus achieved when, throughout the row, the spins point in the same direction. In this configuration the operator $P_{i,j}$ has not effect on the state, and the energy of $|G\rangle$ is simply:

$$\langle G| H |G\rangle = -\frac{J}{2}N \tag{2.30}$$

Subtracting the constant offset (2.30) from (2.29), a zero energy is assigned to $|G\rangle$, so to made it as a reference. The hamiltonian $H$ then becomes:

$$H = -J\sum_n (P_{n,n+1} - 1) \tag{2.31}$$

Suppose now to turn upside down the $m$-th spin to create the lowest possible excited state, generally labelled with $|m\rangle$. The necessary excitation, termed magnon, *must* behave like a boson, since the total spin variation with respect to $|G\rangle$ amounts to $1/2 - (-1/2) = 1$. The overall wave function $|\psi\rangle$ can be expressed as the sum of all possible states $|m\rangle$ with a flipped spin:

$$|\psi\rangle = \sum_m |m\rangle \langle m|\psi\rangle \tag{2.32}$$

where the braket $\langle m|\psi\rangle$ gives the probability amplitude to find the system in the state $|m\rangle$. Hence, by inserting (2.32) in the Schrödinger equation $H|\psi\rangle = E|\psi\rangle$ and by premultiplying it by $\langle n|$, one obtains:

$$-J\sum_i\sum_m \langle n|\left(P_{i,i+1}-1\right)|m\rangle\langle m|\psi\rangle = E\langle n|\psi\rangle \tag{2.33}$$

At this stage, consider the action of $P_{i,i+1}$ on $|m\rangle$. If neither $i$ nor $i+1$ are equal to $m$, two parallel spins switch places leaving the state unchanged, and so $\left(P_{i,i+1}-1\right)|m\rangle = P_{i,i+1}|m\rangle - |m\rangle = |m\rangle - |m\rangle \equiv 0$. Instead, if $i = m$, then the flipped spin at location $m$ is moved to location $m+1$, and thus:

$$\left(P_{m,m+1}-1\right)|m\rangle = |m+1\rangle - |m\rangle \tag{2.34}$$

Similarly, if $i+1 = m$:

$$\left(P_{m,m+1}-1\right)|m\rangle = |m-1\rangle - |m\rangle \tag{2.35}$$

Replacing relations (2.34) and (2.35) in eqn (2.33), with the additional requirement of normalized states, i.e. $\langle m|n\rangle = \delta_{m,n}$, one eventually gets [53]:

$$-J(\langle n-1|\psi\rangle + \langle n+1|\psi\rangle - 2\langle n|\psi\rangle) = E\langle n|\psi\rangle \tag{2.36}$$

If the spins are displaced by a distance $a$, and the $n$-th site lies at $x_n$, defining

$$\langle n|\psi\rangle \doteq C(x_n)$$
$$\langle n\pm 1|\psi\rangle \doteq C(x_n \pm a)$$

eqn (2.36) reads as the following difference equation,

$$-\frac{E}{J}C(x_n) = C(x_n-a) + C(x_n+a) - 2C(x_n) \tag{2.37}$$

with a solution of the form:

$$C(x_n) = e^{ikx_n} \tag{2.38}$$

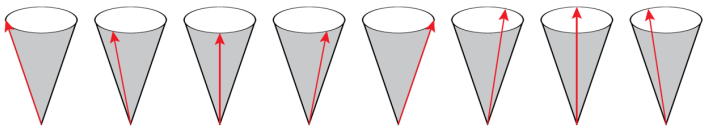

**Figure 2.6:** Schematic of a propagating spin wave along a line of spins. Within the spin exchange operator method, the disturbance along the chain can be viewed as the passing of a region where the likelihood to flip a spin is high. Its travelling nature arises from the probability that near spins exchange their position, thus effectively moving the location of the overturned spin.

where $k$ is the perturbation wavevector. Finally, substituting (2.38) in eqn (2.37) and simplifying yields to the dispersion relation for the chain:

$$E = 2J(1 - \cos ka) \quad \underset{E=\hbar\omega}{\Longrightarrow} \quad \omega = \frac{2J}{\hbar}(1 - \cos ka) \tag{2.39}$$

which reduces to $\omega \propto k^2$ [1] in the long wavelength regime ($ka \ll 1$).
Recalling eqn (2.32), the attained normalized eigenstates $|\psi\rangle$ of the perturbed system are linear combinations of states $|m\rangle$, each weighted by a plane-wave-like term (2.38):

$$|\psi\rangle = \frac{1}{\sqrt{N}} \sum_m e^{ikx_m} |m\rangle \tag{2.40}$$

Individually, none of the $|m\rangle$ diagonalize the equivalent hamiltonians of (2.29), and the *probability*, $|\langle m|\psi\rangle|^2$, that the flipped spin is located on $x_m$ is the same for each position. Thence, $|\psi\rangle$ can be interpreted as a flipped spin 'smeared out' across all the one-dimensional crystal. Indeed, referring to a less rigorous but more intuitive semiclassical approach [19], the discussed perturbation, i.e. a spin-wave, is efficiently ascribed as an excitation of the row of spins where the precession phase changes from site-to-site (see Fig 2.6).

### 2.4.1 Spin waves in thin films: an overview

Dealing with three-dimensional materials, a macroscopic theory, based on the magnetization dynamics (see eqn(2.18) in Paragraph 2.1.5), needs to replace the aforementioned vision of individual spins. Especially, restricting the focus

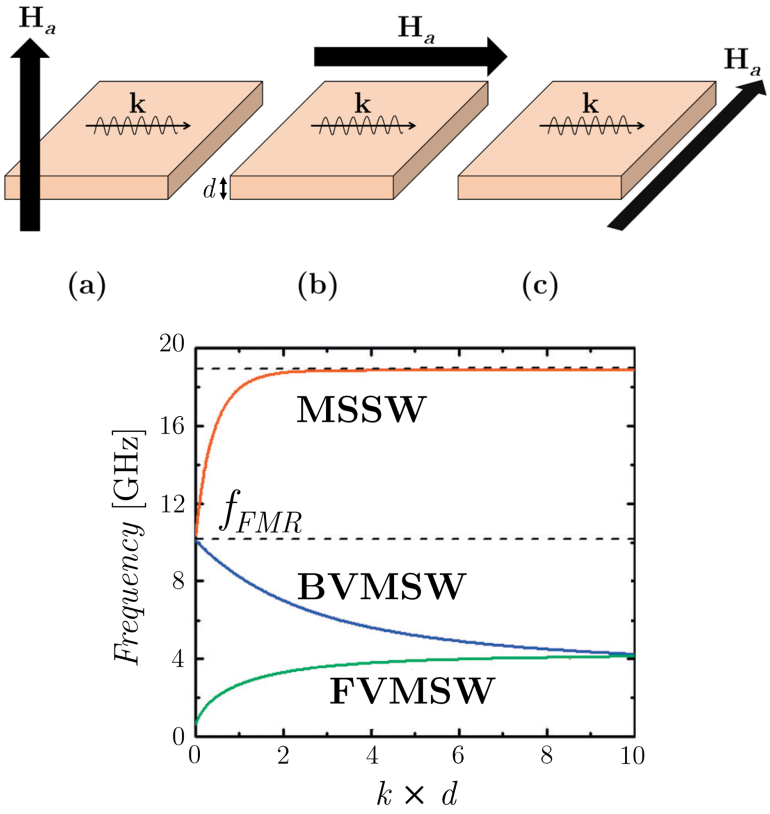


**Figure 2.7:** Geometrical configurations for propagation of **(a)** Forward Volume Magnetostatic Spin Waves (FVMSW), **(b)** Backward Volume Magnetostatic Spin Waves (BVMSW) and **(c)** Magnetostatic Surface Spin Waves (MSSW). The panel below reports the calculated dispersions of the three different magnetostatic spin waves modes for a thin $Ni_{80}Fe_{20}$ slab with $4\pi M_S$ = 10.8 kOe. The applied field $H_a$ amounts to 1 kOe for MSSW and BVMSW, while $H_a$ = 11 kOe for FVMSW. The bottom inset is adapted from [58].

on a thin ferromagnetic film (thickness $d$), three primary types of spin waves modes can propagate, known as Forward Volume Magnetostatic Spin Waves (FVMSW), Backward Volume Magnetostatic Spin Waves (BVMSW) and Magnetostatic Surface Spin Waves (MSSW) [54, 55]. FVMSW are so termed because of the concordant sign of phase ($v_p \doteq \omega/k$) and group ($v_g \doteq \partial\omega/\partial k$) velocity; contrarily, in BVMSW, the dispersion relation $\omega$ *vs.* $|\,\mathbf{k}\,|$ is a monotonic decreasing function (see eqn (2.42)), and thus $v_g$ is opposite to $v_p$. Nevertheless, they both are distributed throughout the volume of the medium, in contrast to MSSW, which are confined on its surface. The specific orien-

tation of the applied magnetic field $\mathbf{H}_a$, sum of a static (modulus $H_a$) and a (small) time-varying component, with respect to the spin wave propagation vector $\mathbf{k}$ determines which one of these modes is allowed (see Fig. 2.7). In what follows $\mathbf{H}_a$ stands for the static component of the field.

As sketched in Fig. 2.7, FVMSW are enabled when $\mathbf{H}_a$ is imposed perpendicularly both to the film and to the spin wave vector $\mathbf{k}$. In such a geometry, as long as $\mathbf{k}$ is in plane, no matter its actual direction, it is automatically perpendicular to $\mathbf{H}_a$, and therefore FVMSW result (waves propagation only depends on the magnitude of $\mathbf{k}$, i.e. it is *isotropic*). An approximate dispersion relation for the lowest-order FVMSW mode ($n = 0$) can be obtained through a perturbation theory on the magnetic equation of motion, and reads as [53]

$$\omega = \sqrt{\omega_0 \left[ \omega_0 + \omega_m \left( 1 - \frac{1 - e^{kd}}{kd} \right) \right]} \tag{2.41}$$

where $\omega_0 \doteq \gamma \mu_0 H_a$ and $\omega_m \doteq \gamma \mu_0 M_S$ ($\gamma$ is the gyromagnetic ratio).
For $k \to 0$, eqn (2.41) starts at $\omega_0$, while increasing the value of $k$, the function approaches ($k \to \infty$) the limit of $\omega_{FMR} \equiv \sqrt{\omega_0(\omega_0 + \omega_m)}$, which is the Ferromagnetic Resonance (FMR) frequency [56] (typically in the GHz range for ferromagnets).

Contrarily to the previous case, when the bias is applied in plane, the spin wave propagation characteristics are affected by the angle between $\mathbf{H}_a$ and $\mathbf{k}$. If $\mathbf{k} \parallel \mathbf{H}_a$ one gets BVMSW, whose lowest-order dispersion relation ($n = 1$) is the opposite of the one for FVMSW [53]:

$$\omega = \sqrt{\omega_0 \left[ \omega_0 + \omega_m \left( \frac{1 - e^{kd}}{kd} \right) \right]} \tag{2.42}$$

In fact, eqn (2.42) starts at $\omega_{FMR}$ and reaches $\omega_0$ for $k \to \infty$. This behaviour engenders a negative slope of the dispersion relation, which causes counterpropagating phase and group velocities.

Finally, MSSW arise when considering a propagation perpendicular to an in-plane magnetized film with $\mathbf{H}_a$ applied as in Fig. 2.7. The dispersion

relation for MSSW is given by [53]:

$$\omega = \sqrt{\omega_0 \left(\omega_0 + \omega_m\right) + \frac{\omega_m^2}{4}\left[1 - e^{-2kd}\right]} \tag{2.43}$$

Differently from FVMSW and BVMSW, now there is only a single mode, which shifts from one side of the slab to the other when the direction of propagation is reversed (this phenomenon is called *non-reciprocity*; see Fig. 2.8). Moreover, the spin wave amplitude exponentially decays moving away from the surfaces.

A comprehensive summary of the above results can be found in [53, 57].

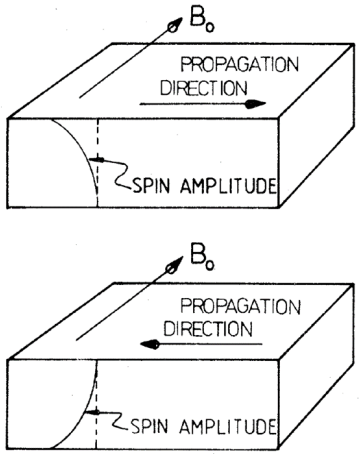


**Figure 2.8:** Schematic of the spatial localization of MSSW in a thin ferromagnetic film as a function of the propagation direction. The image is taken from [59].

# Chapter 3

# Experimental methods

## Overview

Within the state-of-the-art equipped cleanroom in PoliFAB, it was possible to realize and to characterize devices whose feature sizes fall in the submicrometer range. Historically, microfabrication technologies arose from the microelectronics industry as an attempt to address the issue concerning the integration and miniaturization of electronic components on silicon wafer. However, in recent years, microfabrication techniques have been employed for several different applications, ranging from microelectromechanical systems (MEMS) to precision engineering, thus becoming a milestone of a rich variety of industrial activities. The tremendous progresses achieved in this field would not have been possible without the parallel improvement of characterization methods in material science, where new developments are constantly emerging. Especially, the 20th century has been deeply signed with the introduction of the electron microscopes and by the advent of scanning probe microscopy, that paved the way for new landscapes in surface physics.

Purpose of this chapter is to introduce the most relevant approaches to micro- and nanofabrication adopted in this thesis work, and the working principles behind the techniques used to characterize both the samples morphology and their magnetic properties.

## 3.1 Growth and samples preparation

The samples reported in Chapters 4 and 5 underwent various fabrication and characterization steps. Among these, the growth of materials stacks and the nanopatterning were the most fundamental ones. However, since the followed procedure was tailored to the specific heterostructures, the techniques explained in the next paragraphs were not always carried out in the same order they are here exposed and, generally speaking, they might have been performed more than once.

### 3.1.1 Magnetron sputtering

Magnetron sputtering is a physical vapour deposition (PVD) coating technology in which the erosive action of a self-sustained plasma is used to grow high quality thin films. By means of several tunable parameters, it allows an accurate control on the thickness and composition of the deposited material. Moreover, an important advantage compared to other methods consists in the broad variety of substances that can be exploited, which also includes those with very high melting points (e.g. refractory metals) and alloys, whose evaporation is otherwise challenging or even impossible. Fig. 3.1 shows the basic mechanism of magnetron sputtering process.

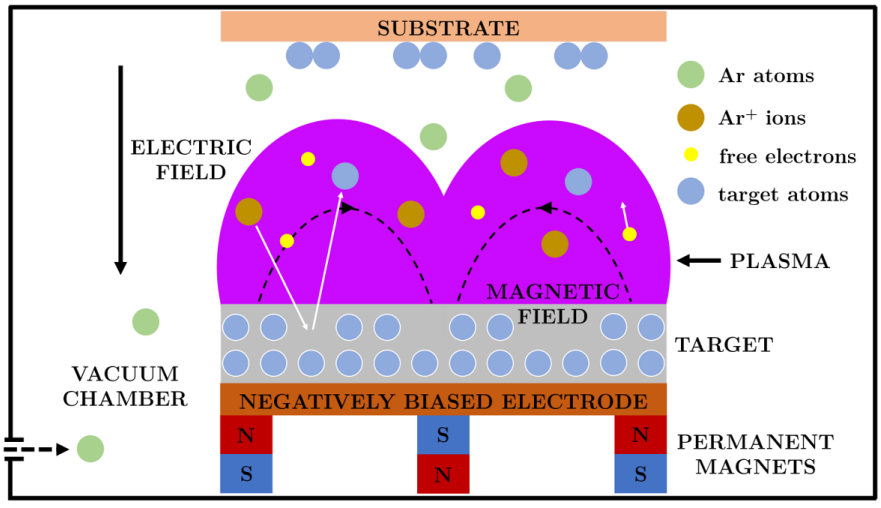


**Figure 3.1:** Simplified schematic of the magnetron sputtering process.

As sketched in Fig. 3.1, inside a vacuum chamber a plasma of an inert gas (Argon in our case) is firstly ignited by accurately varying the potential drop between the substrate and the target; indeed, the pumped gas start conducting when a threshold value, known as *breakdown voltage*, is reached. In this circumstance the free electrons inside the chamber gain enough energy to ionize neutral Ar atoms upon inelastic scattering occurrences. Because of the electric field seen by electrons and $Ar^+$ ions, the former move towards the substrate and the latter are accelerated against the source material, thus establishing a net current. Travelling to the respective electrodes, the charged particles and the injected Ar atoms undergo multiple striking events. Therefore, by properly raising the applied bias it is possible to attain a cascade of ionizing collisions in which the ensemble of charged particles self-sustains.

Hitting the target surface, the $Ar^+$ ions release energy via momentum transfer, hence knock off (*sputter*) material in the form of neutral atoms, clusters of atoms or molecules. These last, crossing the vacuum chamber, reach the substrate where they may adhere and contribute to the thickness of the growing film. To achieve better results it is possible to confine the plasma nearby the target by means of the action of an extra magnetic field. The configuration illustrated in Fig. 3.1 is called *planar magnetron sputtering* and employs an array of permanent magnets to trap the free electrons immediately above the source material, providing some major advantages. First of all, the circular paths covered by the negative charges due to the forces acting on them enhance the ionization probability for neutral Ar atoms, allowing a lower partial pressure of the gas to ignite and maintain the plasma. Besides, the plasma density is increased of several orders of magnitude; as a consequence, the sublimation rate of the target material is speeded up and so does the deposition one. Lastly, the free electrons, repelled by the beneath cathode, are prevented from bombarding the substrate and the chamber walls eroding or overheating them.

Other key specs of sputtered films are good adhesion and 'step coverage', that is the ability to evenly coat microscopic features. Indeed, because the process takes place at relatively high pressure, the source material does not propagate through the space in a rectilinear fashion. Since some gaseous

diffusional transport of the target atoms occurs, they do not follow ballistic trajectories and this results in a higher degree of substrate coverage. Also of great interest is the film thickness uniformity which may be obtained from a given source. It basically depends on material being sputtered, working pressure, substrate geometry and its motion, target design and its relative distance from the substrate (typically 30–100 mm).

The simplest magnetron application concerns the growing of metallic substances and alloys by DC sputtering in which the target directly conducts electricity. The same configuration does not work in case of insulating materials due to charging effects. This issue can be overcame by means of a high frequency (RF) alternating excitation that capacitively couples to the target such that a DC sheath potential develops on its surface [60]. Because a DC voltage is now present, ion bombardment still occurs and a current is re-established. Thus, it becomes even possible to sputter this class of materials without charging troubles. However, regardless the operation mode adopted, dealing with ferromagnetic compounds demands some extra caution. Indeed, their stray field can modify the designed electrons-confinement magnetic field in front of the target. In this case either very thin targets or stronger permanent magnets beneath them must be employed. Furthermore, before the effective deposition of any materials, presputtering or 'conditioning' is always required to achieve high-purity films. In this way oxides and surface contaminants are removed and then adsorb onto shutters placed in between the substrate and the source material.

Within the present work the AJA ATC Orion 8 Sputtering System shown in Fig. 3.2 has been exploited. It is equipped with ten 2"/1" DC or RF targets arranged in a confocal *sputtering-up* configuration (i.e. the sputtered atoms travel from the bottom to the top), including $SiO_2$, $Co_{25}Fe_{75}$, MgO, Ta, $Ir_{22}Mn_{78}$, $Co_{40}Fe_{40}B_{20}$, Ru, Ti, Au, Pt. The sample holder, eventually in-plane magnetized, is bounded to the upper cap of the main chamber **(A)** and can be moved in the vertical direction for optimizing the substrate-target distance. During the deposition it is kept in rotation and it can be brought up to 800 °C. In fact, heat increases the surface diffusion coefficient

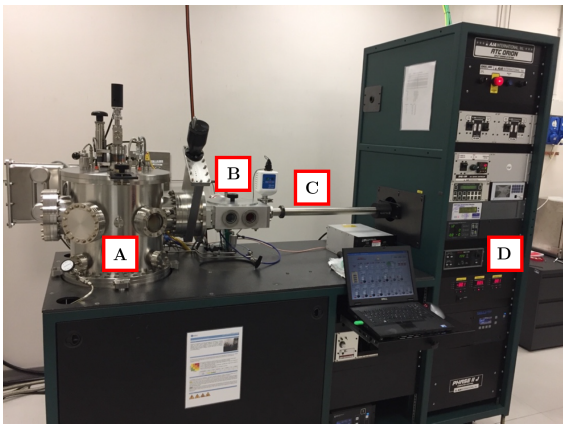


**Figure 3.2:** AJA ATC Orion 8 Sputtering System. **(A)** is the deposition chamber, **(B)** is the load-lock chamber, **(C)** is the transfer arm and **(D)** are the target power supplies.

enabling reorganisation of the growing film and further improvements in its uniformity. To maintain **(A)** in high vacuum (HV) regime ($10^{-8}$–$10^{-9}$ Torr), and thus decoupling it from the outside, a turbo-pumped load-lock chamber **(B)** is used as a fast entry chamber. For this purpose, the substrates un-/loading from **(A)** to **(B)** and vice versa is performed by a mobile transfer arm **(C)** which must be perfectly aligned with the below working plane. The entire sputtering process is driven by power supplies **(D)** and it is remotely controlled by the Phase II LabVIEW software which can be operated in both manual and automatic mode. While in the former all the relevant parameters (targets power, Ar pressure etc.) are set real-time during the deposition, the latter consists in running arbitrary recipes created beforehand. Due to the high-level reproducibility it guarantees, this second option is more advisable when the materials stack is made up of several layers and different targets are to be controlled contemporarily.

### 3.1.2 Optical and electron-beam lithography

The word lithography comes from the Greek *lithos*, meaning stones, and *graphia*, meaning to write. It can be literally translated as 'writing on stones' referring to the process invented in 1796 by Aloys Senefelder. What he found out was that accurately inked and chemically treated Bravarian limestones

could retain and later transfer carved images onto paper.

Although it was originally born as a cheap method of publishing theatrical works [61], nowadays lithography is employed within a broad range of applications and it is one of the key procedures in semiconductor industry [62]. It basically concerns the projection of a bidimensional geometry onto the sample surface thanks to a suitable (often virtual) template, the *mask*, and a thin layer of a polymer, called *resist*, priorly cast over the whole substrate. Actually, by interacting with proper excitations (especially electrons and light) the resist solubility in specific solvents varies, thus making it possible to create a contrast between exposed and unexposed regions corresponding to the mask's voids and solids, respectively. Indeed, once the sample is rinsed in such solvents (*resist development*), the soluble zones are wiped away upon chemical reactions, leaving the mask's image onto the surface. Subsequently, the resulting pattern can be effectively transferred to the substrate by either etching (*subtractive* process) or coating (*additive* process) the resist-free areas.

Depending on the type of radiation used to expose the resist, the technique is named either electron-beam or optical lithography, albeit the steps to follow are substantially the same and include:

(i) **Substrate preparation.** The sample is adequately clean to improve the adhesion of the resist material and increase the effectiveness of the whole process. Substrate contaminants include dust and other particulates and can be either organic or inorganic. The procedure adopted in this work consists of a ultrasonic (US) bath in acetone followed by an isopropylic alcohol (IPA) rinsing to avoid the formation of stains on the surface. If present, inorganic films, such as native oxides, can be removed by chemical or plasma stripping, while a high-temperature process, called *dehydration bake*, is eventually needed for adsorbed drops of water.

(ii) **Deposition of the resist.** A thin, uniform layer of resist at a specific, well-controlled thickness is deposited on the previously cleaned sample surface via *spin coating*. The resist, rendered into a liquid form by

dissolving it in a solvent, is firstly poured onto the substrate, which is held in place by an opportune vacuum chuck, and then spun on. A speed of rotation greater than 4000 rpm is usually chosen to establish a uniform thickness (of the order of 1–2 µm for photoresists and few hundreds of nm for e-beam resists). Besides the velocity, there is plenty of parameters to be paid attention to (such as the spinning time and acceleration, the dispensed resist volume, the substrate material and topography etc.) which directly affect the layer thickness and homogeneity. Yet, after the spin coating, the resulting resist still contains a surplus of solvent by weight. Hence, a thermal *soft baking* is performed to dry it by removing most of this excess, thus stabilizing the film and enhancing its adhesion to the substrate. To better understand what follows, it is important to stress that resists are classed in two different types: *positive* when exposure makes them soluble in specific solutions, and *negative* when they become insoluble instead. Since in the present work only positive resists were used, belonging to the poly(methyl methacrylate) (PMMA) family, hereinafter just the related exemplifying lithographic process will be described (see Fig. 3.3).

(iii) **Exposure.** When the resist polymer interacts either with UV light (photoresists) or with a high energy electron beam (e-beam resists), its chemical properties change. The image transfer through the exposure can be realized by means of a physical mask, laid on top of the sample, or opportunely steering a laser or an electron beam. The devices described in Chapters 4 and 5 were fabricated designing the proper masks in advance, drawing them in AutoCAD. Of course, depending on the sources, different resolutions are allowed. While for UV optical lithography performed with a mask aligner or a maskless aligner the minimum feature size is limited by light diffraction to about 1–0.7 µm [63] , with electrons it has been shown [64] that ultimate resolution as small as 3 to 5 nm is feasible under certain circumstances. Indeed, several factors can be modified to find the best working scheme, including

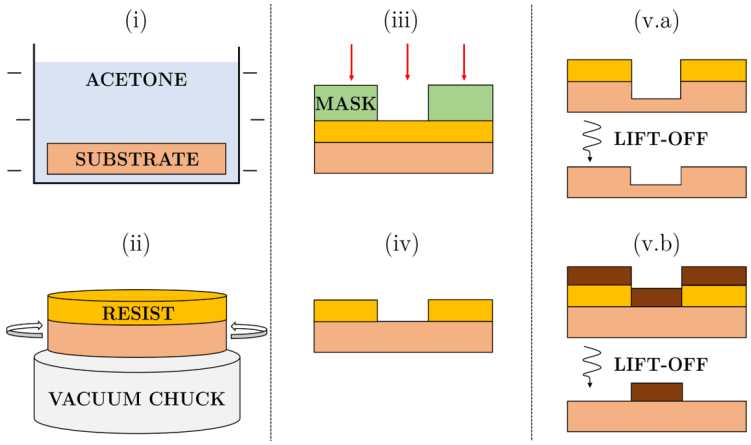


**Figure 3.3:** Main steps in direct lithographic process. (i) The substrate is first cleaned through a ultrasonic bath in acetone. (ii) Then, the resist is deposited via spin coating and a soft baking follows. (iii) A (virtual) mask is put on top of the sample and the exposure takes place. (iv) Lastly the soluble resist is wiped away using a proper solvent. (v.a) and (v.b) are schematic illustrations of a subtractive and an additive transfer approach respectively. The final stages are both achieved thanks to the lift-off procedure.

the resist thickness and composition, the *dose*, defined as the nominal energy/charge deposited per unit surface, and the radiation focusing.

(iv) **Resist development.** Once exposed, the resist must be developed. Development is one of the most critical steps since the nature of resist-developer interactions strongly influences the shape of the resist profile [65]. To wipe away the soluble resist, the sample is immersed in a suitable solvent for a given period. Customarily, the optimal developing time $\Delta t_d$ follows the identification of the right exposure conditions, which are harder to establish and, if wrong, easily lead to poor lithographic outcomes. Anyhow, even determining $\Delta t_d$ is an issue of paramount importance since two major drawbacks can occur, namely *under-* and *overdevelopment*. In fact, in an underdeveloped sample, the resist leftovers could compromise the subsequent microfabrication stages. In the other case, the patterns transferred on the substrate could appear blurry, or could have wrong dimensions, because some unexposed resist was actually removed.

(v) **Pattern transfer.** Lastly, the resist pattern must be transferred to the substrate below. There exist two basic options:

a) Subtractive transfer (etching)

b) Additive transfer (selective deposition)

Etching is the most common approach and it will be described in depth in Paragraph 3.1.4. It mostly consists in digging the sample either using wet chemicals or in a dry environment. On the contrary, additive processes take advantage of the lithographic pattern to open areas where a new layer has to be grown. After the sample is coated, by stripping of the resist a 'negative' version of the mask is produced. Indeed the combined action of a solvent (called *remover*), US and heating cause the detachment of the resist and everything on top (*lift-off*).

All the phases involved in a direct lithographic process, such as those described in the text, are summarized in Fig. 3.3.

To prepare the samples reported in Chapter 4, optical lithography was required to pattern stripline inductive antennas atop $Si_3N_4$ membranes. Lithography was performed through a Heidelberg Tabletop Maskless Aligner 100 (MLA), an instrument designed to achieve structures down to 1 µm without the need for a physical photomask. Therefore, the desired geometries were drawn in advance by means of standard softwares, and a scanning LED light source ($\lambda$ = 365 nm) later transferred them on the photoresist. Instead, the realization of the specimens depicted in Chapter 5, namely magnonic crystals constituted by stripes of diverse materials ~ 200 nm wide, demanded electron-beam lithography. Conceptually, nothing changes in the procedure except that electrons replace photons and a different resist needs to be adopted (PMMA instead of AZ 5214E). To the purpose, it was exploited a LEO 1525 Field Emission-Scanning Electron Microscope (FE-SEM) equipped with a Raith Elphy Plus pattern generator. The accelerating voltage ranges from 0.5 to 20 kV and a field emission gun allows to produce a small beam with high current density, with a ultimate writing resolution down to 20 nm.

### 3.1.3 tam-SPL

Thermally assisted magnetic – Scanning Probe Lithography (tam-SPL) is a novel technique allowing to create reconfigurable magnetic nanopatterns in continuous exchange biased films. It belongs to the family of scanning probe-based lithographic methods [66], born in the late 1980s aiming to overcome the resolution limits of conventional lithography. Even though SPL takes advantage of several approaches to pattern materials, they have all a common thread; indeed, local changes on a surface are always achieved by means of a sharp scanning probe. It can be either in contact or not and its relative position can be adjusted through a variety of feedback mechanisms, such as quantum tunnelling or suitably tuning its interaction force with the sample. Especially, most of the current SPL techniques, as well as tam-SPL, rely on the use of an atomic force microscope (AFM), whose working principle is explained in the Paragraph 3.2.2. The main benefit of SPL over optical and electron-beam lithography consists in its process, which is accomplished in a single step, whereas the others constitute of various stages to follow (see Paragraph 3.1.2). Moreover, the conceptual simplicity of the approach, which allows for parallelization schemes, the feasibility of adopting common laboratory instrumentations, as atomic force or scanning tunnelling microscopes, and the orthogonality between the writing and the reading procedures, make SPL an appealing approach to nanolithography, raising a major interest in this research field.

Recently [67], the already broad class of SPL methods has been enriched by the introduction of tam-SPL, widening their possible applications to magnetic materials. Indeed, tam-SPL has found relevance in magnonics, by nanopatterning spin-textures, such as domain walls, for the manipulation of spin-waves [68, 14]. The technique basically implements a confined field cooling at the nanoscale, which locally rewrites the magnetic configuration of the sample without modifying the chemistry nor the topography. Tam-SPL uses a customized tip of an AFM, with two n-doped Si conductive arms and an intrinsic Si resistive heater. Hence, by applying a voltage, a current is forced to flow through the tip, warming up via Joule effect the resistive part.

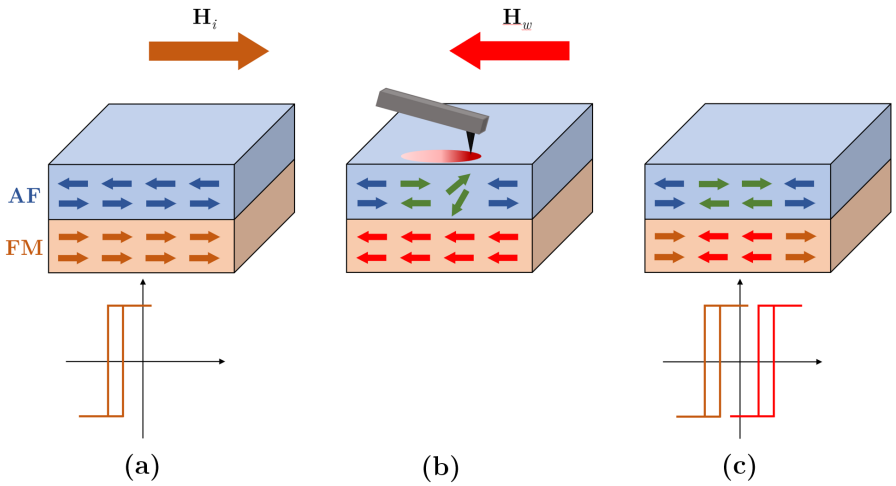


**Figure 3.4:** Working principle of tam-SPL. **(a)** Firstly, the sample undergoes a magnetic thermal annealing. The resulting magnetization of the ferromagnetic layer (light brown) is pinned along the direction of $\mathbf{H}_i$ by the exchange-bias interaction with the antiferromagnet. **(b)** Scanning the hot tip over the surface, a local field cooling is achieved (green arrows) through the applied field $\mathbf{H}_w$. **(c)** Upon removing $\mathbf{H}_w$, the restoring interfacial coupling locks the system in the new configuration, where the patterned areas present a different magnetic landscape.

Scanning in contact mode an exchange-biased ferromagnetic layer, this is heated only in the regions crossed by the hot probe. There, a unidirectional magnetic anisotropy can be permanently set combining the action of an external magnetic field $\mathbf{H}_w$ and the coupling with the adjacent antiferromagnet (AF), as shown in Fig. 3.4. A unidirectional anisotropy axis is firstly fixed in the FM **(a)** with a field cooling of the entire structure in a uniform magnetic field $\mathbf{H}_i$ (see Paragraph 2.2.1). During the pattern, the hot tip of the AFM is scanned over the surface of the film. Beneath the path of the tip, the temperature of the substrate temporarily exceeds the blocking temperature $T_B$, defined as the one at which the exchange bias disappears. Therefore, due to thermal fluctuations, the magnetic coupling exerted at the AF-FM interface is relaxed unlocking the interfacial FM spins, which are able to reorient along the direction of the writing field $\mathbf{H}_w$ **(b)**. During field cooling, i.e. when the tip moves away, the FM spins act as a template for the AF spins and a new exchange bias in a different direction is stabilized. If the last is large enough, the direction of the magnetization of the FM at remanence

corresponds to the direction of $\mathbf{H}_w$. Elsewhere, though $\mathbf{H}_w$ is possibly sufficiently high to cant the FM spins, the exchange bias is still present, and upon removal of the field, the spins of the FM realigned according to the coupling with the unperturbed AF interfacial spins. In this way, tam-SPL redefines the unidirectional anisotropy of the FM only under the scanned area, without perturbing 'magnetism' in the nearby zones **(c)**. Besides, because of the AF-FM coupling nature, the patterned features result to be long-lasting and field-resilient, namely they cannot be erased or permanently modified by the use of a magnetic field only.

The magnetic geometries characterizing the samples of Chapter 4 have made possible thanks to tam-SPL technique; it was executed by Dr. Edoardo Albisetti via a NanoFrazor Explore (SwissLitho AG) customized experimental setup, at the CUNY-Advanced Science Research Center, New York.

### 3.1.4 Ion beam etching

As explained in Paragraph 3.1.2, two complementary ways to transfer the mask image from the resist to the substrate exist, based either on the removal or the addition of material. This paragraph deals with a subtractive dry approach, i.e. a process in which a solid substrate is properly carved without the employment of liquid-phase ('wet') chemicals. Indeed, ion beam etching (or milling) is a physical dry technique used to etch a masked pattern sample by directing on it a beam of charged particles in a HV chamber. Similarly to what happens in plasma assisted physical vapour deposition methods, the sample material is removed by energy transfer between positive ions and its surface atoms. Fig. 3.5 illustrates a simplified schematic of the utilized Sputtering and Ion Beam Etching Kenosistec VS80 experimental apparatus.

A potential difference (*discharge voltage*) accelerates thermionic emitted electrons from a heated filament ($I_{fil} \simeq 2$mA, $V_{fil} \simeq 40$V) through the atmosphere of an injected inert Argon gas (working pressure of about $10^{-4}$ mbar). Upon hitting neutral Ar atoms, $Ar^+$ ions and additional free electrons are generated, thus igniting a plasma; in turn, while the former are driven by a

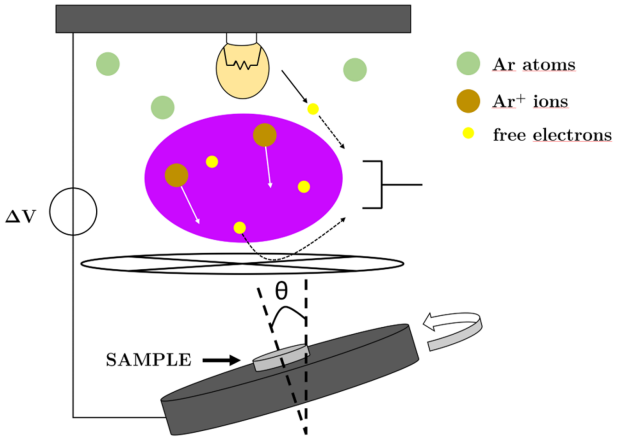


**Figure 3.5:** Ion beam etching technique. A plasma is ignited by energetic electrons, expelled from a heated filament and drew by the positive cross shaped electrode, hitting neutral Argon atoms. The negatively biased grid rejects the electrons and accelerates the positive $Ar^+$ ions towards the sample. Impinging on it, the material is removed by energy transfer between the accelerated $Ar^+$ ions and the sample surface, whose resulting quality is strongly affected by the tilt angle $\theta$.

negatively biased grid toward the sample ($V_{acc} \simeq 200$V, $I_{beam} \simeq 50$mA), the latter contribute to maintain the plasma on. By virtue of the decoupled electrodes governing the plasma and the $Ar^+$ ions, it is possible to independently control both their flux (varying the discharge voltage) and their kinetic energy (acting on $V_{acc}$). To ensure an isotropic etching on the whole patterned area, the sample-holder is kept in rotation throughout the process, and a further electrode, the *plasma bridge neutralizer*, prevents the specimen from charging effects (only neutral Ar atoms reach the surface). Moreover, a fundamental role within the entire procedure is played by the tilt angle $\theta$, which needs to be suitably adjusted to avoid re-deposition of sputtered material.

Table 3.1 lists the parameters adopted to define the structures characterizing the magnonic crystals discussed in Chapter 5. In all cases the Ar gas flow was set to 6 sccm (Standard Cubic Centimetres per Minute) and the stage was tilted by 30 degrees. The reported rates were evaluated by growing calibration samples and by measuring, with an atomic force microscope, the height of etched test features in a given reference etching time.

| **Material** | **Base pressure** | **Etching rate** |
|---|---|---|
| - | [mbar] | [nm/min] |
| $SiO_2$ | $4.2 \cdot 10^{-4}$ | 3.00 |
| Ru | $3.5 \cdot 10^{-4}$ | 2.57 |
| Pt | $3.5 \cdot 10^{-4}$ | 2.70 |

**Table 3.1:** Etching rates for different materials.

### 3.1.5 Magnetic thermal annealing

Thermal annealing is a common technique employed for intrinsic stress liberation, structural improving in materials, and control of magnetic anisotropies. By raising, maintaining for a while, and then slowly reducing the temperature of a solid, the atoms inside can gain enough kinetic energy to rearrange a bit, thus reaching a new minimum-energy equilibrium state. When it is carried out in the presence of a uniform external magnetic field (usually a few tenths of tesla at least), even the magnetic properties could be affected, and the process is also known as magnetic thermal annealing.

Besides the changes in the atomic structure induced through the heating of the sample, the addition of an extra magnetic field **H** customarily helps to stabilize the already present magnetic anisotropies inside a ferromagnet (FM). In this regard, one of the most relevant effects of magnetic thermal annealing concerns the reorientation of the FM axis of spontaneous magnetization, which ultimately results from the interplay of various anisotropy terms (exchange bias, interlayer exchange coupling, magnetocrystalline anisotropy, etc). When a specific magnetic configuration is sought, **H** is precisely addressed to set the easy axis of the FM or, in the case of a net weak anisotropy, to bend the original magnetization vector towards its direction. In fact, if a FM is brought at high temperatures in the presence of a sufficiently strong **H**, its atoms will not only spatially rearrange. On the contrary, by means of the blended action of the applied field and the thermal fluctuations, even the spin system will be altered by the coupling with **H** and the spin-orbit interaction. If the annealed is slow and lengthened in time, an equilibrium condition will be eventually established, which in turn could lead to the searched modifica-

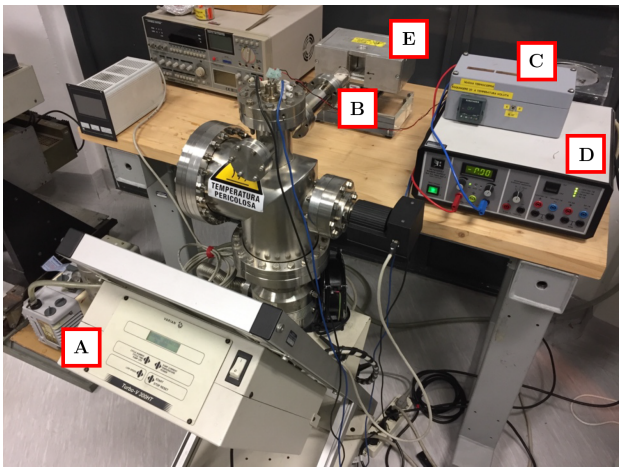


**Figure 3.6:** Field annealing experimental setup. **(A)** is the turbomolecular vacuum pump, **(B)** is the bulb containing the sample, **(C)** is the PID temperature controller, **(D)** is the DC current generator and **(E)** is the permanent magnet.

tion in the overall anisotropy, the latter subsequently 'frozen' by cooling down the FM. Thus, the process as a whole may improve the magnetic properties and make them more robust.

Albeit it belongs to the same theoretical framework, field cooling is a slight variant of the aforementioned procedure, exhibiting two main practical differences. Firstly, heating and cooling take place in a shorter period of time, of the order of few minutes at most; as a result, if the temperatures reached are not too high, no significant structural modifications are induced in the annealed material. Secondly, as suggested by the name, the magnetic field plays a role only in the cooling phase (in fact, one could applied the field solely during this stage). As a consequence, the process primarily affects just the magnetic landscape; for instance, in a proper temperature range, a rapid field cooling can set the exchange bias at a ferromagnet-antiferromagnet interface. Indeed, it is exactly this mechanism which lays the foundations to the technique explained in Paragraph 3.1.3.

Within the present work, the multilayers exploited in Chapter 4 underwent a magnetic thermal annealing to even out and strengthen their magnetic anisotropies. The procedure was performed through the vacuum field annealing experimental setup depicted in Fig. 3.6. A turbomolecular pump

**(A)** ensures a HV regime in the vacuum chamber, from which a transparent bulb protrudes **(B)**. This contains a holder, crossed by a resistive metallic filament. Here the sample is housed upon a ceramic bar, heated via Joule effect. Its actual temperature is constantly monitored by a thermocouple connected to a Proportional-Integral-Derivative (PID) controller **(C)**, which accordingly adjusts the current dispensed by the DC supply **(D)**. Besides, the controller let the user to arbitrarily set the temperature rising rate and the dwell time. Since vacuum prevents convection heat transfers, the system is nearly adiabatic, thus achieving, at the end of the process, the desired slow cooling down phase. In addition, throughout the whole annealing procedure, a uniform 4kOe magnetic field is provided by an external permanent magnet **(E)**, either in-plane or out-of-plane.

## 3.2 Characterization techniques

The characterization phase has covered a fundamental role to track down the relevant aspects of the samples to be optimized, meantime suggesting the improvements to be pursued. Both the specimens morphology and their magnetic properties were in depth investigated, and the next two paragraphs explain the experimental methods employed to carry out these tasks. The section ends with a concise outline regarding the technique used at the Swiss Light Source (SLS) synchrotron facility, hosted in the Paul Scherrer Institut (PSI) in Villigen, to study spin-wave propagation, as reported in Chapter 4.

### 3.2.1 Vibrating sample magnetometry

Vibrating Sample Magnetometer (VSM) is a standard instrument capable to assess the magnetic properties of materials in the form of powders, liquids and solids. As sketched in Fig. 3.7, a magnetization is induced in the specimen by introducing it in a uniform magnetic field, whose magnitude can be tuned within the range of a few Tesla. A mechanical actuator sinusoidally vibrates the sample up and down, thus forcing its magnetic moment to transversally swing in time. Due to the Faraday-Neumann-Lenz law, the resulting mag-

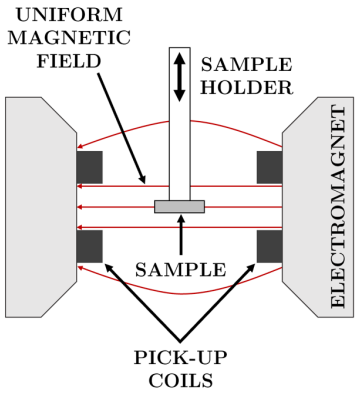


**Figure 3.7:** Schematic of a typical VSM measurement configuration.

netic flux oscillations are converted into an electric signal (i.e. an induced voltage), revealed through a set of stationary pick-up coils arranged around the system. The measured electromotive force is proportional to the magnetization of the sample, as well as to the amplitude and frequency of the vibration. For a given applied field, it is recovered by means of a lock-in amplifier utilizing the same reference as the one triggering the oscillations, and it results as an average of a fixed number of measurements. From this, upon a suitable calibration, the absolute value for the magnetic moment of the specimen is extrapolated. Hence, point-by-point recording of hysteresis loops becomes possible, even as a function of the samples' angular orientation.

Throughout this thesis work a commercial Microsense, LLC. Easy VSM model EZ-9 was employed. It enables to reach magnetic field as high as 2.25 Tesla, and the minimum distinguishable magnetic moment amounts to fractions of $\mu emu$. Moreover, a fully automatized 360° specimens rotation is available for polar characterizations and a side mounted oven/cryostat allows quick heating/cooling in a temperature range from 77 up to 1000 K.

### 3.2.2 Atomic force microscopy

Since its introduction in 1986 [69], the Atomic Force Microscope (AFM) has became one of the most widely used imaging instrument to investigate surfaces at the micro-nanoscale. Thanks to its versatility, it can work both on

hard and soft materials, either in air, in liquid or in vacuum, and it can achieve a resolution down to the atomic level [70]. Besides simply 'measuring', it also allows to manipulate matter and to 'write' on it in different manners [67, 71], as seen for instance in Paragraph 3.1.3. It shares the very general underlying idea of all the other Scanning Probe Microscopes (SPM), coinciding in the raster scan of a probe over the sample surface under the action of an active feedback loop, which determines their mutual distance accordingly to a specific interaction among them. Indeed, when the AFM probe, constituted by a micromachined cantilever with a sharp tip at its end, is brought into proximity of the specimen, a variety of forces arises between the two [72]. By properly mapping these forces, a 2D-topographic image of the sample can be retrieved.

The very heart of the AFM, namely the transducer for the aforementioned 'drivers', is the cantilever, that deflects when interacting with the specimen. It is usually made out of silicon or silicon nitride and can be manufactured in two different shapes, rectangular and V-shaped. Although several methods to detect its bending have been developed so far, the most commonly adopted one is the optical lever. It consists in focusing a laser beam on the back side of the cantilever, coated with a metallic thin layer to enhance its reflectivity, and in detecting the reflected beam through a quartered photodiode. Both the cantilever vertical deflection and lateral torsion signals are collected for subsequent data processing. In fact, after being stored in a computer, they are sent to a controller which suitably regulates and drives a piezoactuator, responsible for the surface raster scanning.

To reconstruct an image, the AFM can operate either at constant tip-sample force or at constant tip-sample distance. In the former, firstly the user decides an arbitrarily setpoint corresponding to a given interaction strength. Since the last depends on the relative distance between the probe and the specimen (see Fig. 3.9), this means establishing the desired probe height during the whole measurement, thus fixing a reference. For each $(x, y)$ in-plane coordinate, the reference is compared to the input, coming from the cantilever, by means of a negative closed-loop circuitry. From their difference an error eventually is generated which both triggers the next scanner

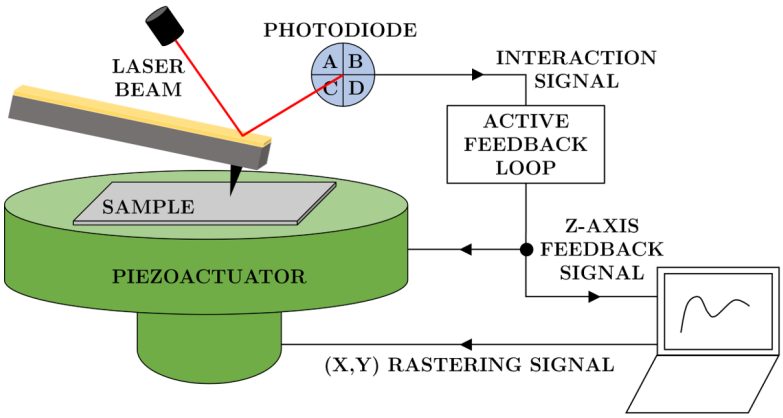


**Figure 3.8:** General scheme of a standard AFM system.

movement, aiming to equalize the measured signal to the setpoint, and contains the sample topographic information (see Fig. 3.8). Alternatively, the second procedure is most suitable dealing with atomically smooth surfaces; in such a case the feedback loop is switched off and the raw cantilever deflection signal is directly employed to build up the topography map. Anyway, regardless of the chosen imaging approach, whereas the lateral attainable resolution always derives from the piezoelectric scanner, the vertical one is strongly affected both by the size of the tip apical radius of curvature and by the dependence of the sample-probe forces in their mutual distance.

To get a very simplified understanding for the behaviour of these interactions, at a first glance they can be overall modelled via the Lennard-Jones potential, as depicted in Fig. 3.9. Based on this assumption, it is so possible to distinguish the two basic AFM operation modes, *tapping* (or dynamic) mode and *contact* (or static) mode. In tapping mode the AFM works with the tip in the attractive regime and the cantilever is excited to vibrate close to its resonance frequency $\nu_0$. By considering it as a driven damped harmonic oscillator, interactions with the sample result in a shift of $\nu_0$, and hence of the actual amplitude of oscillation ($\Delta A$), detectable by means of the deflection. Therefore, the feedback signal is obtained by measuring $\Delta A$ and the height of the tip is accordingly varied to restore the setpoint. The changes in the amplitude and in the phase within the cantilever dynamics both provide

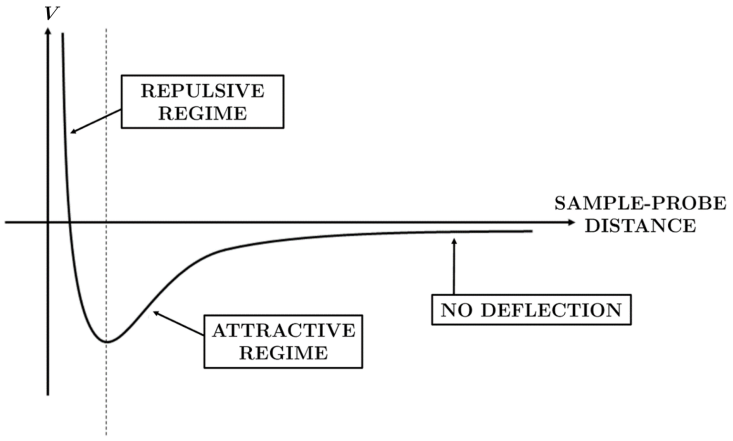


**Figure 3.9:** Potential $V$ established between the AFM probe and the sample surface as a function of their mutual distance. The regime corresponding to a negative slope of $V$ is said repulsive, while where the slope is positive the regime is said attractive. The AFM contact mode works in the first situation, the tapping mode in the second one instead.

different pieces of information; on the one hand from $\Delta A$ the surface topography can be inferred, on the other hand phase images are useful to track material properties variations, such as the composition or the viscosity, or to enhance topographic contrast. In contact mode the tip is brought in the repulsive regime instead, very close to the surface of the sample. Because of the steep profile (see Fig. 3.9), in this circumstance the tip and the cantilever are very sensitive to the morphology of the specimen. Now, the complex interplay between the surface-apex repulsive force, the elastic force due to the cantilever deformation, as well as the mesoscopic attractive cantilever-sample interaction, sets the probe equilibrium position. To maintain it throughout the acquisition stage, the feedback loop straight acts on the deflection signal, kept as close as possible to the reference point.

### Magnetic force microscopy

Magnetic Force Microscopy is an AFM offspring technique for imaging magnetic fields. It is based on using a modified version of a force microscope to measure the magnetic force between the scanned surface and a magnetized tip [73]. Indeed, upon placing a magnetically coated tip close to a magnetic

sample, it interacts with the emanated stray field, which in turn is mapped as a variation of the force exerted on the probe. Thence, scanning the cantilever in a raster-like fashion, an image can be obtained by measuring the force (or force gradient) as a function of position [74].

Actually, the ever-present cross-talk between magnetic and 'topographic' forces demands for extra caution and a two steps procedure, called *lift mode*, has been developed to tackle this issue. The basic idea is to exploit the different spatial decays between magnetic dipole-dipole interactions and all the others, performing a back and forth scan of the sample. First, a standard AFM image is collected, driving the tip as close as possible to the specimen; at such tip-sample distances topography is acquired, being the magnetic signal in comparison negligible. The tip is then lifted at a proper height, say 100 – 200 nm, so that the magnetic forces prevail over the chemical and atomic interactions, and scanned again backwards. To obtain just the specimen magnetic landscape, during the way back this distance is kept constant by means of the previous topographic map, used as a template by the piezoactuator. In this way, ideally, one gets rid of any tip-sample interaction which is not purely magnetic.

Even the tip choice deserves an important remark. Depending on the expected magnetic properties of the examined samples, the tip should be chosen accordingly. Tips characterized by a large coercivity are not affected by the specimen stray field but, at the same time, they can alter the detected magnetic features; similarly, tips with low magnetic moment are less invasive but also less sensitive. Moreover, a tip can be magnetized along its axis or perpendicularly to it to enhance either the out-of-plane or in-plane magnetization sensitivity. As a result, a suitable compromise has always to be found for a given application, since a 'best' choice does not exist in general.

During this thesis, a Keysight 5600LS AFM system was used to perform both topographic and magnetic characterization of the samples.

### 3.2.3 Scanning transmission x-ray microscopy

The magnetization dynamics of the synthetic antiferromagnetic structures described in Chapter 4 was investigated via time-resolved Scanning Transmission X-Ray Microscopy (STXM) at the PolLux end station of the Swiss Light Source [75]. The technique embraces the photons-in/photons-out working principle. To achieve high spatial resolution, it is combined with the focusing, through a Fresnel zone plate, of a soft x-ray beam into a tight spot on the specimen. Images are formed from raster scanning the sample surface while gathering the transmitted intensity for each pixel by means of an avalanche photodiode, placed closely behind the holder. This is possibly surrounded by a permanent magnet generating a magnetic field, either in-plane or out out-of-plane, of hundreds of mT.

The capability of detecting magnetic contrast in the images arises from the X-Ray Magnetic Circular Dichroism (XMCD). When magnetized samples are exposed to circularly polarized light, they differently absorb left and right circularly polarized photons. Particularly, the overall images contrast displays variations in the magnetization component parallel to the photons wave vector. Thus, for normal x-ray beam incidence, regions where the out-of-plane magnetization component attains different values are mapped by distinct greyscale layers. Furthermore, as XMCD is a resonant technique, a monochromator is needed to tune the beam energy to the characteristic absorption edges of the magnetic elements of interest.

By collecting consecutive acquired time-resolved images, a coherent 'movie' of the magnetization dynamics can be retraced. For this purpose, the high temporal resolution required in between consecutive frames is obtained thanks to a pump-probe scheme, exploiting the bunched nature of synchrotron radiation. Indeed, the probing x-ray flashes (70 ps FWHM) take a picture of the specimen magnetic state stroboscopically, and by properly coupling these signals with a pumping one, the time evolution of the magnetization can be recorded. Hence, the exciting magnetic field, generated by injecting a RF current inside lithographically patterned microstrip antenna, is synchronized to the 500 MHz master clock of the synchrotron light source.

# Chapter 4

# Optically-inspired magnonic platform based on synthetic antiferromagnetic structures

## Overview

Spin waves (SW) are promising candidates as information carriers in novel computing devices for data processing. As a matter of fact, among competing technologies, as electronics and photonics, SW offer several advantages. On the one hand, compared to electrons, the propagation of magnons is not associated with the motion of charges, so that ohmic losses are completely avoided. On the other hand, in the frequency range significant for all practical situations, namely from GHz to THz, the (sub-micrometer) SW wavelengths are several orders of magnitude shorter than those of electromagnetic radiation ($\lambda \sim$ cm). The latter and the possibility of non-linear magnetization dynamics [76], *in principle* let both the miniaturization of spin-wave-based architectures and the tailoring of novel analog functionalities be possible. Nonetheless, two are the major challenges to face.

Firstly, a relevant hindrance for the concrete use of SW lies in the capability of manipulating such waves down to the nanoscale. The customary method to steer SW consists in controlling the magnetic properties of the magnonic system by physically patterning it, i.e. by altering its overall mag-

netic anisotropy to confine the propagating modes. The purpose is mainly achieved by conceiving peculiar film geometries in order to exploit shape anisotropy. However, this procedure limits the resolution, it gives rise to non idealities due to the presence of defects in the fabricated specimens, and in most cases it requires the presence of an external magnetic field to stabilize the magnetization direction [77, 78]. Besides, the scheme lacks the flexibility demanded by the novel concept of reconfigurable devices. In this regard, a great step ahead has been made possible with the introduction of tam-SPL, whose working principle (described in Chapter 3) allows for locally designing the anisotropy of the samples [67, 68].

Secondly, the other big deal to run into resides in generating SW with nanometre wavelength. The traditional mechanism exploits lithographed conductive tracks, properly driven with a radio-frequency current. In such a strategy, the underlying idea is to couple the emanating Oersted field with the static magnetization of the ferromagnetic active layer, thus triggering the emission of SW. The main drawback of this scheme is the minimum $\lambda$, which is set by the width of the used inductive antennas [17]. Despite it is possible to scale the dimensions of the latter, for instance by means of electron-beam lithography, the resulting high resistance of the structure does not let anyway efficiently inject the power required to radiate SW, and overheating problems can occur. So far, the issue has been partially solved either by reducing $\lambda$ after the generation process [79], or by following different approaches, such as SW excitation via parametric pumping [80], or by means of localized magnetic nano-oscillators driven by spin torques [81], which however suffer from low efficiency and poor control on SW, or the need of using specific (thin) propagation channels.

Recently, an intriguing alternative chance to overcome both the aforementioned limitations has been arisen thanks to the experimental evidence for the feasibility of employing magnetic domain walls (DWs) as SW waveguides [14, 82]. Especially, in [14] it has been shown that, through the commonly adopted method of inductive antennas, a DWs dynamics can be promoted. Therefore, in principle, the confined magnetization precession inside DWs can in turn be coupled to the spin texture within the domain to excite SW

in the film. As a matter of fact, a similar reasoning has been already utilized in [16], where properly driven magnetic vortex cores, spontaneously appearing in the remanence state of a synthetic antiferromagnet (SAF), are used as SW emitters. In that case, the peculiar properties of the investigated systems result in SW featuring a non-reciprocal dispersion relation [83], and whose nanometre wavelength can be tailored by accordingly tuning the excitation. Nevertheless, since the vortex cores in [16] have been stabilized, once and for all, from the overall magnetic anisotropy, it has not been possible to *deterministically* control them.

The plan of the first part of the present thesis aimed to pattern via tam-SPL in a SAF *arbitrarily* shaped DWs, to exactly prove their effective adoption as magnonic nanoantennas. In this regard, a breakthrough has been accomplished compared to the previous work in [16]. In fact, the ultimate scope of the project was the realization of a *versatile* and *reconfigurable* optically-inspired spin-wave-based platform. Especially, the blended employment of tam-SPL technique and synthetic antiferromagnetic structures, besides overcoming the problem of generating SW with nanoscale wavelengths, have further allowed to engineer their wavefronts both to focus them, and to produce robust interference patterns. Moreover, the one-way propagation of SW has been observed as a direct consequence of their non-reciprocal nature in SAFs.

In the next few paragraphs a summary of the relevant steps required to achieve the final devices is described, namely the growth of the materials stack, its magnetic characterization and the subsequent standard optical lithography. Among the various stages comprehending the fabrication as a whole, the stress is particularly addressed to the optimization procedures and the related underlying physical reasons. I carried out personally these steps at PoliFAB, the micro and nanofabrication centre of Politecnico di Milano. Instead, the magnetic patterning of the specimens by tam-SPL was executed by Dr. Edoardo Albisetti, at the CUNY-Advanced Science Research Center, New York. The conclusive part of the chapter highlights the outcomes of the measurements performed at the PolLux beamline of the SLS synchrotron facility, hosted in Villigen. The experiments, to which I collaborated too,

were mainly devoted to the imaging by X-ray Magnetic Circular Dichroism-Scanning Transmission X-ray Microscopy (XMCD-STXM) the SW dynamics and their propagation.

## 4.1 Samples growth and magnetic characterization

The CoFeB/Ru/CoFeB/IrMn/Ru stack reported in Fig. 4.1 coincides with the first magnonic platform developed in this work. Its overall magnetic behaviour results from the interplay between two interactions, namely the exchange bias (EB) at the CoFeB/IrMn interface, and the interlayer exchange coupling (IEC) among the magnetizations of the two CoFeB films. Especially, the last, mediated via the Ru interlayer, results in the main building block of the multilayer, i.e. a synthetic antiferromagnet (SAF).

Broadly speaking, a SAF consists of two ferromagnets, separated by a nonmagnetic spacer, whose magnetizations at remanence point in opposite directions. The large tunability of its magnetic properties, achieved by controlling the layers thickness and material composition, makes SAFs widely used within both the spintronic [84] and the magnonic field [16]. As for the latter, the absence of a significant stray field emanated from a SAF, indeed has a positive impact on the spin waves wavelength and the propagating modes. For the purposes of the current research thesis, a symmetric system CoFeB/Ru/CoFeB was designed, where each ferromagnetic layer is constituted of an amorphous $Co_{40}Fe_{40}B_{20}$ alloy. This alloy is particularly suited for operations involving spin waves, since it possesses a small Gilbert damping parameter and a large saturation magnetization, which respectively ensure long spin waves propagation distances and high working frequencies [3]. The choice of Ru as interlayer was dictated by the strong antiferromagnetic coupling it supports, which has also been found stable against annealing up to temperatures greater than 350 °C [85]. Especially, the last feature allows the structure to be stable even at the temperatures required for the subsequent magnetic patterning (see Paragraph 4.2).

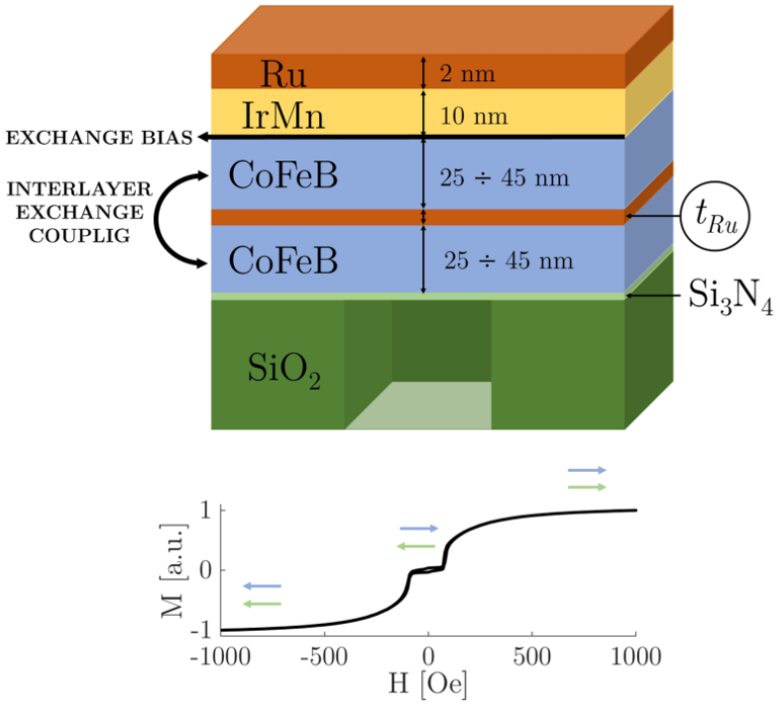


**Figure 4.1:** Sketch of the sputtered samples. The major interactions governing its magnetic behaviour are highlighted, namely the exchange bias interaction at the upper CoFeB/IrMn interface, and the interlayer exchange coupling among the magnetizations of the CoFeB layers. The parameter $t_{Ru}$, which determines the sign of the last term, is circled on the right. The bottom inset illustrates the normalized in-plane hysteresis loop for 45 nm thick CoFeB films and $t_{Ru}$ = 0.6 nm (optimized heterostructure), after the annealing at 250 °C in the in-plane +4 kOe initializing field. Pale blue and green arrows show the direction of the magnetization of the top and bottom ferromagnetic layer, respectively.

Consider Fig. 4.1. In such a system, by exploiting both the EB and the IEC, it is possible to set the overall magnetic remanence configuration. In fact, on the one hand, the orientation of the EB pins the magnetization of the uppermost FM, by inducing a uniaxial anisotropy; on the other hand, the magnetizations of either the CoFeB layers are coupled via IEC. Especially, at remanence, the two magnetizations can lie in a parallel or antiparallel configuration, depending on the thickness of the Ru interlayer $t_{Ru}$ (see Chapter 2). Thus, in zero external field, a necessary condition to achieve an antiparallel ordering of the magnetizations consists in properly tailoring $t_{Ru}$. To

actually enable a *unique* magnetic remanence configuration, an adequate EB must be exerted on the pinned FM, as to completely displaced its hysteresis loop from the origin. In this regard, the bottom inset in figure shows the hysteresis loop for the optimized heterostructure. Whereas for large negative (positive) fields, the magnetization of both the FMs is saturated along -$x$ ($+x$) direction, by decreasing the magnitude of the applied field, the IEC promotes at remanence the antiparallel alignment in the SAF. Nevertheless, the attained antiferromagnetic arrangement is not random at all; in fact, at low fields, the unidirectional anisotropy set by the EB forces the orientation of the top-pinned CoFeB magnetization along the positive direction of the $x$-axis. Hence, the combined effect of these interactions makes sure that in zero-applied field the magnetizations of the two layers are aligned antiferromagnetically, and that the in-plane orientation of the magnetizations is determined *only* by the direction of the EB. Besides, the robustness of the IEC is confirmed by the characteristic plateau observed around $H = 0$.

The design specifications of the samples had to match several constraints, arising both from the tuning of the aforementioned interactions, and the small thicknesses claimed by STXM experiments. Indeed, the experimental observation of spin waves via STXM requires the synchrotron radiation to be transmitted *through* the samples, which consequently need to be thin enough. In this regard, the guiding principle was to choose the materials layers thickness as small as possible. To this purpose, whereas to assess the magnetic and thermal properties of the multilayer, preliminary samples were grown on thermal oxidized bulk supports, the final investigation of the spin dynamics was carried out by depositing the optimized materials stack on 200 nm thick silicon nitride ($Si_3N_4$) membranes (see Fig. 4.1). The latter are perfectly smooth, chemically inert, mechanically stable and sustain heating up to 1000 °C, letting tam-SPL be properly performed.

Nonetheless, since the XMCD signal is strongly related to the amount of ferromagnetic material, the CoFeB layers could not be too thin. Moreover, the large FMs thicknesses are needed both to reduce the presence of defects and impurities, this way enlarging the SW travelling paths [86], and to exploit the relevant features of propagating modes in SAFs. For instance,

their localization in specific interfaces, together with non-reciprocal dispersion relations and nanometre wavelengths [16], are achieved only in the limit of semi-infinite FMs [83]. However, this wide-thicknesses demand clashes with the interfacial nature of the interactions present in the exchange-biased SAF, so to make appear a further hindrance to the concrete fabrication of the samples. Indeed, both EB and IEC strength diminishes as the thicknesses of the ferromagnetic layers grow.

As sketched in Fig. 4.1, the starting investigated materials stack consisted of CoFeB($x$)/Ru($t_{Ru}$)/CoFeB($x$)/IrMn(10)/Ru(2) (thicknesses in nanometres), with $x$ and $t_{Ru}$ ranging between 25–45 and 0.6–1 nm, respectively. The choice of 10 nm for IrMn basically resulted from two reasonings. On the one hand, raising the thickness of the polycristalline IrMn, the dimensions of its grains increase as well. This fact makes both the blocking temperature $T_B$ and the exchange bias to follow a similar growing trend [87], stemming from the average contribution of different sized grains, whose thermal instability lowers by thickening the AF. Especially, $T_B$ exceeds the room temperature at about 4–5 nm, and so these numbers are the minimum target for the devices to be magnetically patterned. On the other hand, this pace is interrupted for thicker layers (around 10 nm), at which the EB first saturates, and then starts decreasing with the AF thickness $t_{AF}$, roughly as $1/t_{AF}$. For instance, in Co/IrMn/Co trilayers, $\sigma_{ex}$ tends to vanish for $t_{AF}$ less than 5 nm, while it achieves its maximum for $t_{AF}$=10 nm [88] (the result is strictly valid only for IrMn, since it depends on the material-specific width of the magnetic domain walls inside the AF). Furthermore, past experience with a similar exchange biased system lead to an optimal $t_{AF}$=10 nm [14], ensuring $\mathbf{H}_{EB}$ = 35 ± 5 Oe and $\mathbf{H}_{co}$ = 20 ± 5 Oe, i.e. a completely shifted hysteresis loop for the upper FM. Thus, the reported optimization procedure regards the thickness of the Ru spacer $t_{Ru}$, whose optimal value has been simultaneously attained by varying the thickness for the CoFeB films.

All samples were grown via magnetron sputtering, with the conditions listed in Table 4.1. An in-plane magnetic field was applied during each deposition to promote the EB between the CoFeB top-pinned layer and the nearby AF. Then, the magnetic hysteresis loops of the sputtered samples

| Material | Mode | Ar pressure | Power | Rate |
|---|---|---|---|---|
| - | - | mTorr | W | nm/min |
| $Co_{40}Fe_{40}B_{20}$ | DC | 3.5 | 58 | 1.35 |
| Ru | DC | 5 | 50 | 2.18 |
| $Ir_{22}Mn_{78}$ | DC | 3 | 50 | 2.6 |
| $SiO_2$ | AC | 2.2 | 280 | 1.06 |

**Table 4.1:** Magnetron sputtering deposition conditions for synthetic antiferromagnetic structures.

were recorded by Vibrating Sample Magnetometry (VSM). To stabilize the interfaces and the magnetic configuration, each measurement followed a thermal annealing at 250 °C for 5 minutes, in an in-plane magnetic field $\mathbf{H}_{in}$ of 4 kOe oriented as the one applied during the growth (the impact of this thermal treating is better described below). The analysis of the magnetic characterizations have primarily guided the calibration of the Ruthenium thickness $t_{Ru}$, since it heavily influences the IEC and the coupling sign among the magnetizations of the two CoFeB layers. Besides, the reversal temperature $T_r$, namely the one needed to reverse the EB, was evaluated by field cooling the samples and subsequently measuring their hysteresis loops. The whole procedure was accomplished via the VSM instrument, which permitted to adjust contemporarily the applied field and the target temperature by means of a blowing $N_2$ heated flux. To simulate the effect of a fictitious run of tam-SPL, a 1 kOe field was applied in the opposite direction to the initializing field; the setpoint temperature was maintained for 20 seconds, then the samples were cooled down to room temperature. Later, the reversal temperature was evaluated by measuring the hysteresis loop. A complete overturning of the last with respect to the origin corresponded to a reversal of EB (see Fig. 4.4).

In what follows, the optimization of $t_{Ru}$ as a function of the CoFeB layers thickness is described. Based on the work in [14], the initial trial materials stack was constituted by CoFeB(25)/Ru($t_{Ru}$)/CoFeB(25)/IrMn(10)/Ru(2), where $t_{Ru}$ was decreased in steps of 0.1 nm starting from $t_{Ru}$ = 0.9 nm. Fig. 4.2 reports the subsequent hysteresis loops for this set of specimens as a

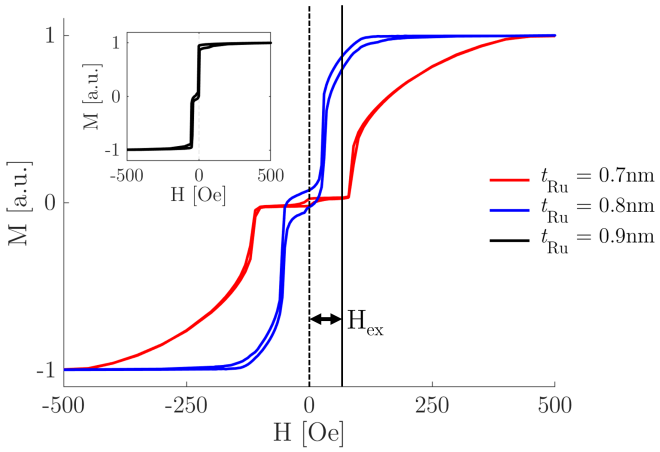


**Figure 4.2:** In-plane hysteresis loops for the materials stack comprised of CoFeB(25)/Ru($t_{Ru}$)/CoFeB(25)/IrMn(10)/Ru(2) (thicknesses in nm), where the interlayer Ruthenium thickness ranges from $t_{Ru}$ = 0.7 nm to $t_{Ru}$ = 0.9 nm in steps of 0.1 nm. Each curve has been acquired after the annealing of the samples at 250 °C in an in-plane +4 kOe initializing field, as proved by the small shift of the loops towards the negative x-axis. The field around which the lobe related to the free FM is centered ($H_{ex}$) gives the strength for the IEC for all the three cases (for a clearer visualization, it is reported only the one for $t_{Ru}$ = 0.8 nm).

function of $t_{Ru}$. The cycles can be thought as the sum of those corresponding to each individual CoFeB layer. Especially, for any $t_{Ru}$, the first loop, shifted from the origin, corresponds to the rotation of the pinned CoFeB film, whereas the second curve refers to the rotation of the magnetization of the other ferromagnet. The role played by $\mathbf{H}_{in}$ on the EB becomes manifest by looking at the loops as a whole, which are not centred around the origin; in fact, since the initializing field pointed in the positive direction with respect to the reference x-axis, the cycle for the exchange-biased FM is shifted by a tiny amount in the negative direction (at remanence the EB forces the magnetization of the top-pinned layer to lie towards the positive x-axis). Another common thread shared by the three curves in Fig. 4.2 is the horizontal plateau across $H$ = 0, which sharpens by lowering the Ruthenium interlayer thickness. In this regard, the IEC strength $H_{ex}$ was assessed for each $t_{Ru}$ as depicted in figure, i.e. by considering the field around which the lobe for the free FM is centered. A quantitative analysis of the hysteresis loops has lead to $H_{ex}$ = 0 Oe, $H_{ex}$ ~ 66 Oe and $H_{ex}$ ~ 250 Oe, for $t_{Ru}$ = 0.9 nm, $t_{Ru}$ = 0.8

nm and $t_{Ru}$ = 0.7 nm, respectively. Thus, albeit IEC is an interfacial interaction, our findings suggest its strength to be large enough even with thicker FMs, as in the present work. Indeed, by diminishing $t_{Ru}$, $H_{ex}$ strengthens and the magnetizations of the CoFeB layers are forced in an antiparallel arrangement in zero-applied field, which is eventually established for $t_{Ru}$ = 0.7 nm. In this condition, the measured magnetic signal is vanishingly small in a wide range of the applied field, testifying the effectiveness of the interlayer exchange coupling in setting the magnetizations of the two FMs antiparallel. On the contrary, the case for $t_{Ru}$ = 0.9 nm (in the inset on the left) results in a zero of the IEC ($H_{ex}$ = 0 Oe), since the corresponding loop is a nearly the decoupled sum of the ones of the two FMs, in good agreement with [85].

Hence, lead by the aforementioned need of as much ferromagnetic material as possible, a new batch of samples was designed. To this aim, the ultimate goal was to achieve comparable thicknesses for the FMs as in [16], namely of the order of 40 nm, with still strong enough IEC and EB. The new stacks were made up of CoFeB(35)/Ru($t_{Ru}$)/CoFeB(35)/IrMn(10)/Ru(2), with $t_{Ru}$ ranging from 0.6 nm to 0.8 nm. The choice for $t_{Ru}$ was driven by the experimental evidences of Fig. 4.2: the less it is, the stronger is the antiparallel coupling. The same annealing procedure as before brought to the hysteresis loops of Fig. 4.3. Even though the plots show a similar behaviour with respect to the ones in Fig. 4.2 (note that now the applied external field ranges from -1 kOe to +1 kOe), two major differences appear. First of all, the values of $H_{ex}$ for different $t_{Ru}$ increase on average: $H_{ex}$ = 0 Oe for $t_{Ru}$ = 0.8 nm, $H_{ex} \sim$ 213 Oe for $t_{Ru}$ = 0.7 nm, $H_{ex} \sim$ 530 Oe for $t_{Ru}$ = 0.6 nm. Surprisingly, though IEC is an interfacial interaction, by raising the thickness of the two FMs, its forcefulness boosts as well. This datum can be mainly attributed to enhanced growth conditions, in other words better base pressure of the chamber and cleanness of the targets, achieved through several repeated depositions. Besides, the antiparallel IEC is biased towards smaller $t_{Ru}$. In fact, comparing the two insets on the left in Figs. 4.2 and 4.3, the curves are basically identical. As qualitatively sketched in the plot on the right of Fig. 4.3, for 35 nm thick CoFeB layers the IEC thus vanishes for $t_{Ru}$ = 0.8 nm. Scaling $t_{Ru}$, the magnetizations of the two FMs gain a clear antiferro-

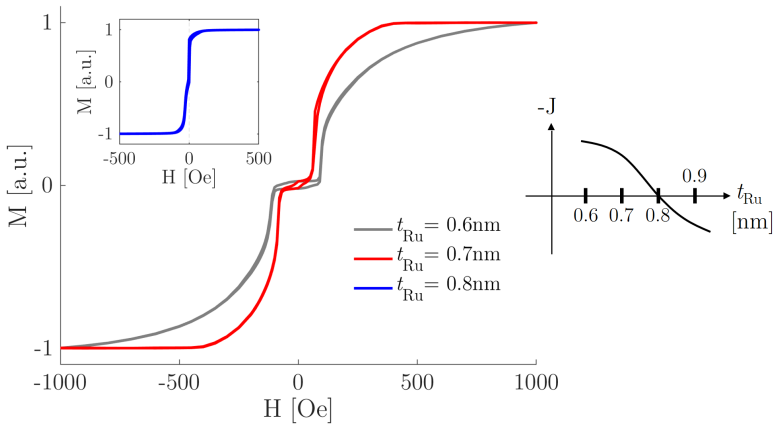


**Figure 4.3:** In-plane hysteresis loops acquired for the second set of samples, made of CoFeB(35)/Ru($t_{Ru}$)/CoFeB(35)/IrMn(10)/Ru(2) (thicknesses in nm). Now the range of values for $t_{Ru}$ is shifted by 0.1 nm towards smaller thicknesses, namely it varies from $t_{Ru}$ = 0.6 nm to $t_{Ru}$ = 0.8 nm (same colour-map of the previous figure). Unlike the trend for 25 nm thick CoFeB layers, the zero of the interlayer exchange coupling is moved to $t_{Ru}$ = 0.8 nm, as depicted by the corresponding loop shown in the upper-left inset. On the right, a qualitative behaviour of the interlayer exchange constant J against $t_{Ru}$ is sketched.

magnetic ordering for $t_{Ru}$ = 0.6 nm, where the slope of the central plateau is nearly equal to zero, and it extends over a wide range of the applied field values. Moreover, the data acquired for $t_{Ru}$ = 0.9 nm and $t_{Ru}$ = 1 nm (not reported here) have upheld the previous reasoning, exhibiting hysteresis loops as the ones ascribed to a single 70 nm thick ferromagnet (35 nm + 35 nm). Therefore, for greater Ruthenium thicknesses the sign of J reverses, entailing a parallel coupling of the magnetizations.

At this stage, the magnetic properties of the systems upon different thermal treatments are discussed. Especially, to verify the capability of practically employing tam-SPL technique, the specimens were compelled to several repeated processes of field cooling. It has been so possible to assess the overturning of the EB, fundamental for tam-SPL, and to establish the reversal temperature $T_r$ for the samples, which was found to be roughly equal to 250 °C independently from the thickness of the CoFeB films. In this regard, Fig. 4.4 compares the cases of 25 nm and 35 nm thick

CoFeB layers for $t_{Ru}$ = 0.7 nm. Particularly, it shows the hysteresis loops of CoFeB(25)/Ru(0.7)/CoFeB(25)/IrMn(10)/Ru(2) **(a)** and CoFeB(35)/Ru(0.7) /CoFeB(35)/IrMn(10)/Ru(2) **(b)** stacks, as grown (upper black curves), following the first annealing at 250 °C in the initializing field (red curves), and after the field cooling at 250 °C in an in-plane -1 kOe field $\mathbf{H}_{fc}$ (brown curves). A preliminary observation can be deduced from the comparison between the black and the red loops, which traces the aforementioned favourable action of the first annealing. In fact, following the heating of the specimens, the slopes of the central region of the cycles diminish (see in **(a)** the different slopes of the green lines). This trend is common to all the films, irrespective of both $t_{Ru}$ and the thicknesses of the CoFeB layers, and suggests a reinforcement in the IEC between the two ferromagnets. A possible explanation resides in the better structural ordering at the CoFeB interfaces, which in turn means approaching the idealized situation discussed in Chapter 2. In addition, the curves become more squared off, possibly because of a further improvement also in the interfacial magnetic landscape of the ferromagnets. In this regard, under the action of thermal fluctuations, the grains inside the two CoFeB films likely merge together, and the sizes of the magnetic domains are consequently enlarged. The behaviour of the extremities of the loops in figure can corroborate this assumption: in the as grown heterostructures the field required to saturate the magnetization exceed the one for the annealed samples, and the 'stretched' ends of the lobes are mainly due to the rotation of the macroscopic magnetization vector via magnetic domains expansion.

Moreover, from Fig. 4.4 it is possible to determine the reversal temperature $T_R$ of the system. To this purpose, consider for instance panel **(a)**. By comparing the two lowest-lying hysteresis loops (the red and brown curves), it is straight to conclude that each lobe has been shifted. As a matter of fact, in the red cycle the first lobe is centered on a negative field $-H_A \sim -250$ Oe, and it is related to the exchange-biased ferromagnet; the other lobe, centered on the vertical line passing through $+H_B \sim +185$ Oe, corresponds to the dynamics of the magnetization inside the free layer. Therefore, the first CoFeB layer following the field (for negative values) is the uppermost one, pinned with the EB. On the contrary, for the brown cycle (the one collected

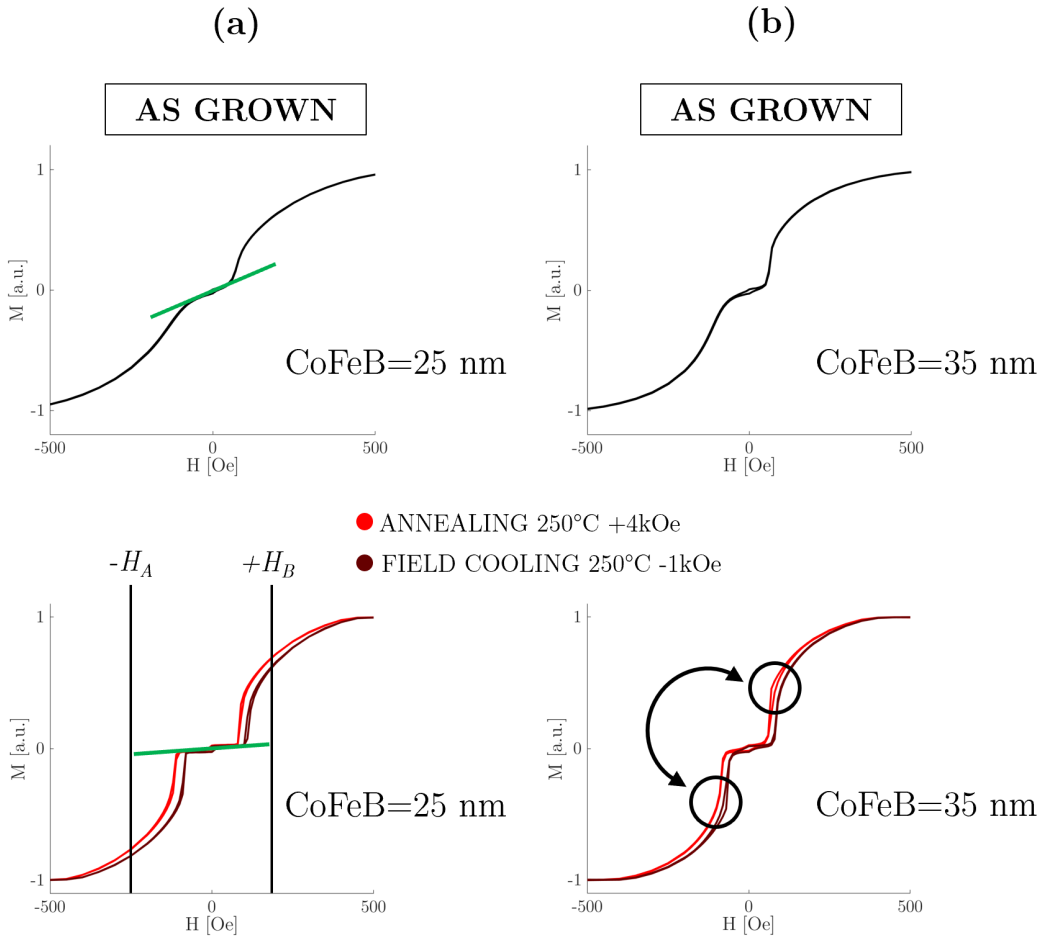


**Figure 4.4:** In-plane hysteresis loops for $t_{Ru}$ = 0.7 nm recorded 'as grown' (black), after the initial annealing at 250 °C in an in-plane +4 kOe initializing field (red), and following the field cooling of the samples at 250 °C in an in-plane -1 kOe field (brown). Both the cases of 25 nm **(a)** and 35 nm **(b)** thick CoFeB layers are shown. The different slopes of the plateau around $H$ = 0 are traced with a green line for **(a)**, either for the cycle as grown (upper black curve), and for the ones following the thermal treatments (bottom red and brown curves).

after the field cooling), the first lobe is centered on $-H_B \sim -185$ Oe, thus corresponding to the free bottom FM (first now to rotate), while the second lobe is centered on $+H_A \sim +250$ Oe and refers to the pinned FM. Indeed, a better inspection of panel **(b)** in Fig. 4.4, reveals that the hysteresis loop, recorded after the initial annealing, has been *completely* reversed via field cooling, given that the circled features at the positive fields in the red curve have moved to negative fields in the brown one. Furthermore, $T_r \equiv 250$ °C since, on the one hand, a further raising in the field cooling target temperature did not significantly affect the shape of the brown loops; on the other hand, for $T < 250$ °C the EB was not entirely flipped.

Motivated by the promising results of a strong antiparallel coupling for $t_{Ru}$ = 0.6, which was essentially unaffected with the thickness of the CoFeB layers, and by the possibility for the EB to be reversed, and so to write the magnetic configuration at remanence, the thickness of the CoFeB was further increased to 45 nm, with $t_{Ru}$ = 0.6 nm and $t_{IrMn}$ = 10 nm. The corresponding hysteresis loop, acquired after the first annealing, is the one shown in Fig. 4.1. Even for $t_{CoFeB}$ = 45 nm, the IEC was found to be able to force at remanence the antiparallel alignment of the two CoFeB layers (with $H_{ex} \sim 530$ Oe). Besides, as discussed at the very beginning, in zero-applied field the *unique* arrangement for the two magnetizations (no matter the direction of approaching the origin) is set by the unidirectional anisotropy imposed via EB on the uppermost FM. Lastly, as in the preceding figures, the robustness of IEC is confirmed by the characteristic plateau observed around $H$ = 0. For the present materials stack the reversal temperature was re-evaluated, ascertaining a slight shift towards higher values, namely 275–300 °C, which anyway let the subsequent magnetic writing via tam-SPL doable. Thus, in what follows, all the description will be referred to specimens constituted by CoFeB(45)/Ru(0.6)/CoFeB(45)/IrMn(10)/Ru(2).

## 4.2 tam-SPL and optical lithography

Once the right materials stack, fulfilling all the above requirements, was identified in CoFeB(45)/Ru(0.6)/CoFeB(45)/IrMn(10)/Ru(2), the next step was the fabrication of the magnonic devices. Thus, the heterostructures were deposited by magnetron sputtering on suitable supports, constituted by silicon nitride membranes 200 nm thick, etched in bulk silicon oxidized substrates (see Fig. 4.1). As before, to stabilize the exchange bias at the CoFeB/IrMn interface, the samples were housed in a in-plane magnetized sample-holder. This time, sputtering was followed by a magnetic thermal annealing in a vacuum chamber (see Chapter 3), to have a better control on the temperature and preserve the sample surface from contaminants. The temperature was increased at a rate of 5 °C/min and was maintained at 250 °C for 5 minutes. Meanwhile, an in-plane 4 kOe initializing field was imposed, by means of a permanent magnet, in the same direction of the one applied during the growth.

The resulting heterostructures were finally ready to be magnetically patterned via tam-SPL, allowing the writing of domain walls (DWs) to be exploited as magnonic nanoantennas. The patterning was performed at CUNY-ASRC by means of a nanofrazor explorer (SwissLitho AG). Spin-textures were patterned by sweeping in a raster-scan fashion the scanning probe, heated above the blocking temperature of the exchange bias system , at about 300° C, in presence of an external magnetic field. Two rotatable permanent magnets were employed for generating a uniform external magnetic field applied in the sample plane during the patterning. The high degree of versatility of tam-SPL technique has allowed to draw arbitrarily shaped spin textures. For instance, examples of angled **(a)** and curved **(b)** 180° Néel DWs traced on the membranes are illustrated in the Magnetic Force Microscopy (MFM) images of Fig. 4.5. Notice that, in either the panels, since the tip used to scan the surface was magnetized along its axis, only the polar component of the emanating stray field was sensed. Thus, adjacent in-plane magnetized domains appear with the same colour, though the inside magnetization lies in opposite directions. The reason why DWs instead appear as dark lines

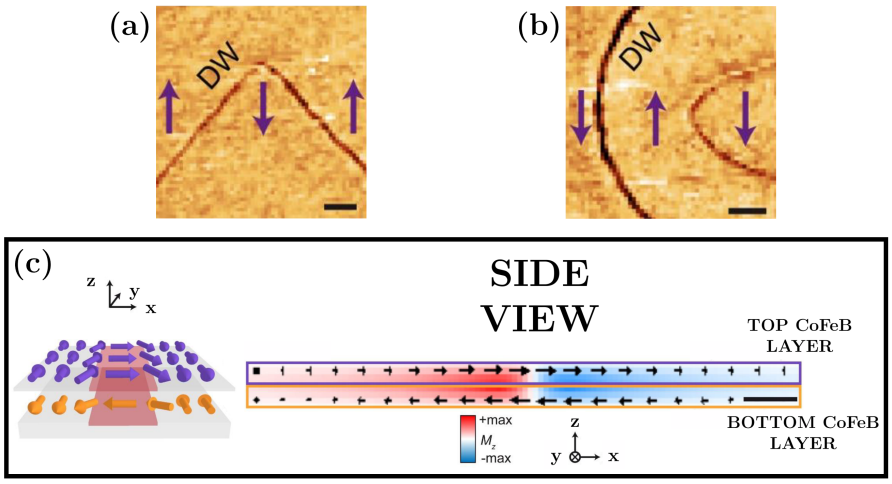


**Figure 4.5:** MFM images of angled **(a)** and curved **(b)** 180° Néel domain walls patterned via tam-SPL. The purple arrows indicate the direction of the equilibrium magnetization in the top CoFeB layer. Panel **(c)** shows the simulated magnetic configuration inside the top and bottom CoFeB films, highlighted by purple and orange boxes, respectively. Especially, the black arrows mark the direction of the magnetization, while the colours trace the out-of-plane component of the magnetization. Scale bar in **(a)** and **(b)** corresponds to 3 µm, whereas in **(c)** to 200 nm. Simulations in panel **(c)** were performed by Dr. Edoardo Albisetti.

is provided in panel **(c)** of the same figure, which sketches a micromagnetic simulation of the magnetic arrangement of a DW in a SAF. In fact, the configuration simulated in panel **(c)** shows the magnetization in the two CoFeB layers pointing everywhere in opposite directions. However, moving towards the central part of the DW a partial out-of-plane canting of the magnetization occurs (the colour contrast increases in the insets), and this is exactly the contribution measured in panels **(a)** and **(b)**. Besides one-dimensional DWs, several geometries have been exploited, including point-like topological magnetic quasiparticles [89] for the emission of radial wavefronts. Anyway, the inspiring idea was always to generate 'engineered' spin waves, by accordingly drawing the emitter.

The patterning of features as those depicted in Fig. 4.5 allowed an efficient way for tailoring spin waves wavefronts at the nanoscale. Indeed, by coupling the shaped magnonic nanoantennas with a radio-frequency external magnetic field, spin waves were expected to be launched thanks to the

oscillations of such spin textures. Especially, from **(c)**, it is reasonable to foresee the coupling to be among the component of the Oersted field parallel to the out-of-plane magnetization, as the overall in-plane magnetization in a SAF instead vanishes due to the IEC (at least for fields lower than $H_{ex}$). Consequently, idealizing the inductive antennas as straight lines over which a current flows, the $z$-component of the emanated magnetic field achieves its maximum just outside the conductive tracks: here the DWs have to be present. Hence, the magnetic writing needed to be followed by an optical lithography stage to design the inductive antennas destined to excite DWs. In order to electrically insulate the antennas from the magnetic film, firstly 50 nm of insulating $SiO_2$ were deposited by RF magnetron sputtering. Later, the ordinary steps of a typical direct lithography were carried out, except the baking procedure. Even if the estimated reversal temperature of the exchange bias SAF was higher than the baking temperature, a room temperature process was carried out in order to avoid the risk of erasing the magnetic patterns. After AZ5214E resist deposition through spin coating (see Paragraph 3.1.2), to promote the evaporation of the solvents from the resist and its hardening, the membranes were kept in low vacuum inside the entry chamber of the magnetron sputtering machine for 30 minutes. Next, the exposure was accomplished via the MaskLess Aligner 100 (MLA) instrument, as it allows to design arbitrary geometries without the need of a photomask and to align the pattern with the underlying substrate. In fact, there were strict constraints on the antennas positions for they needed to be aligned with the beneath magnetic patterns, albeit the last were not visible optically, since the patterning is purely magnetic. To this purpose, the patterns were localized via MFM with respect to the corners of the membranes (see Fig. 4.6), subsequently exploited as references. Each microstrip antenna was singularly designed on the basis of the corresponding membrane, aiming to crossing the written spin texture. They were all constituted by two pads, for the ground and signal contacts respectively, joined by a narrow line with a nominal width ranging from 1.5 µm to 5 µm (see for instance panel **(b)**). In particular, their sizes had not to be neither too low, to avoid local heating atop the magnetic pattering, nor too high, otherwise the Oersted field gen-

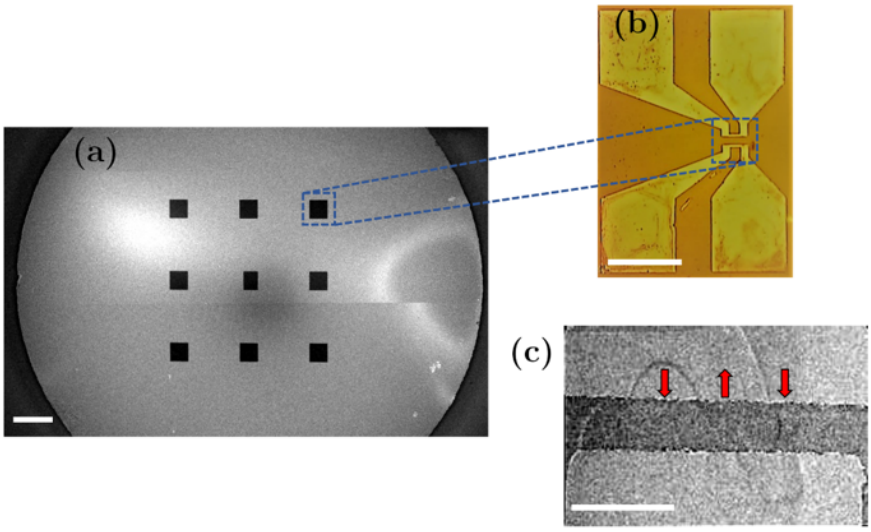


**Figure 4.6:** SEM image **(a)** of the membranes used to support the magnetic stack. Inset **(b)** shows an optical microscopy image of an illustrative inductive antenna defined by optical lithography atop a $Si_3N_4$ membrane. Finally, in **(c)** a static XMCD–STXM image of the out-of-plane magnetization component for a finished sample reveals the good alignment achieved between the position of the magnetically patterned features and the one of the lithographed antennas (the red arrows show the direction of the magnetization in the top CoFeB layer). The scale bars correspond to 200 µm for **(a)** and **(b)**, and to 10 µm for **(c)**, respectively.

erated by the flowing of the injected current could be not strong enough to trigger the DWs oscillations. After exposure, the development was performed in AZ 726MIF for 30 s, followed by a rinse in DI water.

Lastly, the fabrication finished with the deposition of Cr(7 nm)/Cu(200 nm) bilayer by means of electron beam evaporator (chromium was used as adhesion layer) and the following standard lift-off. Indeed, Copper was preferred to Au, normally used for fabricating electrical contacts, due to its greater transparency to X-rays radiation. All the antennas had resistances about few Ω, 30 Ω at most. In Fig. 4.6 an exemplary static XMCD-STXM image of the domain wall crossing the stripline confirms that the alignment procedure has been carried out correctly.

## 4.3 Results and discussion

The excitation of the patterned spin textures and the imaging of the emitted spin waves were carried out with time-resolved scanning transmission X-ray microscopy at the PolLux endstation of the Swiss Light Source, at PSI. Monochromatic X-rays at the Co $L_3$ absorption edge (781 eV) were focused by a Fresnel zone plate onto a diffraction-limited spot on the sample, and the transmitted photons were collected through a detector behind the sample-holder. Static and time-resolved images were recorded from raster scanning the sample through the focal point within a variable magnetic field (0 mT ÷ 10 mT). To probe the out-of-plane magnetization component $M_z$ in SAFs, i.e. the one supposed to be potentially coupled with the Oersted field generated by the inductive antennas, the specimens were mounted perpendicularly to the incident X-ray beam (see Chapter 3). The typical point-resolution ranges from 50 nm to 100 nm, and, to enhance the signal-to-noise ratio, the signal arising from each single pixel was integrated on a certain time window. The normalized images reported below were formed by sensing one photon helicity only (circular negative) and by subtracting pixel-by-pixel the measured intensity average value over one period of oscillation of the pump signal (see Paragraph 3.2.3 and below). The temporal resolution in magnetization dynamics movies resulted from the synchronization between the bunched X-ray pulses (70 ps FWHM) and the RF input to the inductive antennas. In this regard, AC voltage signals with 1500 mV amplitude peak-to-peak, constantly tracked by means of an oscilloscope, were fed to the lithographed contact pads to drive the DWs stimulus. The pumping signal was synchronized to the 500 MHz master clock of the synchrotron light source (the X-ray flashes generated by the light source) through a field programmable gate array (FPGA) setup. Due to the specific requirements of the FPGA-based pump-probe setup installed at the PolLux endstation, RF frequencies of $500 \times (M/N)$ [MHz] were accessible, being $N$ a prime number and $M$ a positive integer. For the measurements presented in this work, $N$ was typically selected to be equal to 7 (namely each video is comprised of 7 frames), giving a phase resolution of about 50° in the time-resolved images.

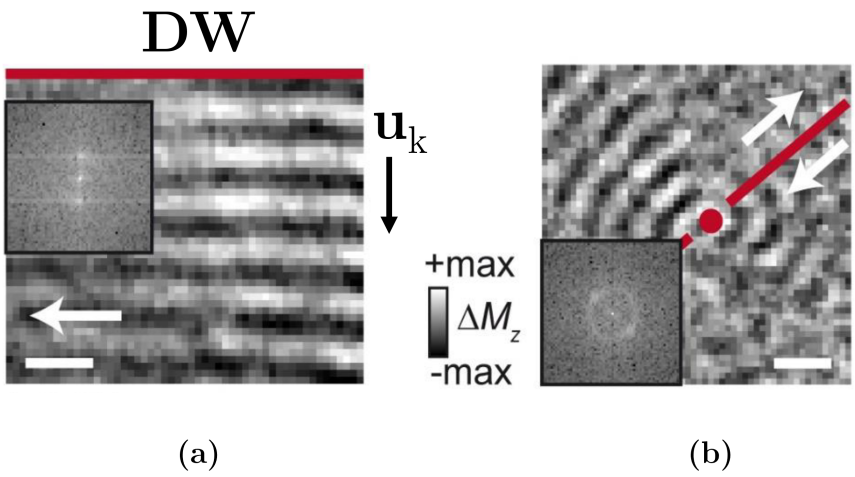


**Figure 4.7:** Normalized STXM images of linear **(a)** and radial **(b)** wavefronts excited by a straight domain wall ($f$ = 1.43 GHz) and a votex-Bloch line ($f$ = 1.57 GHz), respectively. The contrast arising from the XMCD distinguishes the magnitude of the out-of-plane component of the magnetization. Both the images are single frame extracted from a video reproducing the magnetization dynamics. The magenta line and dot show the position of the exploited domain wall and vortex. The smaller insets show the related two-dimensional spatial Fourier transform, while the white arrows the direction of the magnetization in the top CoFeB layer. The scale bars correspond to 500 nm. The image is taken from [E. Albisetti et al., submitted to Science Advance].

Depending on the RF frequency, the temporal resolution of the time-resolved images is given by $2/M$ [ns], with its lower limit amounting to the width of the X-ray pulses. The following pictures show the main outcomes achieved by investigating the heterostructures described so far.

Fig. 4.7 provides a first fundamental proof for the employability of spin textures as magnonic nanoantennas. Either the panels **(a)** and **(b)** are single frames extracted from a STXM video, constituted by an ordered sequence of such images. Especially, in **(a)** the magnetization inside a straight DW is excited by means of an external RF magnetic field $\mathbf{H}_{RF}$, and spin waves with planar wavefronts emanates away from the wall. The black-white contrast corresponds to oscillations of the out-of-plane component of the magnetization with respect to the mean $M_z$ value, and it is associated to the propagation of spin waves. In fact, as already explained, this contrast arises from the differential absorption of circularly polarized light by regions with opposite

out-of-plane magnetization component. In **(a)**, the DW location is specified by the upper magenta line, whereas the white arrow indicates the orientation of the magnetization in the CoFeB top layer. The smaller inset depicts the spatial two-dimensional Fourier transform of the image, wherein the localization of bright dots related to the propagating mode reveals a preferential emission perpendicular to the wall ($\lambda \sim 330$ nm). In **(b)**, a vortex-Bloch line [89], sited within a DW, launches spin waves with radial symmetry, as proved again by the Fourier transform. Indeed, the brighter dots are now arranged on a ring, corresponding to the excitation of individual linear wavefronts from the patterned spin texture. Moreover, the low ellipticity of the ring testifies that the spin waves wavelength weakly depends on the emission direction (since $k \propto 1/\lambda$ is nearly the same over all the in-plane directions). Therefore, either in **(a)** and **(b)**, the effect of $\mathbf{H}_{RF}$ is to excite dynamics inside the DWs, which in turn act as confined sources for the observed spin waves. Note that a similar behaviour has been theoretically predicted in [90] for analogue geometries.

To better visualize the wave nature of such generated spin waves in a 'static framework', panel **(a)** of Fig. 4.8 shows the spatial *interference* of spin waves with both planar and radial wavefronts. To this purpose, features as those in Fig. 4.7 were patterned nearby and simultaneously exploited as emitters. In the experimental STXM image of **(a)**, curved and straight coloured thin lines stand for the distinct propagating wavefronts, while the domain wall and the vortex structure are labelled with a magenta thick stroke and dot, respectively. As before, the contrast represents the variation $\Delta M_z$ in the out-of-plane component of the magnetization at a specific time (i.e. at a certain synchrotron radiation 'flash'). The colour-map modulation traces the actual physical picture: constructive interference maxima are identified as high intensity black/white regions, while destructive interference fringes occur in correspondence with low intensity, uniform grey zones. The underlying interference pattern is unambiguously caught in panel **(b)**, sketching the spatial distribution of the spin waves amplitude point-by-point. The latter has been extracted by fitting the time trace of each pixel with a sinusoidal function, whose amplitude was then extrapolated. In **(b)**, the areas

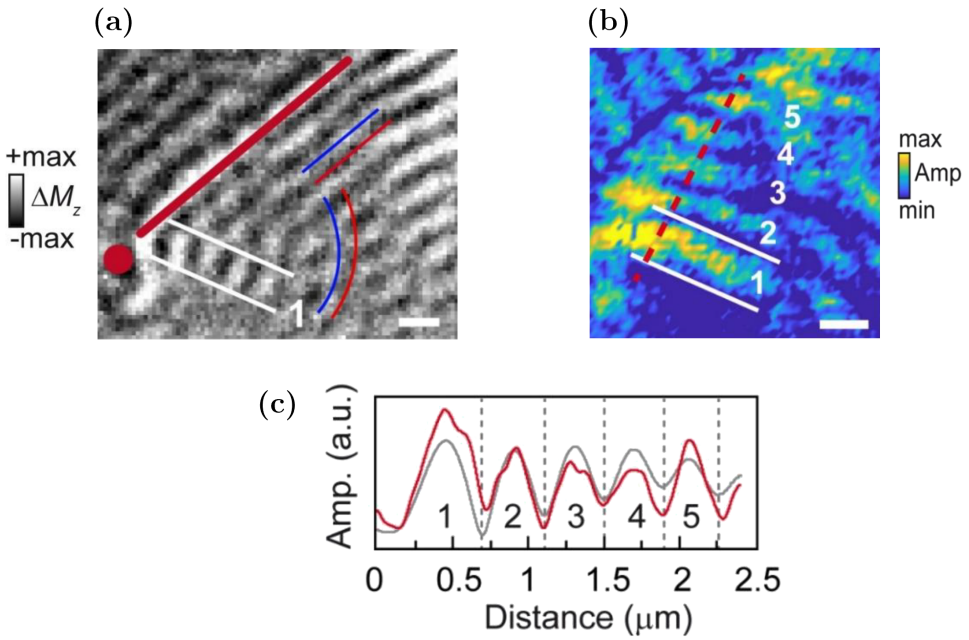


**Figure 4.8:** Imaging of the interference pattern arising from radial and linear wavefronts emitted by a vortex and a planar domain wall, respectively ($f$ = 1.29 GHz). In the experimental STXM image **(a)** the emitters correspond to the thick magenta stroke and dot. The thinner blue/red straight (curved) lines follow the linear (radial) wavefronts. **(b)** shows the spatial spin wave amplitude corresponding to **(a)**. Constructive fringes are yellow coloured, while blue regions stand for destructive troughs. The first interference maximum is highlighted by white lines in either panels **(a)** and **(b)**. In **(c)** is portrayed a comparison between the measured and simulated amplitude along the dashed red line in **(b)**. The scale bars correspond to 500 nm.

in which such waves coherently sum are marked in vibrant yellow; instead, blue regions arise where the spin waves superimpose in anti-phase. The first interference maxima (spaced by ~ 450 nm) are numbered for a comparison with panel **(c)**, which exhibits the measured and simulated spatial profile extracted from the dashed line in **(b)**. Indeed, the same geometry of **(a)** has been simulated with the GPU-accelerated software MuMax[3], and the grey profile in the inset **(c)** refers to the same of **(b)** for the simulation. As illustrated in the graph, the good agreement between experiments and theoretical model further proves the robustness of the designed multi-beam interference pattern, which benefits of the non-reciprocity nature of the propagating spin

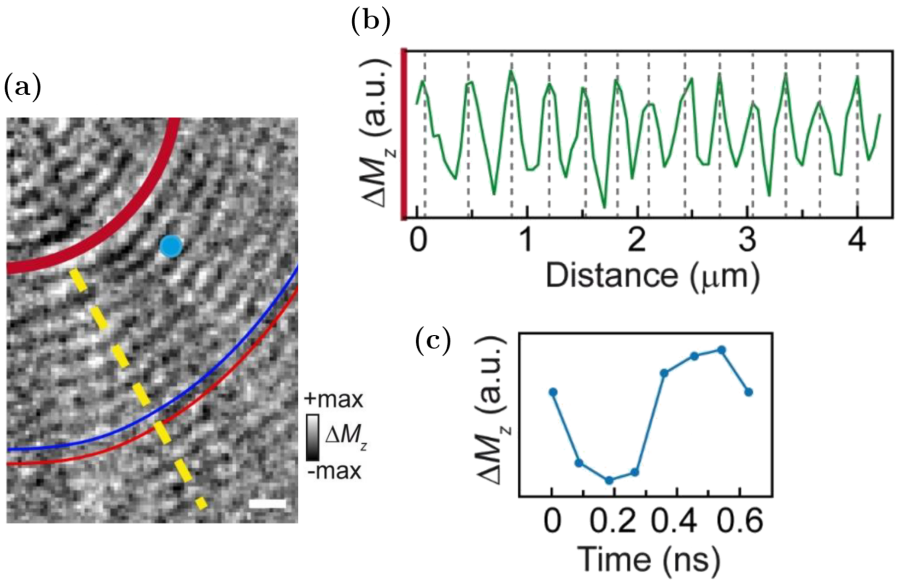


**Figure 4.9:** Experimental STXM image of the emanating spin waves emitted from a curved domain wall (marked with a thick magenta line) excited at $f = 1.57$ GHz. In **(a)** the alternated thinner blue/red arches signal the convex wavefronts. Panels **(b)** and **(c)** refer to the yellow dashed line and the blue dot in **(a)**, respectively. Especially, in **(b)** the oscillating magnitude of the normalized out-of-plane magnetization is traced ($\lambda \sim 330$ nm). Noteworthy, the signal is still high after 15 periods, being limited by the STXM acquisition window. In **(c)** the temporal profile extracted from the magnetization dynamics is sketched. The time resolution between two consecutive frames is 90 ps, very close to the ultimate limit imposed by the FWHM of the bunched synchrotron radiation. Scale bar: 500 nm.

waves (see below). Especially, the related one-way propagation is also the reason why the interference pattern is free from spurious contributions.

The enormous flexibility granted by tam-SPL technique also allowed to customize more complex spin textures respect to the ones addressed so far. As a matter of fact, curved DWs, as those reported in the MFM image of Fig. 4.6**(b)**, have been efficiently used to excite spin waves. For instance, Fig. 4.9 demonstrates the propagation of spin waves with convex wavefronts (alternated thin red/blue arches) from the DW indicated by the thick magenta line. As in the previous examples, the wavefronts maintain the geometry of the emitter, making possible to arbitrarily engineer the former by properly tailoring the latter. This result reveals that the Huygens-Fresnel principle

can be applicable even in the present case of oscillating DWs as emitters. Hence, each point on a certain wavefront can be thought as source of radial spin waves to retrace the overall waveform. Again, this feature arises from the nonreciprocal modes propagating in the SAF, [16], as will be discussed later. Furthermore, merging the pieces of information provided by panels **(b)** and **(c)**, which respectively show the experimental spatial and temporal profiles extracted from the yellow dashed line and blue dot in **(a)**, other two essential characteristics of the examined systems are disclosed. On the one hand, it is actually proved the effectiveness of generating spin waves with nanometre wavelength ($\lambda \sim 300$ nm from **(b)**) by coupling an oscillating spin texture ($f = 1.57$ GHz from **(c)**) with an external RF field; on the other hand, such spin waves travel micrometre distances before their amplitude decays (in **(b)** the signal is still high after 15 periods). Therefore, the developed platform enables the unique combination of short-wavelength modes, propagating over lengths exceeding several times their wavelength, whose wavefronts can be possibly engineered.

Especially, the last feature has already been exploited in the present work to design a prototype building-block for spin-waves-based analog devices. In fact, Fig. 4.10 sketches a curved nanoantenna, drawn with the aim of performing a focusing action on the launched modes. Taking advantage of the experimentally observed directional emission from the DW **(a)**, the energy carried by the spin wave ($\lambda \sim 330$ nm, $f = 1.43$ GHz) is driven in a controlled fashion within the shaped geometry. In figure, firstly the converging wavefronts propagate towards the beam waist at a distance $d_f \sim 2.5$ µm from the emitter; then, crossing this point (marked by the dashed yellow line in **(a)**), the beam concavity is reversed, passing from concave to convex. At the focal point, the spin wave lateral confinement is given by the full width at half maximum (FWHM) of the curve in **(b)**, equal to $w_f \sim 340 \pm 50$ nm. Notably, the arising picture resembles the one of panel **(c)**, where the optical emission from a curved source of finite dimension is considered. In that case, the smallest beam size at the focal point is set by the numerical aperture $2\alpha = 52°$ of the object (i.e. the DW in **(a)**), and can be esteemed via the Abbe formula as $w_f \simeq \lambda/2\sin(\alpha) = 363$ nm, in good agreement with **(b)**.

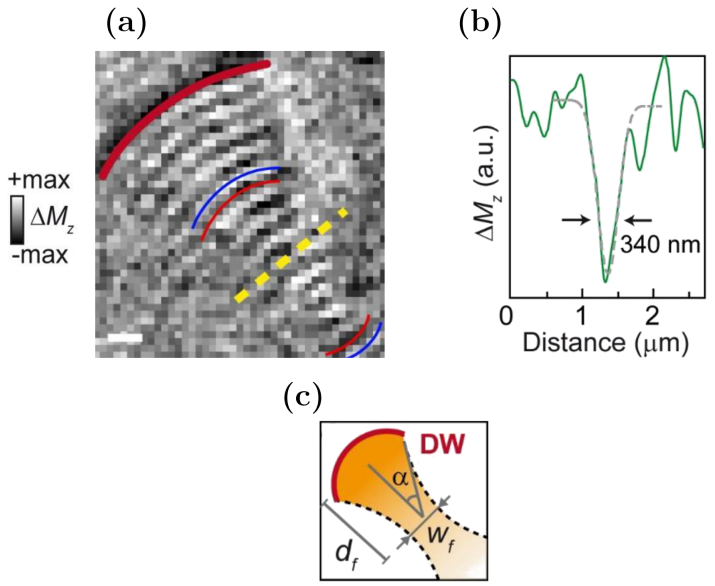


**Figure 4.10:** Implementation of a prototype spin waves focusing antenna. In **(a)** the STXM image ($f$ = 1.43 GHz) shows the reversal of the wavefronts, whose shape changes from concave to convex after the focal point, consistently with a focusing effect. The position of the beam waist is marked by a dashed yellow line, from which the spin waves amplitude signal in **(b)** is extracted. The FWHM of the beam at the focal point (placed 2.5 µm away from the emitter) is 340 ± 50 nm, i.e. comparable with its wavelength $\lambda \sim 330$ nm. **(c)** is the optical analogue of the spin-wave focusing by a magnonic nanoantenna with angular aperture $2\alpha = 52°$. Scale bar: 500 nm.

Ascertained the capability of patterning 'from scratch', via tam-SPL, DWs with arbitrary geometry, a further investigation has been carried out to assess potential changes in the magnetic landscapes, already established, as a function of the triggering frequency $f = f_{RF}$. Indeed, it sounds reasonable to await that the induced dynamics of the DWs magnetization depends on the coupling with the Oersted field generated in space by flowing currents inside the coplanar waveguides, and so ultimately on the stimulus frequency $f_{RF}$. Thus, fixed the usually 1500 mV amplitude peak-to-peak of the RF signal, and the value for a static in-plane magnetic field $H_{st} = -8$ mT, the excitation and transmission of spin waves from a previously drawn nanoantenna in SAF has been analysed. In this regard, the upper panels in Fig. 4.11 show the wavefronts launched from a DW at $f_{RF}$ = 1071 MHz, $f_{RF}$ = 1142 MHz and

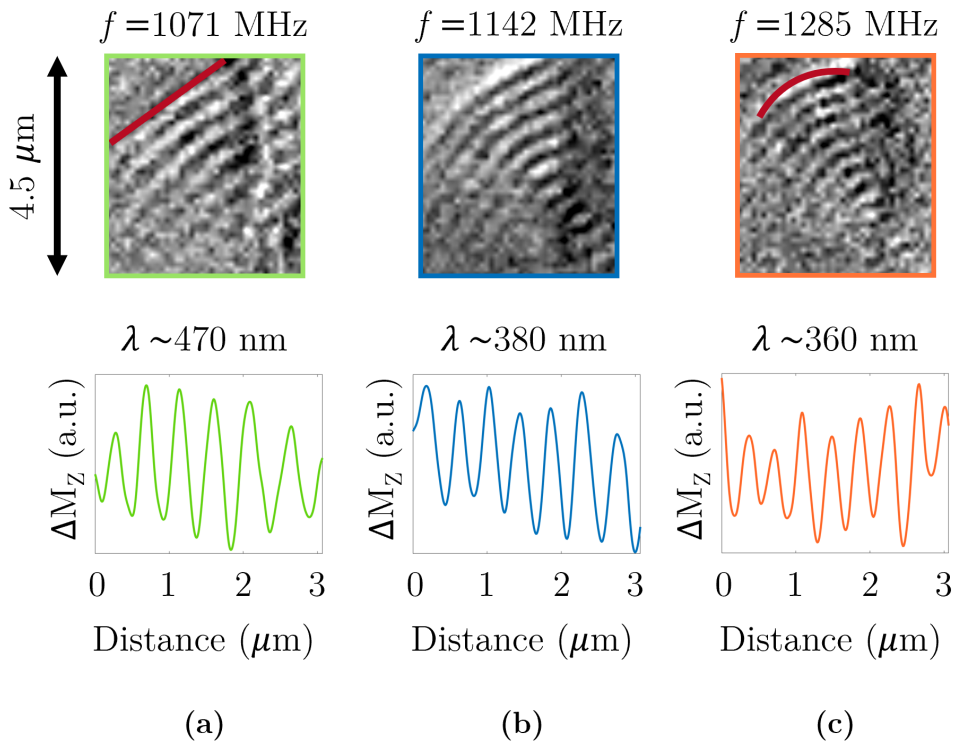


**Figure 4.11:** STXM (4×4.5) μm$^2$ images of a domain wall and the related emanating spin waves as a function of increasing excitation frequency $f_{RF}$. The bottom insets show the spin waves spatial amplitude evaluated for the same propagation length ~ 3 μm (the colour-map refers to diverse $f_{RF}$). By raising $f_{RF}$, the wavelength lowers and both the emitter and the corresponding wavefronts bend.

$f_{RF}$ = 1285 MHz, whereas the bottom ones show the corresponding spatial amplitude of the propagating spin waves. A preliminary observation, better discussed in what follows, can be derived by looking at the couple ($f_{RF}$; $\lambda$); especially, by raising the former, the latter is lowered (see the different number of peaks in the insets). Once again, this trend reveals the effective possibility of tuning the wavelengths by acting on $f_{RF}$. However, $\lambda$ is not the only parameter affected by $f_{RF}$. Noteworthy, the shape of either the emitter and the wavefronts significantly modifies by boosting the excitation frequencies. In fact, while for $f_{RF}$ = 1071 MHz the DW is a straight line and the waveforms are linear, by increasing the frequency, they both gradually bend till $f_{RF}$ = 1285 MHz, when a focusing action is achieved similar to the

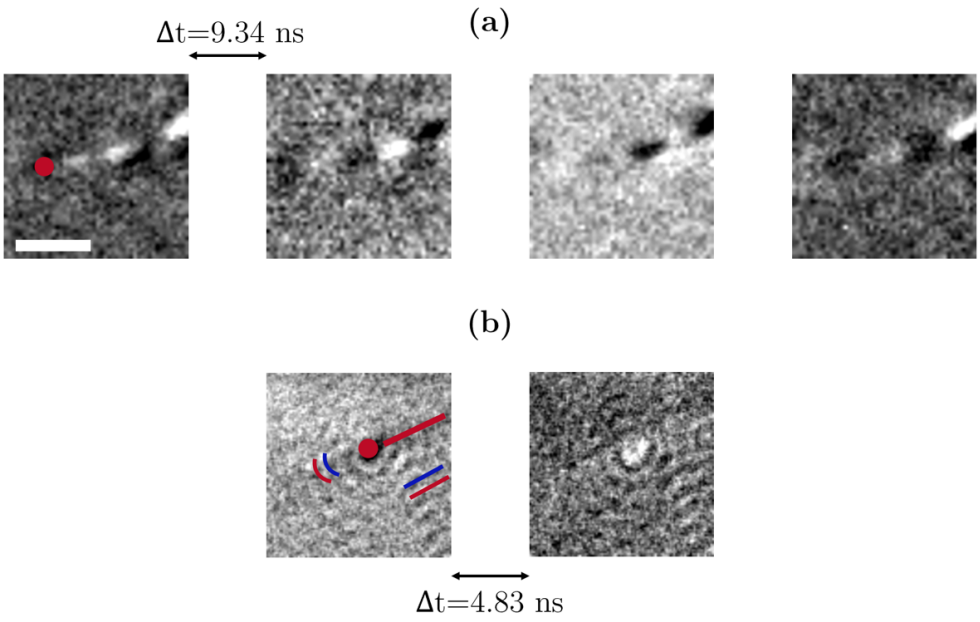


**Figure 4.12:** Extracted frames from STXM movies of the magnetization dynamics with an excitation frequency $f_{RF}$ = 428 MHz **(a)** and $f_{RF}$ = 2071 MHz **(b)**. Noteworthy, while in **(a)** the spin waves emitted from the vortex core propagate inside the domain wall, in **(b)** they are launched throughout the film by either the vortex and the domain wall. The magnetic contrast arises from the out-of-plane component of the magnetization. The scale bar is 1 µm for all the images.

one depicted in Fig. 4.10. An analogue 'bowing' has been observed with diverse $H_{st}$. Anyhow, the behaviour illustrated in figure can be ascribed to the frequency response of the DW to $f_{RF}$, which is not known a priori. To this purpose, another intriguing experimental evidence is documented in Fig. 4.12, where frames from the movie showing the excitation of a DW and a vortex at $f_{RF}$ = 428 MHz **(a)** and $f_{RF}$ = 2071 MHz **(b)** are reported. Remarkably, by changing $f_{RF}$ two distinct scenarios are now opened: on the one hand, for $f_{RF}$ = 428 MHz the vortex launches spin waves spatially confined inside the DW, consistently with the findings in [14], where a similar guiding effect was observed for comparable (low) excitation frequencies. On the other hand, at larger $f_{RF}$ (in the range of the ones typically adopted for the images reported so far) both the very same vortex core and the straight DW emit spin waves, and the corresponding modes propagate throughout the

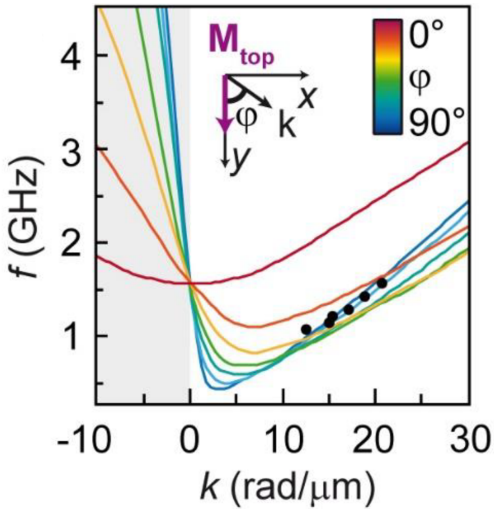


**Figure 4.13:** Simulated dispersion relations of spin waves in SAF as a function of the in-plane angle $\varphi$ between the magnetization of the top CoFeB layer (purple arrow along $y$) and the wavevector $\mathbf{k}$. $\varphi$ ranges from 0° to 90° (Damon-Eshbach configuration). The black filled dots coincide with the experimental data. The grey-shaded area for $k < 0$ corresponds to 'long-wavelength' modes, whereas the 'short-wavelength' modes stand on the right side (positive wavevectors). The simulation of the dispersion relations have been performed by S. Tacchi and R. Silvani of Dipartimento di Fisica e Geologia, Università di Perugia. The image is taken from [E. Albisetti et al., submitted to Science Advance].

film. Consequently, the opportunities of modulating either the wavefronts and wavelengths with $f_{RF}$, together with the one of arbitrarily confining the modes inside DWs, add extra flexibility to the described system, albeit further examinations are required to evaluate the reproducibility of features as those in Figs. 4.11–4.12.

To shed light on the above experimental observations, a deeper analysis on the underlying physics ruling the investigated heterostructures was accomplished. In this regard, Fig. 4.13 reports the calculated dispersion relation in SAFs as a function of the in-plane angle $\varphi$ between the wavevector $\mathbf{k}$ and the magnetization $\mathbf{M}$. To calculate the dispersion, micromagnetic simulations of the magnetization dynamics were carried out by solving the Landau–Lifshitz–Gilbert equation of motion, using the open-source, GPU-accelerated software MuMax$^3$. The simulated material parameters were set to the following values: saturation magnetization $M_S$ = 1000 kA/m, exchange

constant $A = 1.2 \cdot 10^{-11}$ J/m, interlayer exchange coupling constant $J = -0.6$ mJ/m$^2$. The Gilbert damping parameter was set to $\alpha = 0.001$. To compute the curves, the magnetization of the two CoFeB films was initialized to be pointing in opposite direction. Then, the relations were obtained by computing the response to a 10 mT sinc-pulse applied in the centre of the simulated area (a stripe 12.6 µm length, 40 nm wide and 2×45 nm thick, for the two CoFeB layer), with a maximum frequency component of 30 GHz. On the other hand, the experimental points (black dots in figure) are acquired by measuring the wavelength of propagating SW excited by a straight DW (see Fig. 4.7**(a)**) at different frequencies. First of all, the quite good agreement in Fig. 4.13 between the experiments and the derived dispersion relations corroborates the actual possibility of tuning the (nanometre) wavelengths by varying the excitation frequency. Besides, from figure it is also possible to see the strong non-reciprocity of the two branches for $k < 0$ and $k > 0$. As a matter of fact, this property straightly arises from the different group velocities $v_g \propto \partial\omega/\partial k$ of spin waves propagating in opposite directions ($\pm k$). Its implications are better clarified considering the dispersions for frequencies lower than the common cross-point $f_{cp} \approx 1.57$ GHz for $k = 0$. Indeed, if $f \leq f_{cp}$, the film sustains modes with only $k > 0$, theoretically confirming the experimentally observed 'one-way' propagation (see Fig. 4.10). On the contrary, for $f > f_{cp}$, two distinct modes are related to the same frequency, one for $k > 0$ and the other for $k < 0$. Especially, due to the slopes of the branches, all modes at negative $k$ have $v_g$ larger than the ones for the modes with $k > 0$. Accordingly, for a fixed frequency $f > f_{cp}$, the former are characterized with smaller $k$ compared to the wavevectors associated to the latter. Thus, since $k \propto 1/\lambda$, the modes for $k < 0$ correspond to spin waves with wavelengths greater than their counterpart for $k > 0$, and are so termed 'long-wavelength' modes; instead, those for positive $k$ are accordingly named 'short-wavelength' modes. The microwave frequencies $f_{RF}$ ($\leq f_{cp}$) exploited in the present work are mostly linked to the regime in which only 'short-wavelength' modes with $k > 0$ are supported by the SAF. As a consequence, the aforementioned 'forward' propagation and back-scattering immunity (discussed in Fig. 4.8) are assured. Furthermore, fixed $f = f_{RF}$, in

the 'short-wavelength' regime ($k > 0$) the similar behaviour of the dispersion relations makes wavelengths and group velocities to be the same for modes corresponding to distinct $\varphi$. In other words, 'short-wavelength' modes are characterized by a roughly isotropic in-plane propagation for a wide angular range (approximately from $\varphi = 90°$, dark blue curve, to $\varphi = 15°$, orange curve).

## 4.4 Conclusions and perspectives

In this chapter, the reported experimental measurements have confirmed the feasibility of efficaciously exploiting spin textures as emitters of spin waves with nanometre wavelengths. Starting from simple geometries, such as straight domain walls or vortexes, the spin waves propagation has been observed via Scanning Transmission X-rays Microscopy. The versatility of tam-SPL technique, together with the unique magnetic properties of thick exchange-biased Synthetic AntiFerromagnets, have allowed for both the spatially engineering of wavefronts (linear, radial, convex and concave) and micrometre travelled paths by spin waves. Moreover, the in-plane isotropic, 'one-way' propagation of the excited modes has granted for regular interference patterns, free from spurious contributions due to counter-propagating spin waves and/or back reflections by crystalline defects.
The present work lays the foundations to the effective use of spin waves as data carriers in future microwave signal processing devices, where the computation could be performed via analog interference of coherent wavefronts. In fact, the robustness of spin waves interference in SAFs, their nanometre wavelengths in the GHz regime, and the possibility of arbitrarily shaping their wavefronts via tam-SPL, pave the route towards the miniaturization of reconfigurable, spin-waves-based, optically-inspired platforms.

# Chapter 5

# One-dimensional magnonic crystals: the effects of a periodic DMI

## Overview

In the previous Chapter a promising alternative method to generate spin waves with nanometre wavelength has been experimentally proved. Especially, as already discussed, the use of synthetic antiferromagnets allowed for the unique non-reciprocity nature of the propagating modes. As a matter of fact, spin waves features can be tailored acting on several parameters, including the choice of magnetic material and the geometry and sizes of the patterned samples. In other words, in general it is possible to engineer the spectra of spin waves excitation by properly customizing their host support. In this regard, Magnonic Crystals are artificial magnetic media whose properties are characterized by a periodic variation in space [91]. Thanks to this periodicity, these metamaterials acquire a rich variety of features that are very diverse from those of their constituents. Indeed, any propagating spin wave probes effective parameters designed by structure and composition. Magnonic crystals therefore represent in spintronics the corrispective of photonic crystal in optics. Hence, they are per definition artificial materials where the periodicity needs to be comparable or smaller than the spin

waves wavelength of interest. Customarily, the modulation of the magnetic landscape reflects modifications in the thickness of the magnetic film [92], in its saturation magnetization [93], or in the width of the spin waves waveguides [94]. If the parameters are constant over time, these magnonic crystals are termed static, otherwise reconfigurable or dynamic. In the first case, depending on how a magnet is 'crafted' to form the resulting metamaterial, two distinct scenarios open: either one-dimensional (the focus of this chapter) or two-dimensional crystals (three-dimensional crystals are investigated theoretically [95]). Essentially, the former can be practically obtained by aligning parallel wires of dissimilar ferromagnets, while the latter result from a matrix of dots of various ferromagnetic materials.

The wave properties exhibited by such periodically patterned metamaterials resemble the ones in electronic band structures inside crystal lattices. In particular, a common thread shared from magnonic crystals consists in the presence of continuous bands, and in the opening of bandgaps in the spin wave spectrum at tunable GHz frequencies. As a consequence, magnonic crystals are one of the key elements for magnon spintronics, allowing the access to novel multifunctional devices for logic operations and signals processing [96].

Recently, a proposal for the implementation of a one-dimensional magnonic crystal with periodic Dzyaloshinsky-Moriya interaction (DMI) has been raised [9]. Indeed, the fabrication of magnetically ordered heterostructures hosting DMI is currently pursued with growing interest. The appeal for this kind of systems basically crops up from a double reason. On the one hand, DMIs stabilize chiral spin textures, such as skyrmions, future candidates as information carriers [47]; on the other hand, the antisymmetric nature of the Dzyaloshinsky-Moriya coupling enables non-reciprocal spin waves modes, particularly in thin ferromagnets adjacent to strong spin-orbit-coupling materials, such as heavy metals (HM) [50]. In this regard, a lot of theoretical work has been carried out in studying the interplay between spin waves and DMI, leading to several key aspects of the inspected systems. For instance, the non-reciprocal nature of spin waves in samples presenting DMI allows for a unidirectional propagation in a narrow frequency band in bicomponent

magnonic crystals in contact with a hevy metal layer [97]. Besides, it has been shown that, in principle, spin waves can be amplified at the boundaries between two regions having different DMI [98]. However, at the moment, the experimental realization of magnonic platforms exploiting DMI is still lacking. This can be mainly ascribed to the technical difficulties in fabricating devices with ferromagnetic active layers less than 1 nm thick, as required by the exploitation of DMI, which is an interfacial effect (see next paragraph). Oxidation, structural damage or interdiffusion arising from the fabrication processes can hinder the propagation of spin waves, that can be easily damped by the presence of defects. As will be explained later in this chapter, magnonic devices exploiting DMI have to be thoroughly designed, taking into account the lithographic steps necessary to fabricate them.

The second part of the present thesis work is the result of the collaboration with the theorists of [9] and the group of High-Resolution Optical Spectroscopy in Perugia. Therefore, it has drawn on the experimental realization of one-dimensional magnonic crystals, whose periodicity is signed by a variation in space of the interfacial Dzyaloshinsky-Moriya interaction. Especially, it has been predicted that the modulation of the DMI induces three major consequences on the magnonic band structure of ultrathin films: (*i*) low-frequency flat bands, (*ii*) tunable indirect band gaps, (*iii*) unconventional time evolution of the standing spin waves in the areas with active DMI. Due to the nanometre wavelengths of the propagating spin waves, which in turn request for similar features in the samples, the manufacturing of such devices was a challenging task, and has demanded severe optimization procedures. In order to prevent the thin ferromagnetic films from undergoing any lithographic process, a different approach from the theoretical work [9] has been proposed. We planned to localize DMIs by growing a thin ferromagnetic layer on top of a previously lithographed support. In fact, by alternating HM–$SiO_2$ stripes it is possible to spatially modulate the presence of the DMI, which arises only at the FM/HM interfaces (see Fig. 5.1).

In what follows, I report on each fabrication stage, namely the initial materials choice and stacks, the magnetic characterization of the related heterostructures, the electron-beam lithography of the specimens, and the

successive masks transfer to the substrates. Either the test and final samples were grown by magnetron sputtering on $Si/SiO_2$ substrates. The various steps were entirely carried out at PoliFAB, whereas the attached Brillouin Light Spectroscopy (BLS) measurements have been performed by S. Tacchi of Dipartimento di Fisica e Geologia, Università di Perugia. Lastly, the conclusive section of the chapter marks the comparison between the observed experimental outcomes and the predicted behaviour in [9].

## 5.1 Materials optimization

As already mentioned, the concrete development of the one-dimensional metamaterials of interest has necessarily implied an intermediate lithographic step. The reason of such a procedure is related to the conceived geometry for the devices, sketched in Fig. 5.1.

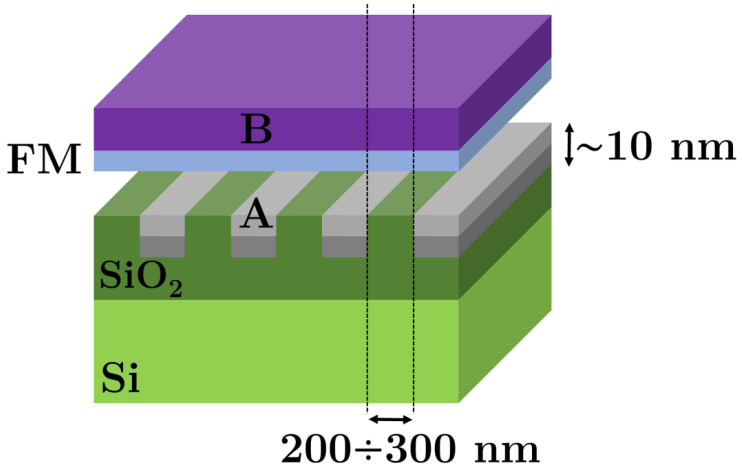


**Figure 5.1:** Schematic of the magnonic crystal structure used in the experiments. Starting from $Si–SiO_2$ substrates, a periodic array of trenches (hundreds of nanometres wide) was patterned via electron-beam lithography. Then, to modulate the DMI at the bottom surface of the ferromagnetic layer, the grooves were properly filled in order to expose alternated stripes of $SiO_2$ and a proper heavy metal (A). Both A/FM/B and $SiO_2$/FM/B stacks have previously been investigated by growing 1 $cm^2$ reference samples, to assess the optimal materials choice and the layers thickness.

As depicted in the above schematic, an array of grooves had to be patterned in the $SiO_2$ substrate, with the aim of subsequently filling them up with a suitable materials stack. Especially, to stabilize in the ferromagnetic layer a periodic landscape through a modulation of the interfacial DMI, the resulting support needed to alternatively expose stripes of $SiO_2$ and a proper heavy metal. Given the demanded feature sizes in [9] (hundreds of nanometers), an accurate design of the lithography has been requested, described in details later. The current paragraph deals instead with the materials choice and their corresponding magnetic behaviour.

The materials stacks addressed to promote DMI in the final magnonic crystals have been investigated to assess their specific properties by growing 1 $cm^2$ reference samples. In this regard, the optimal combination has resulted from several restrictions. First of all the inherent origin of the Dzyaloshinsky-Moriya interaction called for systems characterized by a broken space-inversion symmetry. Hence, a multilayer of the form A/FM/B was required, with A≠B and a strong spin-orbit-coupling heavy metal (HM), to assist the DMI via a three-site indirect exchange mechanism [49]. Once again CoFeB was selected as the ferromagnetic layer, since a large DMI constant $D$ [$mJ/m^2$] is highly anticipated due to its technological use for chiral domain wall motion [99] and formation of non trivial spin textures [100]. As a matter of fact, the interfacial nature of the investigated phenomenum makes the strength of the DMI to follow a $1/t_{FM}$ relation in the thickness of the FM [101], corroborating its surface provenance. Therefore, the designed heterostructures had to involve a thin CoFeB layer, in order to enhance the DMI signal and, consequently, the 'contrast' in the magnetic landscape at the bottom interfaces of the FM ($D = 0$ above the $SiO_2$ stripes in Fig. 5.1). However, the issue of such a constraint (i.e. small $t_{FM}$) concerned the stronger damping of spin waves compared to thicker ferromagnetic films. Nonetheless, a possible solution arose by thinking to Perpendicular Magnetic Anisotropy (PMA), properly tailored for the present context. PMA is a further interfacial effect observed in certain ultrathin ferromagnetic specimens, whose magnetization spontaneously orients perpendicularly to the surface, though the shape anisotropy would ideally force $\mathbf{M}$ to be in the sample plane. Concerning the

present work, a positive impact may occur in such a circumstance. Indeed, it has been reported that the spin waves lifetime greatly improves in CoFeB thin films exhibiting large PMA, wherein the damping is attenuated and spin waves can still be excited and propagate [102]. Moreover, the conditions for the achievement of PMA in thin CoFeB films have already been investigated, and they do not clash with the ones claimed by DMI. In fact, both the effects can be pursued in systems comprehending a CoFeB layer sandwiched in between a heavy metal, as Ta or Pt, and MgO [103, 104]. In such structures, the origin of PMA seems to reside in the interface interaction among Co, Fe and O atoms, which bends the easy axis from in plane to out of plane. The presence of the beneath HM appears to facilitate and strenghten the PMA, though a different picture arises passing from Ta to Pt. In particular, while samples with Ta underlayers present clear PMA, those with Pt show a more in-plane-like magnetic anisotropy [105]. Thus, two main possibilities opened for the stack determining the regions with active DMI inside the magnonic crystal: either Ta/CoFeB/MgO or Pt/CoFeB/MgO. The choice, among the two, favoured the latter for several reasons. Firstly, Ta is known for creating a considerable magnetic dead layer ($\sim 0.4$ nm) when placed next to CoFeB [106], which in turn significantly worsen its saturation magnetization (here the effect is even exacerbated due to the desirable small $t_{FM}$). Besides, past studies have revealed that the DMI is much greater at Pt/CoFe interface than that at Ta/CoFe [107] (and it is licit to expect a similar behaviour also for CoFeB). Further, the discussed different impact of Ta and Pt respect to PMA made Pt the optimal alternative in view of the subsequent BLS measurements (see below); finally, in ultrathin Pt/CoFeB films the dependence of the induced interfacial DMI on the Pt thickness $t_{Pt}$ is well known, displaying a monotonic trend of $D$ respect to $t_{Pt}$ till a plateau for $t_{Pt} \sim 2$nm [50].

Yet, a recent work has shown a favourable action for the DMI in growing a multilayer constituted of Ta/Pt/CoFeB/MgO, where Ta was used as seed layer for Pt [108] (the importance of separating the substrate from the upper materials will become even more evident later, dealing with the $SiO_2$/CoFeB interface). Especially, with $t_{Ta}$ = 5nm and $t_{FM}$ = 1nm, the effective parameter $D$ has been observed to adapt with $t_{Pt}$, and to satu-

rate, for $t_{Pt} \sim 4$ nm, to a higher value compared to the one without the Ta buffer layer [50]. Accordingly, the initial investigated heterostructure was Si–$SiO_2$/Ta(5)/Pt(5)/CoFeB($t_{FM}$)/MgO(5) (number in parenthesis are the nominal thicknesses in nm). In these systems, the Ta seed layer eases the adhesion of the stacks and decouples them from the below $SiO_2$, the Pt bottom layer induces PMA and DMI in the CoFeB layer, whereas the MgO is essential to provide an asymmetric interface to the CoFeB, promote PMA and it prevents the FM from oxidation. Only the thickness $t_{FM}$ of the CoFeB layer was varied, while keeping all the other parameters fixed, in order to optimize the interfacial DMI strength and analyse the emerging of PMA.

From the aforementioned arguments, apparently the smaller is $t_{FM}$, the better (larger) is the value of $D$ (due to the interfacial nature of DMI). Hence, thickening the layer too much would be useless in establishing a contrast between regions of active DMI and zones where the FM was directly grown atop $SiO_2$ (see Fig. 5.1). On the other hand, an exaggerated scaling in the size of the CoFeB film would be counterproductive either, for two main reasons. Firstly, under a specific threshold of the CoFeB grains dimensions, a transition in the FM occurs towards the superparamagnetic state [109]. The second reason is mainly technical, because we wanted to be able to saturate the magnetization in the plane of the sample during the BLS characterization (see below). To do so, we were limited by the setup to apply an external field of 2 kOe maximum. At low film thicknesses, even in the ferromagnetic regime, the strong PMA would prevent a complete in plane saturation. Consequently, on the basis of data and reports available in the literature [50, 104, 108], as well as on past experience within the research group, the range explored for $t_{FM}$ encompassed thicknesses from 0.7 to 1 nm.

The materials stacks were grown by magnetron sputtering on Si–$SiO_2$ substrates with the conditions listed in Table 5.1. Differently from the case of the exchange-biased synthetic antiferromagnets discussed in Chapter 4, this time no magnetic field was applied during the deposition. Later, the samples were characterized by VSM 'as grown' and after an annealing of 30 minutes at 470 °C in a 4 kOe field applied perpendicular to the sample surface. In-plane and out-of-plane hysteresis loops were separately recorded,

| Material | Mode | Ar pressure | Power | Rate |
|---|---|---|---|---|
| - | - | mTorr | W | nm/min |
| $Co_{40}Fe_{40}B_{20}$ | DC | 3.5 | 58 | 1.35 |
| Pt | DC | 5 | 10 | 2.7 |
| Ta | DC | 3 | 100 | 5.1 |
| MgO | AC | 2.2 | 220 | 0.33 |

**Table 5.1:** Magnetron sputtering deposition conditions for the one-dimensional magnonic crystals with a periodic interfacial DMI.

allowing the identification of the type of anisotropy and the in-plane saturation field. Fig. 5.2 shows the results for the specimens with the minimum and maximum $t_{FM}$, acquired after the annealing procedure, since the last little affected both their shapes and the magnetization absolute values. As sketched, the upper couple refers to the case $t_{FM}$ = 0.7 nm, whereas the bottom to $t_{FM}$ = 1 nm. For a better comparison, the same colour-map is exploited in each panel, namely the red graphs (on the left) are those corresponding to the in-plane hysteresis loops, and the ones (on the right) are related to the out-of-plane component. Noteworthy, by diminishing $t_{FM}$ from $t_{FM}$ = 1 nm to $t_{FM}$ = 0.7 nm, the shape of the out-of-plane loop is significantly altered. Indeed, while in the former condition it evidently pertains to an hard axis (being elongated and reaching the saturation for fields out-of-scale), in the latter it much more resembles the behaviour for an easy-axis. In particular, for $t_{FM}$ = 0.7 nm, albeit the measurements are noisy, the in-plane and out-of-plane hysteresis loops are similar, suggesting the presence of a perpendicular magnetic anisotropy. Fig. 5.2 also reveals that the in-plane saturation field, for both $t_{FM}$ = 0.7 nm and $t_{FM}$ = 1 nm, fulfils the necessary constraint to carry out the subsequent BLS experiments ($H_{sat} < 2$ kOe). Furthermore, from the measurements the magnitude of the magnetization saturation has been evaluated to be $1.2 \times 10^6$ A/m and $0.8 \times 10^6$ A/m, respectively for the thickest and thinnest CoFeB film. While the first number is within a similar range in literature [99, 104], the second is slightly under the average. A possible explanation resides on the fact that our estimate of $M_S$ relies on the volume of magnetic material present in the sample. An

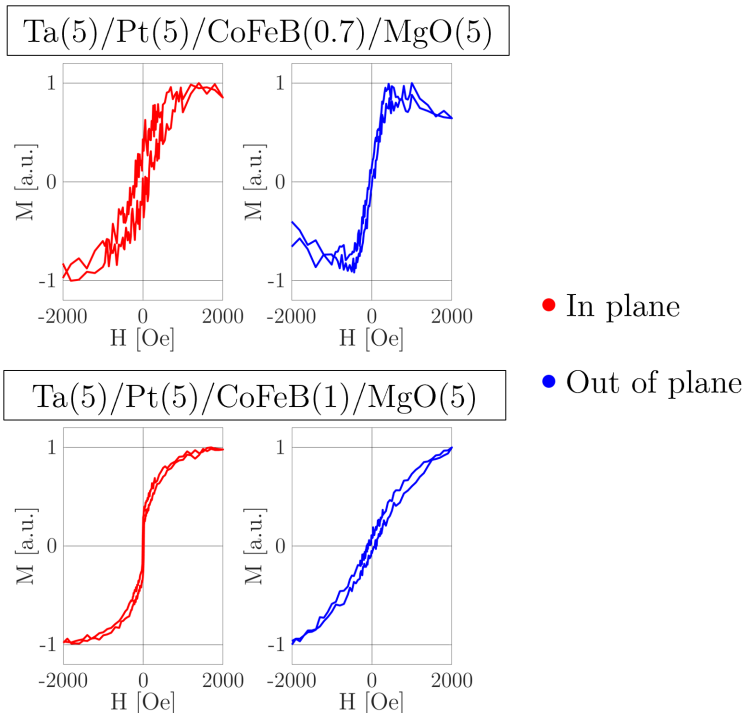


**Figure 5.2:** In-plane (red curves) and out-of-plane (blue curves) hysteresis loops after annealing at 470 °C for $t_{FM}$ = 0.7 nm (upper panel) and $t_{FM}$ = 1 nm (bottom panel) of heterostructures comprising Ta(5)/Pt(5)/CoFeB($t_{FM}$)/MgO(5). Remarkably, whereas for $t_{FM}$ = 1 nm the out-of-plane direction is clearly an hard axis for the specimen, thinning the CoFeB to $t_{FM}$ = 0.7 nm, the resulting magnetic landscape is more undefined (the two plots for $t_{FM}$ = 0.7 nm show a similar behaviour). The worsening of the signal-to-noise ratio for the thinnest CoFeB layer is due to the lower amount of magnetic material. For the same CoFeB thickness $t_{FM}$, the deformation of the loops at high fields has to be attributed to the non-perfect subtraction of the background diamagnetic contribution of the sample-holder.

underestimation of $M_S$ can arise if the effective thickness of the magnetic film is lower than the nominal one. Especially, a credible justification for the last consists in the development of a thin magnetic dead layer induced by the beneath Pt, whose effect is more pronounced for the smallest $t_{FM}$. The assumption sounds reasonable since the formation of the (001) texture in the MgO surface, which is the most close-packed plane, makes the intermixing at CoFeB/MgO improbable, and therefore prevent the formation of a dead layer at that interface [106].

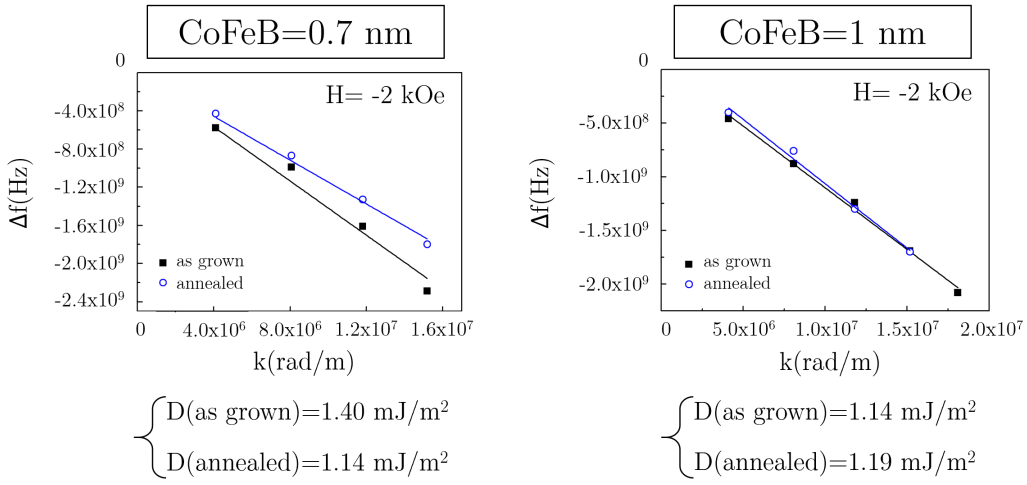


**Figure 5.3:** BLS measurements acquired with an in-plane magnetic field $H = -2$ kOe for $t_{FM} = 0.7$ nm (panel on the left) and $t_{FM} = 1$ nm (panel on the right). The experimental points are reported either before and after the thermal treatment at 470 °C together with the linear fitting lines, from which it was possible to extract the values of $D$. Especially, whereas for $t_{FM} = 1$ nm the annealing procedure does not essentially alter the interfacial DMI, the last is worsened after the annealing for $t_{FM} = 0.7$ nm.

The two samples reported so far were both suitable candidates for the fabrication of the DMI-based one-dimensional magnonic crystals. Hence, the characterization of the DMI in both samples was performed through BLS spectra. Fig. 5.3 illustrates the outcomes of BLS measurements for $t_{FM} = 0.7$ nm and $t_{FM} = 1$ nm. Differently from the experiments discussed in Chapter 4, these preliminary measures were carried out without the use of patterned antennas to generate spin-waves. Thermally excited spin-waves are therefore studied at room temperature in order to evaluate the anisotropies of the samples and the modes sustained by the magnonic crystal (see Paragraph 5.3), without focusing on the propagation of these waves. To better understand the plots in figure, a preparatory discussion is demanded. BLS experiments have been performed within a Damon-Eshbach (DE) geometry, where the magnetization of the specimens was saturated in-plane by an ex-

ternal applied field. In such an arrangement, spin waves can be localized at the top and bottom surfaces of the ferromagnetic layer depending on their wavevector $\pm k$ respect with the magnetization, which lays perpendicular to both $k$ (see Chapter 2). In this configuration, BLS is exploited to observe non-reciprocal spin wave dispersion relations affected by interfacial DMI. Indeed, the technique measures the propagating spin waves simultaneously at the two interfaces (CoFeB/Pt and CoFeB/MgO). The wavevector of the spin wave mode is uniquely defined by the wavelength and the scattering angle of the incident laser light. In the inelastic events, the photons can either lose their kinetic energy (Stokes process) in the interaction with a spin wave with wavevector $+k$, or gain energy (anti-Stokes process), in the interaction with a $-k$ mode. Usually, in ferromagnetic films with the same surface anisotropy at the top and bottom interfaces, the spin waves frequencies of Stokes and anti-Stokes peaks should be nearly at the same position with respect to the elastic peak. However, in presence of DMI, due to the different anisotropies at the two sides of the film, there is a difference in the frequencies of the DE modes travelling at the two interfaces with opposite wavevectors. In Fig. 5.3 the frequency difference $\Delta f$ on the ordinate axes exactly indicates the mismatch between the Stokes and anti-Stokes frequencies peaks. Indeed, the DE spin waves frequencies, including interfacial DMI, read as:

$$f_{DE} = f_0 \pm C\frac{D}{M_S}k \tag{5.1}$$

where $f_0$ is the spin wave frequency without DMI, $M_S$ is the saturation magnetization of the ferromagnet, $D$ is an effective parameter (positive or negative) standing for the DMI, and $\pm$ sign is related to $+k$ (Stokes peak) or $-k$ (anti-Stokes peak) wavevector. Therefore, for $D \neq 0$, $\Delta f = f_{DE}(+k) - f_{DE}(-k) \propto (D/M_S)\,k$, justifying the linear trend of the plots (with, in either the cases, $D < 0$). The experimental points in figure, referring to the specimens as grown (black squares) and annealed (empty blue circles), have been fitted with the coloured straight lines, reported as well, to infer the related slopes. Consequently, knowing from the VSM data the magnitude of $M_S$, it has been possible to extract the absolute value for $D$, which quantitatively

agrees with the literature [104] for similar systems. As expected from the initial discussion, $D$ increases by thinning the ferromagnetic layer, confirming the interfacial origin of the DMI. In fact, the maximum $D = 1.4$ mJ/m$^2$ is attained for $t_{FM} = 0.7$ nm, whereas $D$ slightly diminishes for $t_{FM} = 1$ nm. Moreover, the graphs reveal another important information, i.e. the influence of the thermal treatment. To this purpose, even though the magnetic signals measured through VSM were essentially unaffected by the annealing procedure, the last has negatively impacted on the interfacial DMI for $t_{FM} = 0.7$ nm (while for $t_{FM} = 1$ nm, $D$ is basically unchanged). Such a behaviour can possibly be attributed once again to the intermixing at the CoFeB interfaces, promoted by the annealing, whose consequences are more evident for smaller $t_{FM}$. Anyhow, to avoid a potential worsening of the DMI, the samples no longer underwent the heating operation.

From the evidences described in Fig. 5.3, the value of DMI found made both film thicknesses suitable for the fabrication of the magnonic crystal. Starting from these results, the samples with $SiO_2$/CoFeB/MgO structures have been characterized, in order to access the magnetic properties of the second component of the crystal. At this stage, to be sure to have a good VSM magnetic signal, we started with the characterization of a bilayer of CoFeB(1)/MgO(5) atop of 1 cm$^2$ thermally oxidized silicon substrate. Especially, the samples were grown to assess the magnitude of the magnetization saturation and perpendicular anisotropy, which ideally needed to be uniform over all the ferromagnet (both above the Pt and the $SiO_2$ stripes). Indeed, the modulation of the magnetic landscape inside the one-dimensional magnonic crystals in [9] crops up uniquely due the variation of the DMI passing from one region to the nearby. Nevertheless, the results of the in-plane VSM measurements for the stack Si-$SiO_2$/CoFeB(1)/MgO(5) have pointed out a saturation magnetization little bigger than the diamagnetic background of the sample-holder (i.e. definitely minor than $M_S$ for Ta/Pt/CoFeB/MgO). The causes of the experimentally observed behaviour can be mainly ascribed to an oxidation mechanism triggered by the beneath silicon oxide $SiO_2$. In fact, the insurgence of dead layers of about $\sim 0.7$ nm thick, due to the interdiffusion of nonmagnetic atoms, has been already reported in ultrathin CoFeB

films on $SiO_2$ substrates [110]. The degradation of the magnetic signal was so linked to the similar thicknesses of both the ferromagnetic and the magnetic dead layer. Hence, among the sputtering targets at our disposal, the only two suitable to decouple CoFeB from $SiO_2$ in these circumstances, were Ru and MgO. The choice of the two materials was motivate by the fact that Ru is not a heavy metal and we expect it to provide zero or very low DMI; on the other hand, MgO assures a negligible intermixing at the interface with CoFeB and completely symmetric interfaces (therefore $D \equiv 0$). Anyhow, given the monotonic increasing trend of $D$ with the thickness of Pt $t_{Pt}$ for Pt/CoFeB systems [50], to be sure to limit a potential DMI arising from Ru, the guide line consisted in setting $t_{Ru}$ and $t_{MgO}$ as low as possible. Besides, in so doing, the developed lithographic processes (discussed in the next paragraph) would not have been substantially altered. Thus, $SiO_2$/Ru(1)/CoFeB(1)/MgO(5) and $SiO_2$/MgO(1)/CoFeB(1)/MgO(5) stacks were separately deposited. The corresponding in-plane hysteresis loops are shown in Fig. 5.4, together with the one for $SiO_2$/CoFeB(1)/MgO(5) for a comparison.

As sketched in the left panel, when the CoFeB film is split from the $SiO_2$ substrate by means of either 1 nm thick Ru (blue curve) and MgO (green curve) layer, the measured signal improves. However, the inferred value for $M_S$ is by far lower (about one order of magnitude) respect to the case of Ta(5)/Pt(5) as underlayers. Moreover, the three loops are all narrow, and none of them exhibits a meaningful remanence magnetization in zero-applied field. Likely, the trends suggest that the CoFeB film becomes granular in nature, with a superparamagnetic behaviour. The last could agree with [110], where ultrathin CoFeB layers ($t_{FM} \lesssim 1$ nm) grown atop of MgO supports, turn into separate grains with no stable ferromagnetic moment. In the case of Ru(1)/CoFeB(1) the low magnetic signal and the approximately superparamagnetic behaviour can be ascribed to a granular growth of the thin Ru layer, which leaves partially uncovered the underlying $SiO_2$. As a matter of fact, by increasing the Ruthenium thickness to 3 nm it has been possible to efficaciously decouple the ferromagnetic layer from the substrate, as illustrated in panel **(b)** of Fig. 5.4. The hysteresis loop displays a definite ferromagnetic behaviour (the remanence magnetization is clearly different

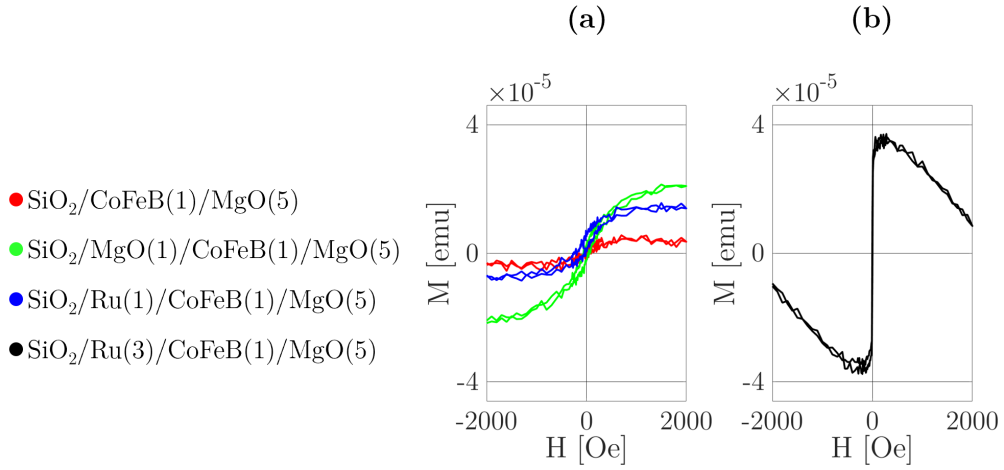


**Figure 5.4:** In-plane hysteresis loops for various material stacks. In **(a)** the insertion of 1 nm thick buffered layer of either MgO (green curve) and Ru (blue curve) betters the magnetic signal compared to the case of $SiO_2$/CoFeB(1)/MgO(5) (red curve). However, the shape of the plots may suggest a transition toward the CoFeB superparamagnetic state (see main text). In **(b)** is reported the trend for $SiO_2$/Ru(3)/CoFeB(1)/MgO(5), which shows a clear ferromagnetic behaviour, with $M_S$ nearly one-third of the value for $t_{FM}$ = 1 nm in Fig. 5.2.

from zero and the cycle is squared, though the deformations at high fields due to the subtraction of the background), with $M_S$ roughly one-third of the value related to the Ta(5)/Pt(5)/CoFeB(1)/MgO(5) stack. Due to the difficulties in achieving a reliable and stable magnetic behaviour similar to that obtained with Pt/CoFeB, a thickness of CoFeB of 1 nm instead of 0.7 nm has been chosen for the realization of the one-dimensional magnonic crystal. This pick has been made thanks to the promising results of Fig. 5.3, in which a sizeable DMI is measured even with 1 nm of CoFeB.

Accordingly, a preparatory BLS spectrum has been acquired also for this case of Ru(3)/CoFeB(1)/MgO(5), and the related outcomes are sketched in Figure 5.5. Unexpectedly, a value for $D \sim 0.17 \neq 0$ mJ/m$^2$ has been found. A similar result for Ruthenium is new in literature, and in principle negatively impacts the behaviour of the designed devices. However, $D$ is around one order of magnitude smaller than the one for Pt(5)/CoFeB(1)/MgO(5), thus allowing anyway a good contrast in terms of DMI among Ru and

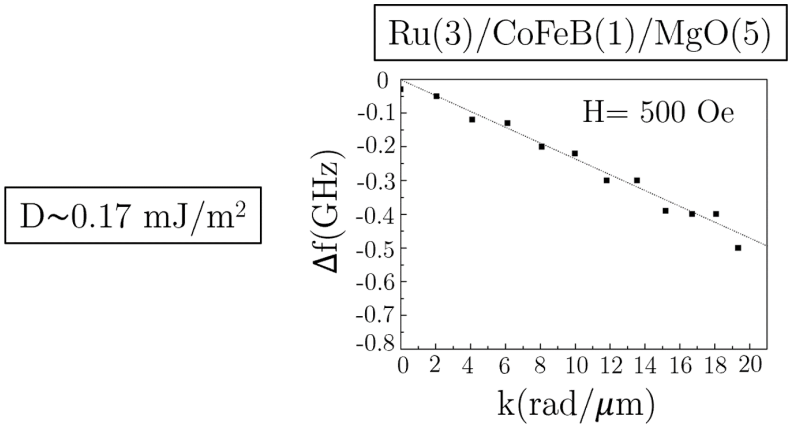


**Figure 5.5:** BLS measurements acquired with an in-plane magnetic field $H$ = 500 Oe for Ru(3)/CoFeB(1)/MgO(5). An unpredictable, though very small, value for the DMI has been observed.

Pt stripes. Hence, it is legitimate to foresee secondary effects at most, which do not invalidate the theoretical predictions in [9]. As a consequence, Ta(5)/Pt(5)/CoFeB(1)/MgO(5) and $SiO_2$/Ru(3)/CoFeB(1)/MgO(5) stacks were chosen for the regions with and without DMI, respectively.

## 5.2 Fabrication process

As sketched in Fig. 5.1, the major criticalities of the fabrication procedure were essentially two. Firstly, the (high) aspect ratio of the features to be lithographed atop $SiO_2$, namely 200 nm × 600 µm, dictated by the spot-size $w_l$ of the laser adopted (~ 200 µm) for the acquisition of the subsequent BLS spectra. Indeed, though a patterned region extending on an area of $w_l^2$ might be in principle fine, the dimensions of the mask were enlarged to 600 µm$^2$. This number was picked to account for the increased projection of the spot-size at the different incident geometries of the laser during the angle-resolved BLS measures, in order to facilitate the alignment. Secondly, the need of an ideally flat support surface for the CoFeB deposition, which in turn has demanded an accurate calibration in filling the etched lithographed structures.

Therefore, to obtain the magnonic crystal in Fig. 5.1, the following steps have been optimized and pursued sequentially:

- an array of parallel lines was firstly exposed via electron-beam lithography on the substrate, earlier coated by a suitable resist. The lateral size of the lines had to be equal to their grating pitch, both of hundreds of nanometers, as discussed in [9];
- after the resist development, the mask was transferred by physically etching the substrate; the depth of the corresponding trenches needed to be as close as possible to 10 nm, to house 5 nm of Ta and 5 nm of Pt, as said before;
- later, Ta(5)/Pt(5) stack was deposited to actually fill the grooves; instead, the residual resist on the adjacent regions has prevented them to be covered by the sputtered Ta and Pt atoms. The subsequent lift-off procedure has resulted in a surface formed of alternated Pt and $SiO_2$ stripes;
- finally, 1 nm of CoFeB and 5 nm of MgO were grown on such a support; this way, a periodic magnetic landscape has been engineered at the bottom CoFeB interfaces, which either show or not DMI.

The optimization of the lithographic process was carried out on standard Si–$SiO_2$ specimens. The same findings have then successfully transferred also for the Si–$SiO_2$/Ru(3) substrates.

In virtue of the aforementioned dimensions of the pattern of interest, electron-beam lithography (EBL) has been employed, thanks to its ability to write arbitrary two-dimensional structures down to the nanometre resolution. In spite of the simplicity of the used mask (prepared with AutoCAD), consisting of an array of parallel lines, plenty of parameters have been tailored to generate the desired output. As a matter of fact, the major issue has resided in the huge lithographic region arisen from the above BLS constraints. Consequently, the resulting high aspect ratio of the features has required, at the same time, a resolution down to the nm, and a writing-field area up to

several hundreds of microns. However, the two quantities (theoretical resolution, namely the minimum achievable step-size $\Delta$, and writing-field area) are inherently interrelated in the exploited SEM-modified machine: the larger is the latter, the worse is the former. Especially, for the adopted writing-field area of 1000 µm$^2$, $\Delta \sim 20$ nm, not so far from the lateral dimension of the stripes to be patterned. Thus, to match the geometry of [9], all the main lithographic steps were individually addressed. In this regard, the key determinants were the choice of the resist and developer, and the process conditions, particularly the electron beam energy and dose, the baking temperature and its timing, as well as the one for the development.

Due to the long times taken from each run, wich is basically the primary disadvantage of EBL compared to optical lithography, preliminary trials were accomplished by writing just few lines. Moreover, because of the great sensitivity to vibrations of the instrument, the final scans were performed at night. On the basis of past experiences, the lens aperture was fixed to 10 µm (the smallest at our disposal), and the accelerating voltage $V$ to 20 kV (the largest at our disposal). The former let a tiny focus spot be produced on the resist, and the latter enlarged the applicable doses window (typical values range between 200 and 400 $\mu$C/cm$^2$). Especially, the reason for $V$ = 20 kV is that electrons with higher energies are subjected to less forward scattering, and as a result, the beam broadens less [111]. Besides, such accelerated electrons penetrate deeper into the substrate, eventually arriving to the conductive silicon beneath; hence, charging effects were expected to be less severe than at low voltages [111]. In these circumstances, the beam current has always remained nearly constant and equal to $\sim 24 - 25$ pA.

Initially, thin 950K PMMA films (circa 200 nm thick) were spin-coated onto the samples at 4000 rpm for 1 minute. Then, two distinct baking procedures have been separately followed to assess the optimum one: on the base of past experiences, some specimens were baked at 180 °C for 180 s, whereas others at 175 °C for 5 minutes, as in [112]. The same mask, constituted of 10 lines nominally 200 nm wide with 400 nm pitch, was patterned in either the cases, by spanning the dose from 230 $\mu$C/cm$^2$ to 250 $\mu$C/cm$^2$ in step of 10 $\mu$C/cm$^2$. Lastly, the exposed zones were developed at room temperature

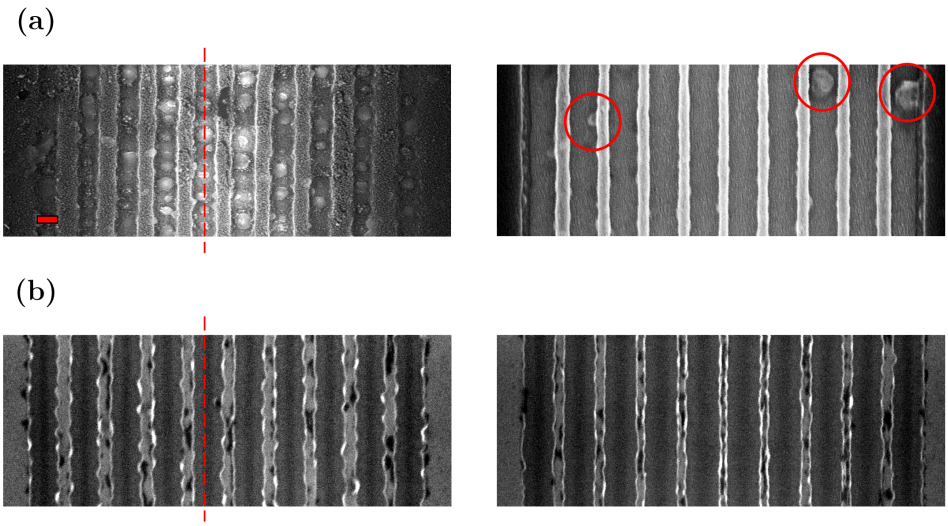


**Figure 5.6:** SEM images of 200 nm gratings in a 950K PMMA layer on Si–$SiO_2$ substrates with 20 keV exposure at 230 $\mu C/cm^2$ (figures on the left) and 250 $\mu C/cm^2$ (figures on the right). In **(a)** the sample were baked at 180 °C for 180 s, while in **(b)** at 175 °C for 5 minutes. The red dashed lines trace the dissolved grooves in the resist. Noteworthy, the red encircled unwanted features in the upper-right panel. The scale bar is the same for all the acquired pictures, and corresponds to 200 nm.

for $\Delta T_1$ = 30 s in a MBIK:IPA (1:3) solution, with a consecutive rinse for $\Delta T_2$ = 30 s in pure isopropyl alcohol. Fig 5.6 illustrates the resulting SEM images of exemplary surfaces for the two dose extremes after the development (the row on the left (right) stands for a dose of 230 $\mu C/cm^2$ (250 $\mu C/cm^2$), respectively). In more detail, the top figures correspond to a baking time of 180 s at 180 °C, while the bottom ones to the other baking process (5 minutes at 175 °C). Though the influence of the diverse annealing is not straightly highlighted in the figure, a general improvement in the edges was experimentally observed with the second thermal treatment. Besides, the latter also let the unwanted features encircled in the upper-right panel be removed, whose origin did not seem to depend neither on the dose nor on the development. Therefore, from now on, it is implicitly assumed for all the next processes. On the contrary, in both **(a)** and **(b)** it is quite evident that

the greater is the dose, the better are the results (in terms of sharpness of the edges). However, *proximity effects* at higher doses are evident, resulting in an enlargement of the feature size (width of the dissolved stripes). Indeed, high energy electrons entering the resist in a specific position $x$ travel longer paths, and are so more susceptible to backscattering events. Upon these large-angle collisions, a fraction of the charged particles will re-emerge from the resist at some distance from $x$. Thus, backscattered electrons may cause exposure of nearby non-exposed regions [113]. This effect has to be added to the large step size $\Delta$ imposed by the writing-field area.

Consequently, in successive optimizations the doses were increased and the mask was accordingly altered. In particular, whereas their nominal wide was left to 200 nm, the gap between adjacent lines was incremented to 400 nm (total pitch equal to 600 nm). In addition, to achieve sharp and evenly spaced features, also the development times were raised up to 40 s. Finally, for the same listed process conditions (baking, mask, doses and development), better results were attained by modifying the employed resist. In this regard, Fig. 5.7 shows SEM images of gratings fabricated in 200K PMMA resist, which has a less molecular weight and it is more sensitive.

In panel **(a)**, again the two extrema of a series of tests at different doses have been acquired after the resist development (as before, the dose separation has been varied in steps of 10 $\mu$C/cm$^2$). Especially, the picture on the left corresponds to a 275 $\mu$C/cm$^2$ area dose, while the one on the right to 325 $\mu$C/cm$^2$. At a first glance, it is already undeniable a general improvement of the surface appearance with respect to Fig. 5.6, verifing the aforementioned arguments. Nevertheless, an additional clue can be caught from the dissimilarities in the two panels. In fact, while the trenches on the left (white patterns) appear slightly underexposed, the ones on the right are quality structures. Supplementary researches at higher doses have confirmed an optimal value of 325 $\mu$C/cm$^2$, since no further enhancements were obtained. Yet, the feature sizes in Fig. 5.7**(a)** were still a bit too large compared to the ones theoretically examined in [9]. Besides, another issue to address was found to be the spin coating. The huge dimensions of the patterned area, demanded a continuous resist film with a uniform thickness atop vast zones

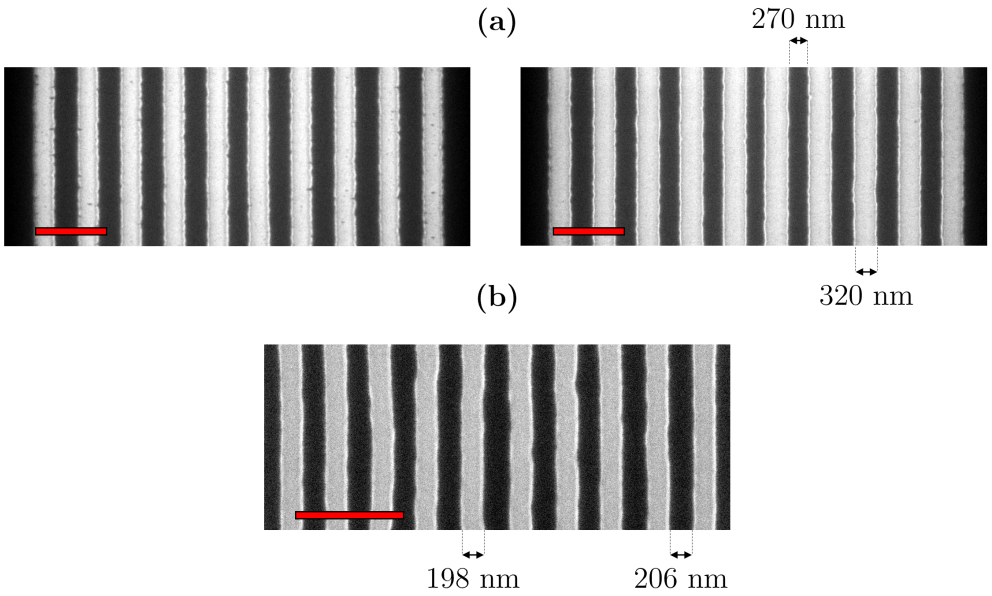


**Figure 5.7:** SEM images of patterns in 200K PMMA layer on Si–$SiO_2$ **(a)** and Si–$SiO_2$/Ru(3) **(b)** substrates. In **(a)** the nominal width ($W$) of the lines amounted to 200 nm, while the grating pitch ($P$) to 400 nm. The doses are 275 $\mu$C/cm$^2$ and 325 $\mu$C/cm$^2$ for the picture on the left and right, respectively. In **(b)** the dose was fixed to the optimal value of 325 $\mu$C/cm$^2$, with $W$ = 150 nm, $P$ = 300 nm, and an increased spin velocity of 5000 rpm. The scale bars correspond to 1 µm.

of the specimens. As a matter of fact, it has been experimentally disclosed that inhomogeneities of such a coating layer in turn locally degraded the outcomes. Thereupon, both to enhance the reproducibility and to diminish the leverage of this parameter, it has been decided to boost the spin velocity $v_s$. Since the resist thickness was nearly saturated already at $v_s$ = 4000 rpm, bringing $v_s$ = 5000 rpm has allowed to achieve a homogeneous coating everywhere atop the specimens, without affecting the resist thickness on the write-field area, so that the dose and patterning parameters have remained unchanged. Hence, before passing to the Si–$SiO_2$/Ru(3) substrates, $v_s$ has increased to 5000 rpm, and the nominal width ($W$) and pitch ($P$) of the designed mask have been brought to 150 and 300 nm, respectively.

The final step of the optimized procedure is displayed in panel **(b)** of Fig. 5.7 for Si–$SiO_2$/Ru(3) specimens. Specifically, the image corresponds just to

a portion of the patterned array of lines from an entirely patterned sample (600×600 µm$^2$ of area). As reported in **(b)**, a periodic grating of trenches with a period of about 200 nm has been ultimately produced. Moreover, the 3 nm thick Ru buffered film did not significantly affect the lithography, as expected. On the contrary, it is licit to assume the positive results illustrated in figure to be partially favoured by the presence of the conductive Ruthenium, which would have mitigate charging effects. Table 5.2 summarizes the conditions fulfilled for the amended lithographic process.

| **Baking** | | **Development** | | **Dose** | **Coating** | | **Sizes** | |
|---|---|---|---|---|---|---|---|---|
| $\Delta T$ [min] | T[°C] | $\Delta T_1$ [s] | $\Delta T_2$ [s] | $\mu$C/cm$^2$ | $\Delta T$ [s] | $v_s$ [rpm] | $W$ [nm] | $P$ [nm] |
| 5 | 175 | 40 | 40 | 325 | 60 | 5000 | 150 | 300 |

**Table 5.2:** Optimized parameters for the electron-beam lithography. The notation is the same adopted in the main text.

After the optimization of the electron beam lithography, the mask had to be transferred on the substrate. To accomplish this task, we have employed the ion beam milling technique, described in detail in Chapter 3. The major effort has resided in carving away the proper amount of material, in order to obtain stripes with controlled deepness, namely in the sub−nm range. Indeed, the engineered outer surface of the supports, where the CoFeB layer had to be later deposited, needed to be as much as possible orderly and flat. Therefore, firstly the exact assessment of the etching rates of interest (the ones for $SiO_2$ and Ru) has been required. The goal was carried out by means of successive stages. A preparatory appraisal of the etching rates was evaluated by growing specific test specimens and by measuring on them, after the etching, the depth of previously patterned 'macroscopic' features. In other words, the substrates were partially covered during the milling performed at fixed times, and then AFM profiles among adjacent regions, either exposed or not, were measured to esteem the height of the etched material. The tilt angle $\theta$ between the incident charged particles and the sample-holder was priorly fixed to 30°, on the basis of past experiences, to avoid redeposition. Thus, the rates attained so far have been used for subsequent calibrations with test samples coming from the lithography optimization. The reason

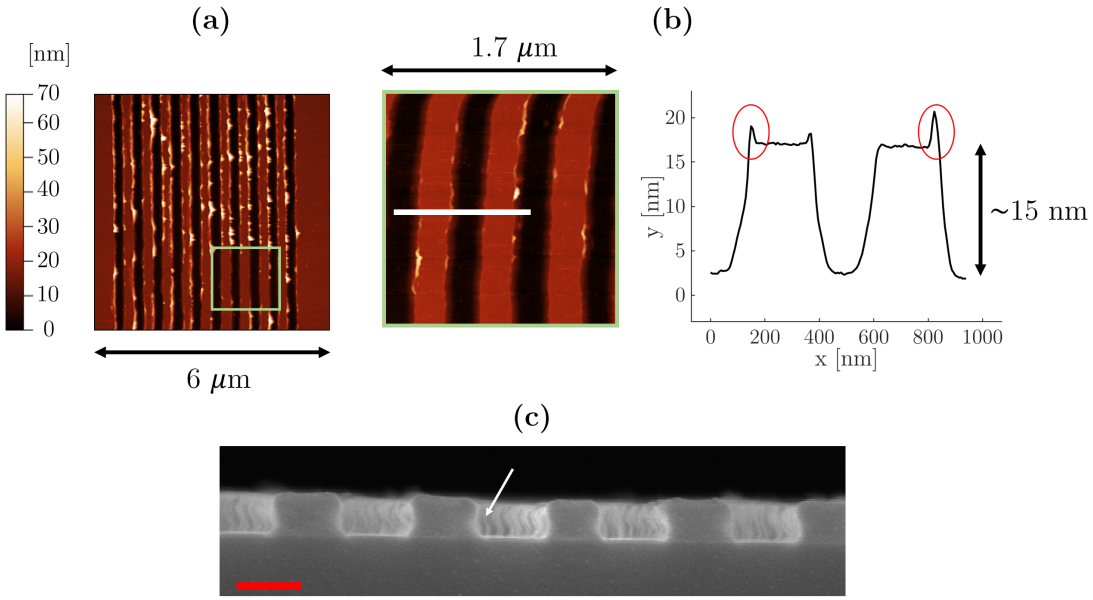


**Figure 5.8:** AFM measures of the etched grooves in a Si–$SiO_2$ substrate after the lift-off procedure **(a)**–**(b)**, and SEM image of the previously exposed mask into the resist **(c)**. The plot in **(b)** shows the surface topography related to the solid white line in the nearby AFM picture. The jutting features at the edge of adjacent grooves (encircled in the curve in **(b)**) may be resulted from a material redeposition during the ion beam milling. Likely, the phenomenon has been facilitated due to the slight undercut profiles in **(c)**, highlighted by the white arrow. The scale bar in **(c)** corresponds to 200 nm.

behind such a sequential process was to figure out the possibly impact of geometrical factors. In this regard, Fig. 5.8 shows the AFM image of a test Si–$SiO_2$ specimen after the resist stripping, which has consisted of repeated ultrasonic baths in NEP at 55 °C.

Since in figure the colour-map traces the surface topography, the black stripes correspond to the etched zones, i.e. to the initial patterned mask, which has been adequately transferred to the substrate. The resulting depth of the trenches was 15 nm, against a target etching of 10 nm. In general, this was not an isolated event, and the etching rates were usually underestimated after the first step of calibration. To fill this gap, the final magnonic crystal has been realized by depositing more Ta and Pt than the 5 nm earlier discussed ($t_{Ta}$ = 8 nm and $t_{Pt}$ = 7 nm), and by keeping fixed the etching time.

Such a change does not invalidate, but it strengthens the reasoning of the previous paragraph instead; as a matter of fact, higher thickness of Ta does not affect the texturation and the magnetic properties of the above layers, and the DMI present a saturation above 4 nm of Pt [108].

A further important remark concerns the 'horns' on the edges (~ 3 nm in height) visible in **(a)**–**(b)**. Albeit jagged borders are quite common after ion beam milling, in principle they could negatively impact on the behaviour of the designed heterostructures. Actually, as stated at the very beginning, here the main interest involves spin waves with wavelengths comparable with the periodicity of the magnetic landscape, which should not be affected by nanometre sized non-idealities in the topography of the magnonic crystal. Indeed, in the present context, what matters is the contrast in the DMI between CoFeB bottom interfaces, which either show such a coupling or not. Nonetheless, a plausible origin for these unwanted traits was ascribed to a redeposition of sputtered material, possibly facilitated by the slight undercut profiles of the resist highlighted by the white arrow in panel **(c)**, which is a SEM image taken on the cross section of the sample. There, during the etching of the substrate, likely the redeposition of sputtered material would have happened. Without modifying the already optimized lithographic process, several attempts have been tried in order to flatten the surface. Especially, since the tilt angle $\theta$ heavily conditions the quality of the etching procedure, we have changed different values for $\theta$ (0°–60°–90°); in addition, other solutions have been tested, such as a prolonged annealing of the samples after the Ta–Pt deposition and the subsequent lift-off, or a soft-etching in the main chamber of the magnetron sputtering, but the situation was worsened at most. Therefore, the issue has remained even in the finished devices, anyway unaffecting the ultimate results.

The reproducibility of the outcomes of Fig. 5.8 has been ascertained by repeating the excavations many times under the same experimental conditions. Then, after the optimization of the etching, the filling of the etched trenches has been optimized too, by carefully controlling the thicknesses of the films ($t_{Ta}$ and $t_{Pt}$) deposited by sputtering. Panel **(a)** of Fig. 5.9 sketches two exemplary combinations for $t_{Ta}$ and $t_{Pt}$. In particular, the AFM profiles

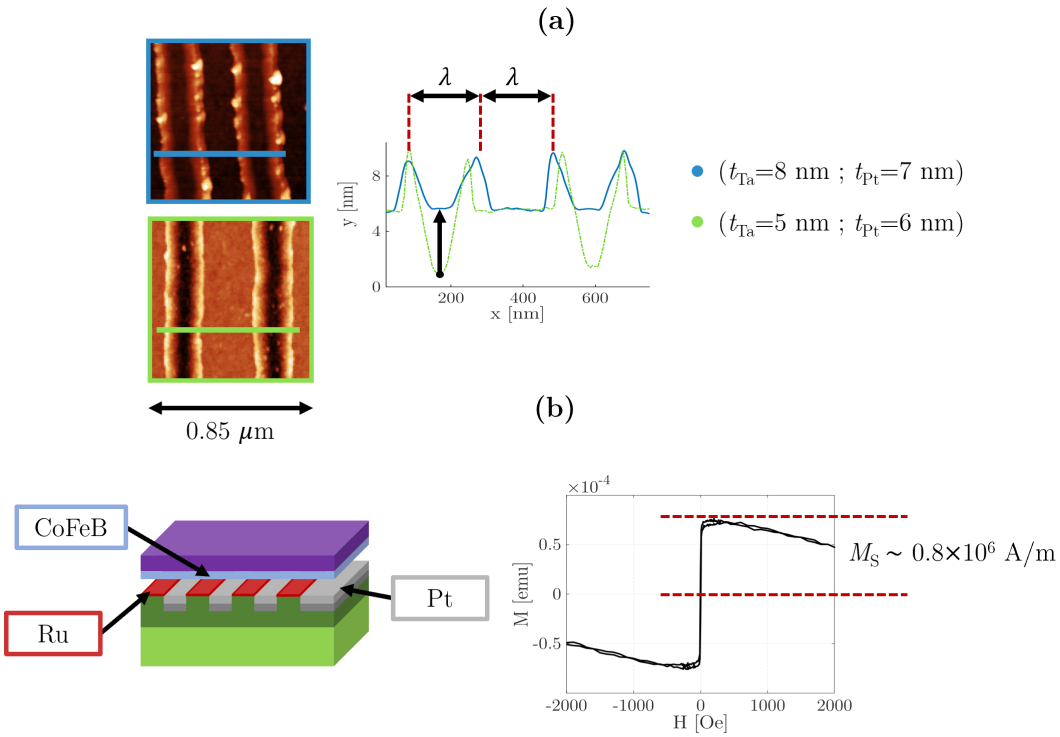


**Figure 5.9:** AFM topography images **(a)** of etched Si–$SiO_2$ substrates, and subsequently filled with $t_{Ta}$ = 8 nm, $t_{Pt}$ = 7 nm (light blue curve) and $t_{Ta}$ = 5 nm, $t_{Pt}$ = 6 nm (green dot-dashed curve). As sketched from the inset on the right, a nearly perfect levelled off surface is attained with the former combination ($\lambda \lesssim 200$ nm). In **(b)**, the schematic for the final magnonic crystals is illustrated, together with the resulting in-plane hysteresis loop. From the last, a saturation magnetization of about $M_S \sim 0.8 \times 10^6$ A/m is extracted, coherently with the presence of either CoFeB/Pt and CoFeB/Ru interfaces.

have been traced after etching, deposition of Ta and Pt, and resist lift-off. As visible from the light blue curve, the height of the substrate ($SiO_2$ in the figure) has been levelled off with nominal $t_{Ta}$ = 8 nm and $t_{Pt}$ = 7 nm (as predictable from Fig. 5.8**(b)**). Noteworthy, now the lateral dimensions of the protruding structures have increased a bit more (~ 4 nm in height, with a (FWHM/2) ~ 50 nm). The trend can be ascribed to the low directionality of the sputtering deposition technique, which provides a conformal coverage of the surfaces of the sample. As a consequence, the grooves have not been filled 'bottom-up', but by accumulating material on their (nearly) ver-

tical walls (i.e. the horns have been 'conformally' coated by the sputtering). However, such an observed behaviour was not supposed to deteriorate the theoretical predictions in [9]. In fact, the filled up zones in between two consecutive protuberances roughly extend as the ones constituted by the $SiO_2$ substrate, giving rise to a nominal spatial periodicity $\lambda \lesssim 200$ nm.

As the final stage, the whole fabrication process has been applied to Si–$SiO_2$/Ru(3) substrates. The only differences with respect to Si–$SiO_2$ samples have resided in the total etching time and lift-off duration. To evaluate the former, the diverse Ru and $SiO_2$ rates (summarized in table 3.1) needed to be taken into account to precisely dig 15 nm deep trenches, as in Fig. 5.7. As for the latter, after etching and sputtering deposition, the substrates were left in NEP at 55 °C for a day, to promote the resist removal from the array of nanometre lines. Lastly, a further inspection of the so attained surfaces was carried out via AFM to verify the procedure accuracy. Then, 1 nm of CoFeB and 5 nm of MgO were grown atop. Subsequently, the samples have been magnetically checked by VSM, as depicted in panel **(b)** of Fig. 5.9, where the in-plane hysteresis loop of an ended system is shown. Especially, as discussed for Fig. 5.2, it has been extracted the saturation magnetization from the raw data, finding an intermediate value of $M_S \sim 0.8 \times 10^6$ A/m, which lies in between the one for the CoFeB/Pt ($M_S = 1.2 \times 10^6$ A/m) and CoFeB/Ru ($M_S = 0.4 \times 10^6$ A/m) boundaries. Note that this non-ideal modulation of $M_S$ due to the presence of Pt and Ru has to be taken into account for quantitatively predict and tune the properties of the magnonic crystals, since the value of $M_S$ greatly influences the spin waves dispersion. However, for the first proof of concept devices, we aim to obtain a qualitative accordance with the predicted results, in view of carrying on further optimizations and simulations. The samples were finally sent to S. Tacchi, of Dipartimento di Fisica e Geologia, Università di Perugia, for the characterization of their magnonic band structure.

## 5.3 Magnonic band structure and future perspectives

The band structure of the magnonic crystals realized so far has been investigated to assess the role of the DMI spatial modulation. To this purpose, to map spin waves wavevectors $k$, BLS spectra, similar to the ones shown in Fig. 5.3, have been acquired by varying the photons incident angle $\phi$. In more detail, for each $\phi$ (i.e. $k$) compatible to the exploited geometry and with the experimental constraints, the corresponding modes have been detected. The right panel of Fig. 5.10 illustrates the outcomes of the measurements, namely the system dispersion curves $f(k)$ related to the lowest frequency branches. Data for positive $k$ refers to Stokes modes, whereas those for negative $k$ to Anti-Stokes ones. To collect the experimental points, a 500 Oe in-plane magnetic field has been imposed in parallel to the Pt stripes to achieve a DE configuration with the wavevector k perpendicular to them. For a comparison, the same figure reports on the left the predicted trends in [9], for a $Ni_{80}Fe_{20}$ film with $D$ = 1.5 mJ/m$^2$ (upper inset), and $D$ = 3 mJ/m$^2$ (bottom inset), and with a periodicity $a$ of $a$ = 100 nm in either the cases (the red lines correspond to the theory and the color code to the MuMax results, where darker (lighter) color represents an intensity maximum (minimum), respectively). As mentioned at the very beginning, three are the main effects theorised in the cited paper: (*i*) low frequency flat bands, (*ii*) indirect gaps, and (*iii*) unconventional time evolution of standing spin waves in the areas of active DMI. Noteworthy, albeit the proof for (*iii*) requires other kinds of measures (like STXM), at least from a qualitative point of view, a quite good agreement in the shape of the theoretical and experimental band structures can be derived from Fig. 5.9. As a matter of fact, the different design of the devices and employed materials (CoFeB instead of NiFe), inevitably makes the graphs not to be numerically compared.

The appearance in **(d)** of a magnonic gap, about 1 GHz wide, testifies that a periodic anisotropy landscape has been efficaciously established inside the CoFeB film. Indeed, within the simplest picture borrowed from the electron behaviour in solids, the periodicity of the internal effective field in

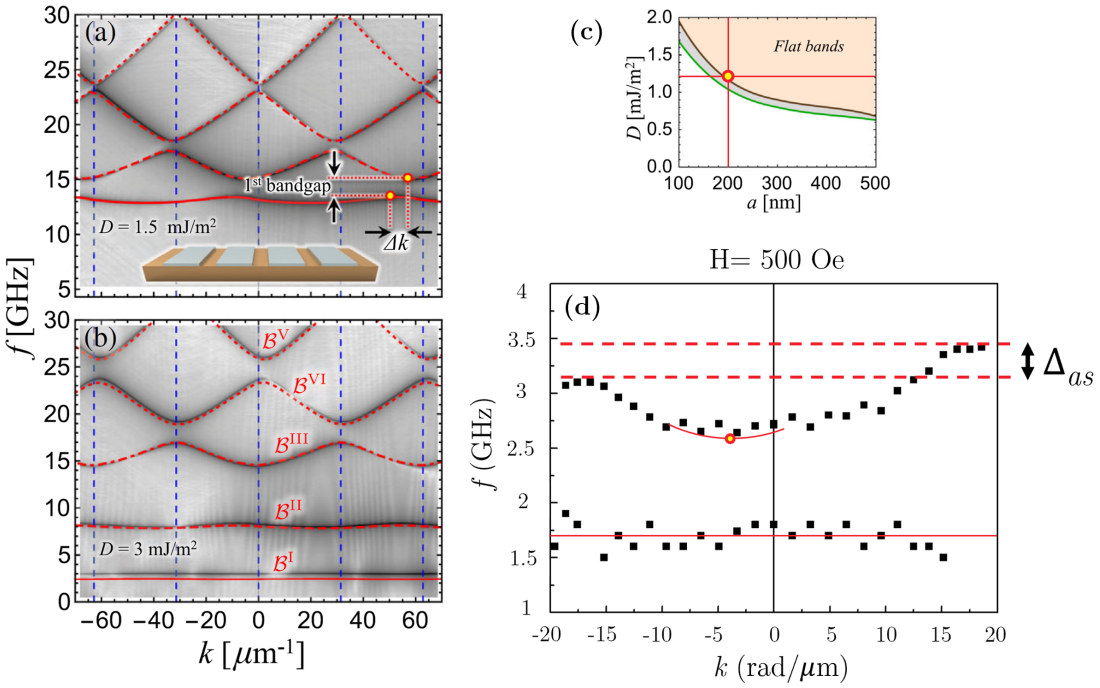


**Figure 5.10:** Panels **(a)** and **(b)** show the magnonic band structure for a $Ni_{80}Fe_{20}$ film covered with an array of HM wires, whose periodicity $a$ equals to $a$ = 100 nm. The effective DMI coupling is $D$ = 1.5 mJ/m$^2$ for **(a)**, and $D$ = 3 mJ/m$^2$ for **(b)**. The smaller inset **(c)** sketches the behaviour for the lowest-lying bands in **(a)** and **(b)** as a function of $a$ and $D$. Especially, the shaded areas correspond to three ranges of $D$ values where different trends are predicted: weak (white region), intermediate (grey region), and strong (flat bands region) coupling, respectively. Our experimental condition is marked with a circled yellow dot. All these panels are taken from [9]. In **(d)** the measure of the magnonic band structure via BLS spectra is reported. The solid red lines are just guides for the eyes.

the magnonic crystal gives rise to counterpropagating 'Bragg-reflected' spin waves, which induce frequency gaps. Besides, from the nearly flat trend, typical near the Brillouin zones edges, of the upper branch around $k \sim 20$ rad/µm, it is possible to guess a later spatial extension for the Pt stripes of ~ 160 nm, not so far from the experimental value $\lambda$ found in the AFM measurements, illustrated in Fig.5.9**(a)**.

With respect to the panels on the left, the upper one draws near the realized structure, being $D$ closer to the nominal one of Fig.5.3 (~ 1.2 mJ/m$^2$). The most impressive result correlated to the work in [9] comes from the

lower measured band, which is almost flat as expected. In fact, **(c)** shows three regions of D values as a function of the periodicity of the array, which correspond to weak (white area), intermediate (grey area), and strong (flat bands area) coupling, respectively. Even considering the differences among the simulated and our system, the experimentally observed flat band condition can be reasonably expected (see the circled yellow dot in panel **(c)**). The corresponding modes have been ascribed to spin waves localized among the Pt stripes, whose temporal evolution is highly non trivial and ultimately promoted by the non-reciprocal nature of the interfacial DMI (for further details, refer to [9]). Moreover, focusing the attention on the upper branch in **(d)**, two other conclusions can be inferred. Firstly, the behaviour of the experimental points may suggest a tiny shift from $k$ = 0 for its minimum (exaggerated with the red curve, which is just a guide to the eyes), though the signal-to-noise ratio does not let to localize it with sufficient accuracy. In turn, this fact could be related to the existence of the speculated indirect band gaps, even if other experiments certainly are required to verify the conjecture. Furthermore, the asymmetry $\Delta_{as}$ highlighted in figure is a side effect not included in the calculation of [9], wherein $D$ is strictly diverse from zero only at the ferromagnet/heavy metal interfaces. In our samples, the origin of $\Delta_{as}$ can be possibly attributed to the small unforeseen DMI revealed at the CoFeB/Ru interfaces (see Fig. 5.5).

Despite the already promising indications coming to light from Fig. 5.9, the research still proceeds to deepen the comprehension of the phenomenon. Especially, three major problems arising from the specimens fabrication need to be faced. On the one hand, to better the contrast between zones with and without DMI, Ru should be replaced with other materials. Beside, the Ru underlayer gives rise to a lower $M_S$ value and a hysteresis loop less squared. Therefore, since both the modulation of $M_S$ and a potential non-uniform PMA throughout the magnonic crystal influence the spin waves dispersion relations, these effects should be either included in the computation or avoided at all. Finally, the fabrication process might be improved to mitigate the presence of the protruding features sketched in Figs. 5.8–5.9. Although, as

expected, their impact seems to be unimportant for the qualitative agreement between the experimental data and the predicted results, they could add some spurious contributions not immediately intelligible from the BLS spectra. Therefore, merging all the pieces together, another draft for the magnonic crystal has been proposed yet, whose structure is depicted in Fig. 5.11. The new concept for the schematic of the device crops up from [108], where a tunable DMI is achieved by varying the Pt thickness $t_{Pt}$ in similar heterostructures. Hence, for the present work, the necessary periodic DMI is ensured by the variation of the Pt height atop the ferromagnet, and can be arbitrarily tailored by accordingly modifying $t_{Pt}$. In particular, the intention is to alternate wires of Pt such that $t_{Pt}$ is large enough to saturate the interfacial DMI with the CoFeB below ($t_{Pt} > 4$ nm), and others with lower thicknesses where the DMI is negligible. Actually, it would be even feasible to invert the sign of the DMI by capping the stripes with low $t_{Pt}$ with a thick Ta film [108]. Moreover, the underlying idea of Fig. 5.11 is to completely avoid the use of Ruthenium, and to get rid of the spikes at the edges of neighbouring trenches. This way, possible issues concerning the continuity of the sandwiched CoFeB layer are totally shunned, resulting in a great step ahead compared to the state-of-the-art magnonic crystals [92, 93, 94]. In fact, the modulation of the magnetic properties in such devices is customarily attained either by placing side by side diverse ferromagnetic compounds or by suitably shaping the geometry of the spin waves waveguides. Anyway, back reflections at the interfaces among different materials, or due to geometrical constraints, are inevitable, thus raising the effective damping for the propagating modes. This is not the case of Fig. 5.11, where the CoFeB interfaces are unaffected by the fabrication process, which is even tremendously simplified, being made up of two stages only: the growing of the entire stack via magnetron sputtering, and one subsequent lithographic step to properly etch the upper Pt level, as in figure.

In this regard, preliminary magnetic characterizations have been carried out to evaluate the magnetic signal in either the 'best' (thicker Pt, which surely prevents the underneath CoFeB from oxidation) and 'worst' (thinner Pt) situations, whose outcomes are illustrated in the bottom panels of Fig.

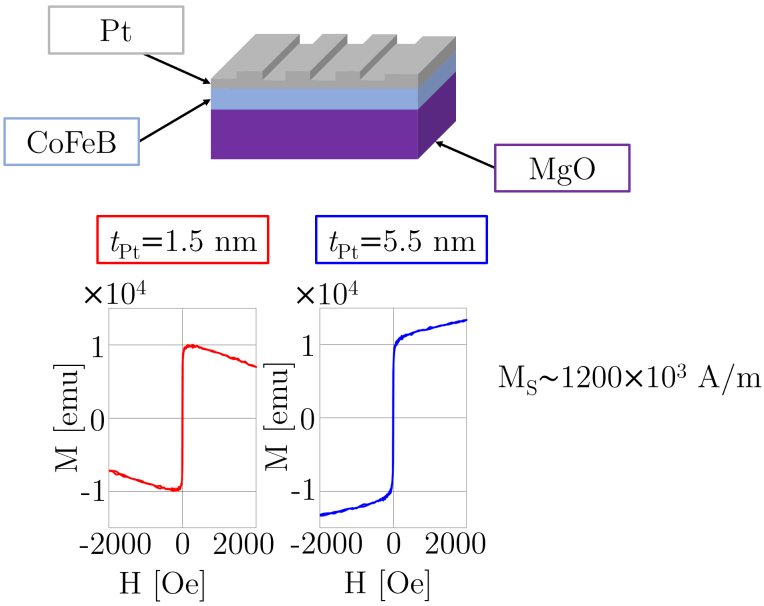


**Figure 5.11:** Novel perspective for the experimental realization of the magnonic crystal in [9]. The new solution envisages an easier fabrication phase, by growing all at once the material stack, and subsequently etching the Pt from above via electron-beam lithography. The insets below trace the in-plane hysteresis loops for the thicker and thinner Pt stripes, respectively. Noteworthy, the absence of magnetic signal loss for $t_{Pt}$ = 1.5 nm is a great advantage compared to the system discussed so far, and it allows a roughly uniform saturation magnetization over all the ferromagnet.

5.11. Remarkably, no significant differences in $M_S$ and in the shape of the hysteresis loops are visible, which in turn means a saturation magnetization and a perpendicular magnetic anisotropy approximately uniform throughout the CoFeB layer (i.e. the idealized condition in [9]). For the sake of completeness, in spite of the various advantages discussed so far, also this solution is not immune from complications. Here, two are the main challenges to face: firstly, several difficulties have been encountered in exploratory BLS measures to align the laser with the 600×600 µm$^2$ patterned array of grooves, due to the poor optical contrast arising from the tiny Pt thickness spatial fluctuations; besides, the etching calibration is much more troublesome respect the one earlier analysed. As a matter of fact, opposite to the case of the previous paragraphs, where the lack of an exact knowledge of the etching

rates could be balanced by subsequently deposing extra material, now the matter is more critical. On the one hand, going too deep possibly means affecting the CoFeB layer, on the other hand, an under-etching would lead to insignificant differences in the interfacial DMI between adjacent regions. Nevertheless, at the moment the work is proceeding towards this direction, and further results are expected in the near future.

# Chapter 6

# Conclusions and perspectives

The present research thesis has been focused on the experimental investigation of spin dynamics in *ad hoc* designed magnonic heterostructures, aiming to implement novel functionalities in view of using spin waves for computing. In other words, it has been practically shown the feasibility of altering spin waves characteristics, namely their wavelengths, their wavefronts and their dispersion relation, by suitably tuning the host materials properties. In this regard, two are the major objectives attained.

Exploiting the blended action of the peculiar magnetic properties of Synthetic Antiferromagnets, resulting in non-reciprocal modes with a nearly isotropic one-way propagation, together with the enormous flexibility allowed by thermally assisted magnetic - Scanning Probe Lithography, magnonic nanoantennas has been used for the first time to realize an optically-inspired system. Especially, arbitrarily shaped wavefronts, featuring nanometre wavelengths, and propagating for distances encompassing several times their periods, have been experimentally observed. Besides, properly tailored emitters have been employed to generate high-quality interference patterns, and to promote other analog operations, such as the focusing of spin waves, thus paving the way towards the concrete realization of nanoscale spin-wave-based computing architectures. Noteworthy, the proposed platform fulfils a complete conventional CMOS technology compatibility, it does not require external magnetic fields, and is fully reconfigurable. Future applications may

involve the developing of non-boolean algorithms and parallel computation, where the power of interference patterns formation may be utilized in digital tasks, such as speech recognition or image processing.

Sharing the same underlying purpose of engineering the spin waves behaviour, the second part of this work has concerned the design, the realization and the preliminary characterization of unconventional one-dimensional magnonic crystals. Particular effort has been devoted to envision a prototype beyond the contemporary limitations of similar metamaterials, namely the presence of discontinuities in the ferromagnetic waveguide, and the extension of the periodicity defining the crystal. To these aims, an original and carefully optimized nanofabrication procedure has been followed. The success of such a customized process has been confirmed by Brillouin Light Scattering measures, which have probed the magnon band structure of the achieved artificial metamaterials. As expected, a gap has been opened in the dispersion relation ruling the system, and the trend of the lowest-lying frequency bands shows a promising agreement with theoretical predictions. At the moment the research is on-going, since a further prospect has been raised which should overcome the encountered experimental obstacles, avoiding the observed spurious contributions. Besides to be a spin waves conduit, more in perspective, the proposed magnonic crystal can be implemented for different purposes. For instance, the capability of filtering spin waves according to their frequency, can be exploited in microwave filters for wireless communications or in signal processing devices performing logic operations. Another example is the realization of magnon transistors, able to modulate the propagation of spin-waves in digital devices. All these possible applications offer novel scenarios for information and communication technologies.

# List of Abbreviations

| | |
|---|---|
| **AFM** | Atomic Force Microscopy |
| **AF** | Antiferromagnet |
| **BLS** | Brillouin Light Spectroscopy |
| **BVMSW** | Backward Volume Magnetostatic Spin Waves |
| **DMI** | Dzyaloshinsky-Moriya Interaction |
| **DW** | Domain Wall |
| **EB** | Exchange Bias |
| **FMR** | Ferromagnetic Resonance |
| **FM** | Ferromagnet |
| **FVMSW** | Forward Volume Magnetostatic Spin Waves |
| **HV** | High Vacuum |
| **IEC** | Interlayer Exchange Couplig |
| **IPA** | IsoPropylic Alcohol |
| **MEMS** | Microelectromechanical Systems |
| **MFM** | Magnetic Force Microscopy |

| | |
|---|---|
| **MSSW** | Magnetostatic Surface Spin Waves |
| **PID** | Proportional-Integral-Derivative |
| **PMA** | Perpendicular Magnetic Anisotropy |
| **PMMA** | Poly(methyl methacrylate) |
| **PVD** | Physical Vapour Deposition |
| **QWS** | Quantum Well State |
| **RF** | Radio Frequency |
| **RKKY** | Ruderman-Kittel-Kasuya-Yosida |
| **SAF** | Synthetic Antiferromagnet |
| **SCCM** | Standard Cubic Centimetres per Minute |
| **SE** | Secondary Electrons |
| **SPM** | Scanning Probe Microscopes |
| **STXM** | Scanning Transmission X-Ray Microscopy |
| **tam-SPL** | thermally assisted magnetic – Scanning Probe Lithography |
| **US** | Ultrasonic |
| **VSM** | Vibrating Sample Magnetometer |
| **XMCD** | X-ray Magnetic Circular Dichroism |

# Bibliography


[1] Bloch, F. Zur Theorie des Ferromagnetismus. *Zeitschrift für Physik* **61**, 206–219 (1930).

[2] Kruglyak, V. V. *et al.* Magnonics. *Journal of Physics D: Applied Physics* **43**, 264001 (2010).

[3] Chumak, A. V. *et al.* Magnonic crystals for data processing. *Journal of Physics D: Applied Physics* **50**, 244001 (2017).

[4] Lenk, B. *et al.* The building blocks of magnonics. *Physics Reports* **507**, 107–136 (2011).

[5] Inoue, M. *et al.* Investigating the use of magnonic crystals as extremely sensitive magnetic field sensors at room temperature. *Applied Physics Letters* **98**, 132511 (2011).

[6] Bankowski, E. *et al.* Magnonic crystal as a delay line for low-noise auto-oscillators. *Applied Physics Letters* **107**, 122409 (2015).

[7] Khitun, A. Multi-frequency magnonic logic circuits for parallel data processing. *Journal of Applied Physics* **111**, 054307 (2012).

[8] Krawczyk, M. & Grundler, D. Review and prospects of magnonic crystals and devices with reprogrammable band structure. *Journal of Physics Condensed Matter* **26**, 123202 (2014).

[9] Gallardo, R. A. *et al.* Flat Bands, Indirect Gaps, and Unconventional Spin-Wave Behavior Induced by a Periodic Dzyaloshinskii-Moriya Interaction. *Physical Review Letters* **122**, 067204 (2019).

[10] Udvardi, L. & Szunyog, L. Chiral Asymmetry of the Spin-Wave Spectra in Ultrathin Magnetic Films. *Physical Review Letters* **102**, 207204 (2009).

[11] Di, K. *et al.* Direct Observation of the Dzyaloshinskii-Moriya Interaction in a Pt/Co/Ni Film. *Physical Review Letters* **114**, 047201 (2015).

[12] Haldar, A. *et al.* A reconfigurable waveguide for energy-efficient transmission and local manipulation of information in a nanomagnetic device. *Nature Nanotechnology* **11**, 437–443 (2016).

[13] Garcia-Sanchez, F. *et al.* Narrow Magnonic Waveguides Based on Domain Walls. *Physical Review Letters* **114**, 247206 (2015).

[14] Albisetti, E. *et al.* Nanoscale spin-wave circuits based on engineered reconfigurable spin-textures. *Communication Physics* **1**, 56 (2018).

[15] Liu, C. *et al.* Long-distance propagation of short-wavelength spin waves. *Nature Communications* **9**, 8274 (2018).

[16] Wintz, S. *et al.* Magnetic vortex cores as tunable spin-wave emitters. *Nature Nanotechnology* **11**, 948–953 (2016).

[17] Demidov, V. E. *et al.* Excitation of microwaveguide modes by a stripe antenna. *Applied Physics Letters* **95**, 112509 (2009).

[18] Coey, J. M. D. *Magnetism and Magnetic Materials*, Cambridge University Press (2010).

[19] Blundell, S. *Magnetism in Condensed Matter*, Oxford University Press (2001).

[20] Aharoni, A. *Introduction to the Theory of Ferromagnetism*, Oxford University Press, 83–84, 173–174 (2002).

[21] Weiss, P. La variation du ferromagnetisme du temperature. *Comptes Rendus*, **146** (1906).

[22] Brown, W. F. Jr. Theory of the Approach to Magnetic Saturation. *Physical Review* **58**, 736–743 (1940).

[23] Landau, L. & Lifshits, E. On the Theory of the Dispersion of Magnetic Permeability in Ferromagnetic Bodies. *Physikalische Zeitschrift der Sowjetunion* **169**, 14–22 (1935).

[24] Gilbert, T. L. A Lagrangian Formulation of the Gyromagnetic Equation of the Magnetization Field. *Physical Review* **100**, 1243 (1955).

[25] Meiklejohn, W. H. & Bean, C. P. New Magnetic Anisotropy. *Physical Review* **105**, 904–913 (1957).

[26] O'Grady, K. *et al.* A new paradigm for exchange bias in polycrystalline thin films. *Journal of Magnetism and Magnetic Materials* **322**, 883–899 (2010).

[27] Kools, J. C. S. Exchange-biased spin-valves for magnetic storage. *IEEE Transactions on Magnetics* **32**, 3165–3184 (1996).

[28] Devasahayam, A. J. & Kryder, M. H. The dependence of the antiferromagnet/ferromagnet blocking temperature on antiferromagnet thickness and deposition conditions. *Journal of Applied Physics* **85**, 5519 (1999).

[29] Radu, F. & Zabel, H. Exchange Bias Effect of Ferro/Antiferromagnetic Heterostructures. *Magnetic Heterostructures* **227**, 97–184 (2007).

[30] Leighton, C. *et al.* Thickness-dependent coercive mechanisms in exchangebiased bilayers. *Physical Review B* **65**, 644031–644037 (2002).

[31] Jungblut, R. *et al.* Orientational dependence of the exchange biasing in molecular-beam-epitaxy-grown $Ni_{80}Fe_{20}/Fe_{50}Mn_{50}$ bilayers. *Journal of Applied Physics* **75**, 6659 (1994).

[32] Nogués, J. & Schuller I. K. Exchange bias. *Journal of Magnetism and Magnetic Materials* **192**, 203–232 (1999).

[33] Grünberg, P. *et al.* Layered Magnetic Structures: Evidence for Antiferromagnetic Coupling of Fe Layers across Cr Interlayers. *Physical Review Letters* **57**, 2442–2445 (1986).

[34] Majkrzak, C. F. *et al.* Observation of a Magnetic Antiphase Domain Structure with Long-Range Order in a Synthetic Gd-Y Superlattice. *Physical Review Letters* **56**, 2700–2703 (1986).

[35] Parkin, S. S. P. *et al.* Oscillations in exchange coupling and magnetoresistance in metallic superlattice structures: Co/Ru, Co/Cr, and Fe/Cr. *Physical Review Letters* **64**, 2304–2307 (1990).

[36] Coehoorn, R. Period of oscillatory exchange interactions in Co/Cu and Fe/Cu multilayer systems. *Physical Review B* **44**, 9331–9337 (1991).

[37] Erickson, R. P. *et al.* Mechanism for non-Heisenberg-exchange coupling between ferromagnetic layers. *Physical Review B* **47**, 2626–2635 (1993).

[38] Wang, Y. *et al.* Interlayer magnetic coupling in Fe/Cr multilayered structures. *Physical Review Letters* **65**, 2732–2735 (1990).

[39] Bruno, P. Interlayer exchange coupling: a unified physical picture. *Journal of Magnetism and Magnetic Materials* **121**, 248–252 (1993).

[40] Stiles, M. D. Interlayer Exchange Coupling, in *Ultrathin Magnetic Structures*, Bland, J. A. C. & Heinrich, B. (Eds.), vol. III, Springer-Verlag, 99–142 (2005).

[41] Bruno, P. Recent progress in the theory of interlayer exchange coupling (invited). *Journal of Applied Physics* **76**, 6972–6976 (1994).

[42] Shull, C. G. et al. Neutron Diffraction by Paramagnetic and Antiferromagnetic Substances. *Physical Review* **83**, 333–345 (1951).

[43] Li, Y. Y. Domain Walls in Antiferromagnets and the Weak Ferromagnetism of $\alpha$-$Fe_2O_3$. *Physical Review* **101**, 1450–1454 (1956).

[44] Dzyaloshinsky, I. A thermodynamic theory of "weak" ferromagnetism of antiferromagnetics. *Journal of Physics and Chemistry of Solids* **4**, 241–255 (1958).

[45] Moriya, T. New Mechanism of Anisotropic Superexchange Interaction. *Physical Review Letters* **4**, 228–230 (1960).

[46] Anderson, P. W. New Approach to the Theory of Superexchange Interactions. *Physical Review* **115**, 2–13 (1959).

[47] Fert, A. *et al.* Skyrmions on the track. *Nature Nanotechnology* **8**, 152–156 (2013).

[48] Bode, M. *et al.* Chiral magnetic order at surfaces driven by inversion asymmetry. *Nature (London)* **447**, 190–193 (2007).

[49] Fert, A. & Levy, P. M. Role of Anisotropic Exchange Interactions in Determining the Properties of Spin-Glasses. *Physical Review Letters* **44**, 1538–1541 (1980).

[50] Tacchi, S. *et al.* Interfacial Dzyaloshinskii-Moriya Interaction in Pt/CoFeB Films: Effect of the Heavy-Metal Thickness. *Physical Review Letters* **118**, 147201 (2017).

[51] Holstein, T. & Primakoff, H. Field dependence of the intrinsic domain magnetization of a ferromagnet. *Physical Review* **58**, 1098–1113 (1940).

[52] Dyson, F. J. Thermodynamic behavior of an ideal ferro-magnet. *Physical Review* **102**, 1230–1244 (1956).

[53] Stancil, D. D. & Prabhakar A. *Spin waves: Theory and Applications*, Springer Science+Business Media (2009).

[54] Damon, R. W. & Eshbach, J. R. Magnetostatic modes of a ferromagnet slab. *Journal of Physics and Chemistry of Solids* **19**, 308–320 (1961).

[55] Eshbach, J. R. Spin-Wave Propagation and the Magnetoelastic Interaction in Yttrium Iron Garnet. *Physical Review Letters* **8**, 357–359 (1962).

[56] Kittel, C. *Introduction to Solid State Physics (eight edition)*, John Wiley & Sons, Inc., 381 (2005).

[57] Kalinikos, B. A. & Slavin, A. N. Theory of dipole-exchange spin wave spectrum for ferromagnetic films with mixed exchange boundary conditions. *Journal of Physics C: Solid State Physics* **19**, 7013–7033 (1986).

[58] Barman, A. & Haldar, A. Time-Domain Study of Magnetization Dynamics in Magnetic Thin Films and Micro- and Nanostructures, in *Solid State Physics*, Camley, R. E. & Stamps, R. L. (Eds), vol. 65, Elsevier Inc., 1–108 (2014).

[59] Camley, R. E. *et al.* Stokes—anti-Stokes asymmetry in Brillouin scattering from magnons in thin ferromagnetic films. *Physical Review B* **26**, 2609–2614 (1982).

[60] Swan, S. Magnetron sputtering. *Physics in Technology* **19**, 67 (1988).

[61] Meggs, Philip B. *A history of graphic design*, John Wiley & Sons, Inc., 146 (1998).

[62] Mack, Chris A. *Fundamental Principles of Optical Lithography: The Science of Microfabrication*, John Wiley & Sons, Inc. (2007).

[63] Levenson, M. D. *et al.* Improving resolution in photolithography with a phase-shifting mask. *IEEE Transactions on Electron Devices* **29**, 1828–1836 (1982).

[64] Vieu, C. *et al.* Electron beam lithography: resolution limits and applications. *Applied Surface Science* **164**, 111–117 (2000).

[65] Chen, W. & Ahmed, H. Fabrication of 5–7 nm wide etched lines in silicon using 100 keV electron beam lithography and polymethylmethacrylate resist. *Applied Physics Letters* **62**, 1499 (1993).

[66] Garcia, R. *et al.* Advanced scanning probe lithography. *Nature Nanotechnology* **9**, 577–587 (2014).

[67] Albisetti, E. *et al.* Nanopatterning reconfigurable magnetic landscapes via thermally assisted scanning probe lithography. *Nature Nanotechnology* **11**, 545–551 (2016).

[68] Albisetti, E. *et al.* Nanopatterning spin-textures: A route to reconfigurable magnonics. *AIP Advances* **7**, 055601 (2017).

[69] Binning, G. *et al.* Atomic Force Microscope. *Physical Review Letters* **56**, 930–933 (1986).

[70] Giessibl, Franz J. Atomic resolution on the silicon (111) – (7×7) surface by atomic force microscopy. *Science* **267**, 68–71 (1995).

[71] Paruch, P. *et al.* Nanoscale control of ferro-electric polarization and domain size in epitaxial $Pb(Zr_{0.2}Ti_{0.8})O_3$ thin films. *Applied Physics Letters* **79**, 530 (2001).

[72] Cappella, B. & Dietler, G. Force-distance curves by atomic force microscopy. *Surface Science Reports* **34**, 1–104 (1999).

[73] Martin, Y. & Wickramasinghe H. K. Magnetic imaging by "force microscopy" with 1000 Å resolution. *Applied Physics Letters* **50**, 1455–1457 (1987).

[74] Rugar, D. *et al.* Magnetic force microscopy: general principles and application to longitudinal recording media. *Journal of Applied Physics* **68**, 1169–1183 (1990).

[75] Raabe, J. *et al.* PolLux: A new facility for soft x-ray spectromicroscopy at the Swiss Light Source. *Review of Scientific Instruments* **79**, 1–10 (2008).

[76] Bauer, H. *et al.* Nonlinear spin-wave excitations at low magnetic bias fields. *Nature Communications* **6**, 8274 (2015).

[77] Vogt, K. *et al.* Spin waves turning a corner. *Applied Physics Letters* **101**, 042410 (2012).

[78] Davies, C. S. *et al.* Towards graded-index magnonics: steering spin waves in magnonic networks. *Physical Review B* **92**, 020408 (2015).

[79] Demidov, V. E. *et al.* Excitation of short-wavelength spin waves in magnonic waveguides. *Applied Physics Letters* **99**, 082507 (2011).

[80] Demokritov, S. O. *et al.* Bose–Einstein condensation of quasi-equilibrium magnons at room temperature under pumping. *Nature* **443**, 430–433 (2006).

[81] Urazhdin, S. *et al.* Nanomagnonic devices based on the spin-transfer torque. *Nature Nanotechnology* **9**, 509–513 (2014).

[82] Wagner, K. *et al.* Magnetic domain walls as reconfigurable spin-wave nanochannels. *Nature Nanotechnology* **11**, 432–436 (2016).

[83] Grünberg, P. Magnetostatic spinwave modes of a heterogeneous ferromagnetic double layer. *Journal of Applied Physics* **52**, 6824–6829 (1981).

[84] Duine, R. A. *et al.* Synthetic antiferromagnetic spintronics. *Nature Physics* **14**, 217–219 (2018).

[85] Wiese, N. *et al.* Antiferromagnetically coupled CoFeB/Ru/CoFeB trilayers. *Applied Physics Letters* **85**, 2020–2022 (2004).

[86] Demidov, V. E. *et al.* Excitation of coherent propagating spin waves by pure spin currents. *Nature Communications* **7**, 10446 (2016).

[87] Vallejo-Fernandez, G. *et al.* Effect of the ferromagnetic layer thickness on the blocking temperature in IrMn/CoFe exchange couples. *IEEE Transactions on Magnetics* **44**, 2835–2838 (2008).

[88] Malinowski, G. *et al.* Correlation between structural quality and magnetic properties of IrMn-based multilayers. *Journal of Applied Physics* **98**, 12–15 (2005).

[89] Albisetti, E. *et al.* Stabilization and control of topological magnetic solitons via magnetic nanopatterning of exchange bias systems. *Applied Physics Letters* **113**, 162401 (2018).

[90] Voto, M. *et al.* Pinned domain wall oscillator as tunable direct current spin wave emitter. *Scientific Reports* **7**, 13559 (2017).

[91] Nikitov, S. A. *et al.* Spin waves in periodic magnetic structures-magnonic crystals. *Journal of Magnetism and Magnetic Materials* **236**, 320–330 (2001).

[92] Chumak, A. V. *et al.* Scattering of backward spin waves in a one-dimensional magnonic crystal. *Applied Physics Letters* **93**, 022508 (2008).

[93] Obry, B. *et al.* A micro-structured ion-implanted magnonic crystal. *Applied Physics Letters* **102**, 202403 (2013).

[94] Chumak, A. V. *et al.* Spin-wave propagation in a microstructured magnonic crystal. *Applied Physics Letters* **95**, 262508 (2009).

[95] Vivas Romero, J. *et al.* Investigation of spin wave damping in three-dimensional magnonic crystals using the plane wave method. *Physical Review* **86**, 144417 (2012).

[96] Chumak, A. V. *et al.* Magnon spintronics. *Nature Physics* **11**, 453–461 (2015).

[97] Ma, F. & Zhou, Y. Interfacial Dzialoshinskii-Moriya interaction induced nonreciprocity of spin waves in magnonic waveguides. *RSC Advances* **4**, 46454 (2014).

[98] Lee, S. *et al.* Spin-wave propagation in the presence of inhomogeneous Dzyaloshinskii-Moriya interactions. *Physical Review Letters* **96**, 184433 (2017).

[99] Torrejon, J. *et al.* Interface control of the magnetic chirality in CoFeB/MgO heterostructures with heavy-metal underlayers. *Nature Communications* **5**, 4655 (2014).

[100] Büttner, F. *et al.* Field-free deterministic ultrafast creation of magnetic skyrmions by spin–orbit torques. *Nature Nanotechnology* **12**, 1040–1044 (2017).

[101] Cho, J. *et al.* Thickness dependence of the interfacial Dzyaloshinskii–Moriya interaction in inversion symmetry broken systems. *Nature Communications* **6**, 7635 (2015).

[102] Brächer, J. *et al.* Detection of Short-Waved Spin Waves in Individual Microscopic Spin-Wave Waveguides Using the Inverse Spin Hall Effect. *Nano Letters* **17**, 7234–7241 (2017).

[103] Cui, B. *et al.* Perpendicular magnetic anisotropy in CoFeB/X (X = MgO, Ta, W, Ti, and Pt) multilayers. *Journal of Alloys and Compounds* **559**, 112–115 (2013).

[104] Di, K. *et al.* Asymmetric spin-wave dispersion due to Dzyaloshinskii-Moriya interaction in an ultrathin Pt/CoFeB film. *Applied Physics Letters* **106**, 052403 (2015).

[105] Oh, Y-W. *et al.* Interfacial perpendicular magnetic anisotropy in CoFeB/MgO structure with various underlayers. *Journal of Applied Physics* **115**, 17C724 (2014).

[106] Jang, S. Y. *et al.* Magnetic dead layer in amorphous CoFeB layers with various top and bottom structures. *Journal of Applied Physics* **107**, 09C707 (2010).

[107] Emori, S. *et al.* Spin Hall torque magnetometry of Dzyaloshinskii domain walls. *Physical Review B* **90**, 184427 (2014).

[108] Chen, Y. *et al.* Tuning Slonczewski-like torque and Dzyaloshinskii–Moriya interaction by inserting a Pt spacer layer in

Ta/CoFeB/MgO structures. *Applied Physics Letters* **112**, 232402 (2018).

[109] Tsai, C. C. *et al.* Superparamagnetic States and Perpendicular Magnetic Anisotropy in Ultrathin MgO/CoFeB/Ta Structures. *IEEE Transactions on Magnetics* **50**, 1–4 (2014).

[110] Oguz, K. *et al.* Magnetic dead layers in sputtered $Co_{40}Fe_{40}B_{20}$ films. *Journal of Applied Physics* **103**, 07B526 (2008).

[111] Olkhovets, A. & Craighead, H. G. Low voltage electron beam lithography in PMMA. *Journal of Vacuum Science & Technology B* **17**, 1366 (1999).

[112] Mohammad, A. M. *et al.* Nanoscale resist morphologies of dense gratings using electron-beam lithography. *Journal of Vacuum Science & Technology B* **25**, 745–753 (2007).

[113] Mohammad, A. M. *et al.* Fundamentals of Electron Beam Exposure and Development, in Nanofabrication: Techniques and Principles, Stepanove, M. & Dew, S. (Eds.), Springer-Verlag, 11–41 (2012).